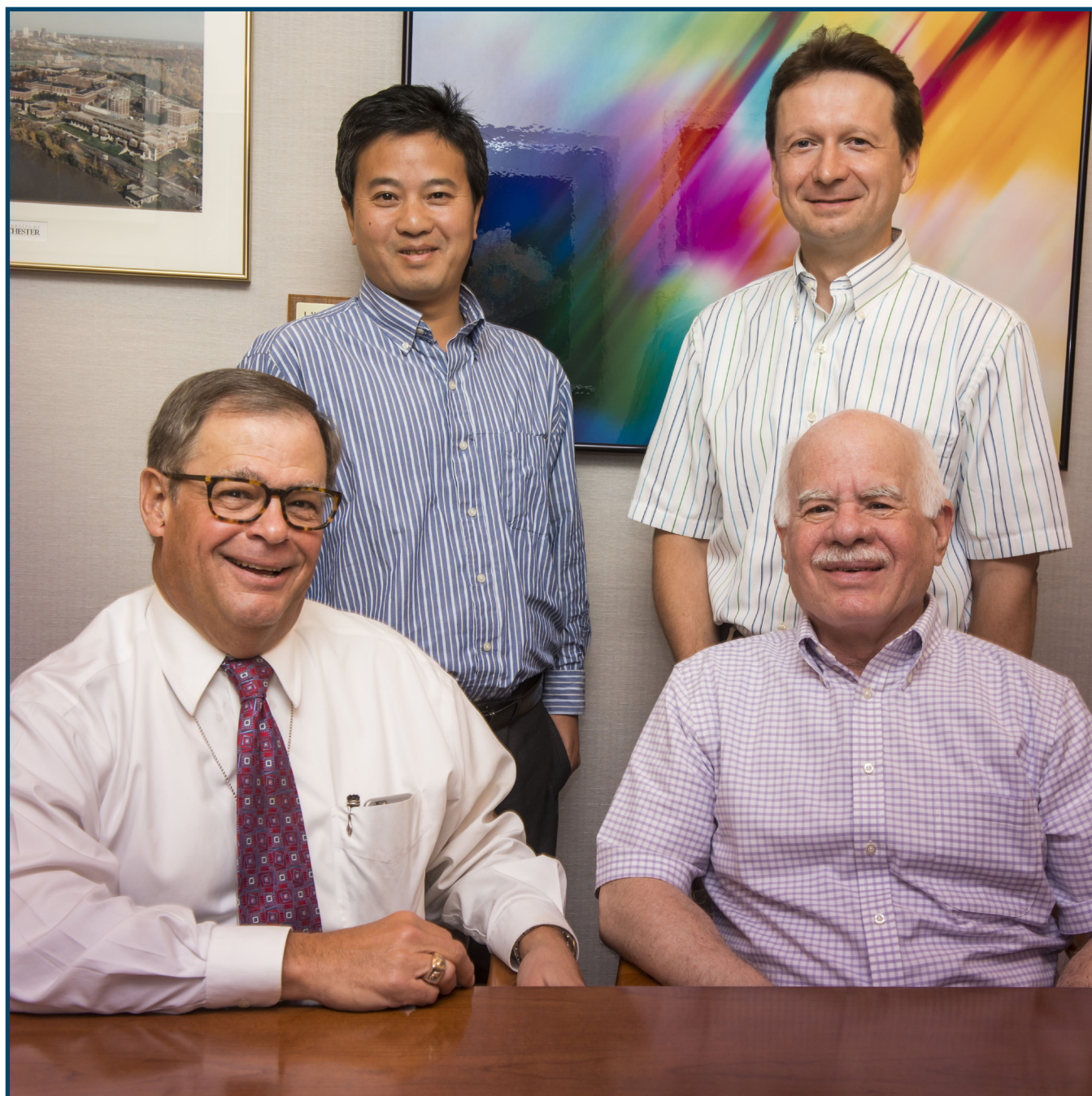


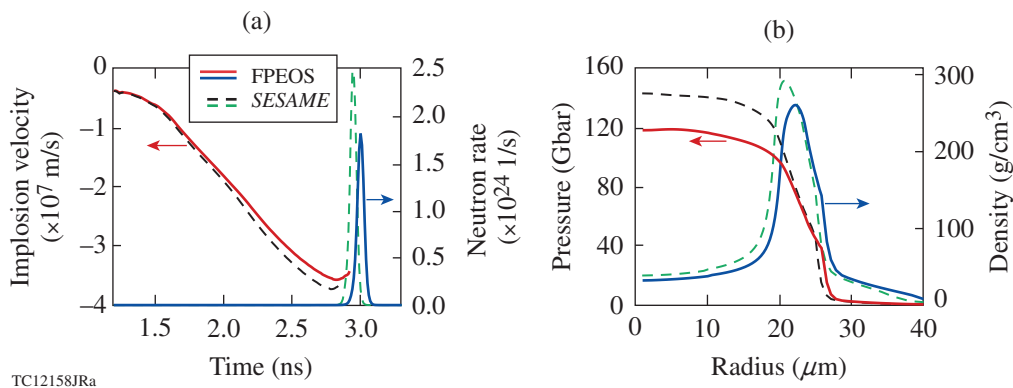
LLE Review

Quarterly Report



About the Cover:

The photograph on the cover features LLE Senior Scientists S. X. Hu, V. N. Goncharov, Laboratory Director and CEO R. L. McCrory, and Theoretical Division Director S. Skupsky. These LLE researchers along with collaborators from Los Alamos National Laboratory, Senior Scientists L. A. Collins (left) and J. D. Kress (right), report on obtaining an accurate first-principles equation of state (FPEOS) of polystyrene (CH). An accurate equation of state (EOS) of CH is essential to obtain accurate hydrodynamic simulations of cryogenic target implosions using CH/CH-based ablaters. Simulations of implosions on OMEGA using the FPEOS of CH have predicted an $\sim 5\%$ reduction in implosion velocity and an $\sim 30\%$ decrease in neutron yield in comparison with the usual *SESAME* simulations.



The figure compares the implosion prediction between *SESAME* EOS (dashed line) and FPEOS (solid line) of CH: (a) the implosion velocity and neutron-production rate as functions of time and (b) the pressure and density as functions of target radius at peak neutron production.

This report was prepared as an account of work conducted by the Laboratory for Laser Energetics and sponsored by the New York State Energy Research and Development Authority, the University of Rochester, the U.S. Department of Energy, and other agencies. Neither the above-named sponsors nor any of their employees makes any warranty, expressed or implied, or assumes any legal liability or responsibility for the accuracy, completeness, or usefulness of any information, apparatus, product, or process disclosed, or represents that its use would not infringe privately owned rights. Reference herein to any specific commercial product, process, or service by trade name, mark, manufacturer, or otherwise, does not necessarily constitute or imply its endorsement, recommendation, or favoring

by the United States Government or any agency thereof or any other sponsor. Results reported in the LLE Review should not be taken as necessarily final results as they represent active research. The views and opinions of authors expressed herein do not necessarily state or reflect those of any of the above sponsoring entities.

The work described in this volume includes current research at the Laboratory for Laser Energetics, which is supported by New York State Energy Research and Development Authority, the University of Rochester, the U.S. Department of Energy Office of Inertial Confinement Fusion under Cooperative Agreement No. DE-NA0001944, and other agencies.

Printed in the United States of America

Available from

National Technical Information Services
U.S. Department of Commerce
5285 Port Royal Road
Springfield, VA 22161
www.ntis.gov

For questions or comments, contact Brian S. Rice, Editor, Laboratory for Laser Energetics, 250 East River Road, Rochester, NY 14623-1299, (585) 275-8001.

Worldwide-Web Home Page: <http://www.lle.rochester.edu/>

LLE Review

Quarterly Report



Contents

In Brief	iii
First-Principles Equation of State of Polystyrene and Its Effect on Inertial Confinement Fusion Implosions	117
Hydrodynamic Scaling of the Deceleration-Phase Rayleigh–Taylor Instability	125
Shock-Wave Equation-of-State Measurements in Fused Silica up to 1600 GPa	139
Temporal-Contrast Measurements of a White-Light–Seeded Noncollinear Optical Parametric Amplifier	145
Computational Chemistry Modeling and Design of Photoswitchable Alignment Materials for Optically Addressable Liquid Crystal Devices	150
The Temporal Analog of Reflection and Refraction of Optical Beams	162
Ultrahigh Responsivity of Optically Active, Semiconducting Asymmetric Nanochannel Diodes	167
Publications and Conference Presentations	

In Brief

This volume of the LLE Review, covering April–June 2015, features “First-Principles Equation of State of Polystyrene and Its Effect on Inertial Confinement Fusion Implosions” by S. X. Hu, V. N. Goncharov, and S. Skupsky (LLE); R. L. McCrory, (LLE, Dept. of Physics and Astronomy, and Dept. of Mechanical Engineering, University of Rochester); and L. A. Collins and J. D. Kress (LANL). This article (p. 117) reports on obtaining an accurate equation of state (EOS) of polystyrene (CH), which is crucial to designing reliable inertial confinement fusion (ICF) capsules using CH/CH-based ablators. With first-principles calculations, they have extended the EOS of CH over a wide range of plasma conditions ($\rho = 0.1$ to 100 g/cm^3 and $T = 1,000$ to $4,000,000 \text{ K}$). When compared with the widely used *SESAME* EOS table, the first-principles equation of state (FPEOS) of CH has significant differences in the low-temperature regime, in which strong coupling and electron degeneracy play an essential role in determining plasma properties. Hydrodynamic simulations of cryogenic target implosions on OMEGA using the FPEOS table of CH have predicted an $\sim 5\%$ reduction in implosion velocity and an $\sim 30\%$ decrease in neutron yield in comparison with the usual *SESAME* simulations. This is attributed to the $\sim 10\%$ lower mass ablation rate of CH predicted by FPEOS. Simulations using the FPEOS of CH show better agreement with measurements of Hugoniot temperature and scattered lights from ICF implosions.

Additional research highlights presented in this issue include the following:

- A. Bose, K. M. Woo, and R. Betti (LLE, Dept. of Physics, and Fusion Science Center), and R. Nora (LLNL) investigate hydrodynamic scaling of the deceleration phase of direct-drive inertial fusion implosions for OMEGA and equivalent National Ignition Facility (NIF)-size targets (p. 125). They show that the deceleration-phase Rayleigh–Taylor instability (RTI) does not scale hydro-equivalently with implosion size. This is because ablative stabilization resulting from thermal conduction and radiation transport in a spherically converging geometry is different on the two scales: NIF-scale implosions show lower hot-spot mass ablation velocity, allowing for higher RTI growth, whereas stabilization resulting from density-gradient enhancement, caused by reabsorption of radiation emitted from the hot spot, is higher on NIF implosions. Since the RTI mitigation related to thermal conduction and radiation transport show opposite trends with the scaling, the effective degradation of implosion performance caused by the deceleration RTI is similar for OMEGA and equivalent NIF targets. It is found that a minimum threshold for the no- α Lawson ignition parameter of $\chi_{\Omega} \approx 0.2$ at the OMEGA scale is required to demonstrate hydro-equivalent ignition at the NIF scale for symmetric direct-drive implosions.
- C. A. McCoy, M. C. Gregor, D. N. Polsin, and T. R. Boehly (LLE); D. D. Meyerhofer (LLE, Dept. Mechanical Engineering, and Dept. of Physics and Astronomy, University of Rochester); and D. E. Fratanduono and P. M. Celliers (LLNL) report on shock-wave equation-of-state measurements in fused silica up to 1600 GPa (p. 139). The properties of silica are important to geophysical and high-pressure equation-of-state research. The most-prevalent crystalline form, α -quartz, has been extensively studied to TPa pressures. Recent experiments with amorphous silica, commonly referred to as fused silica, have provided Hugoniot and reflectivity data up to 630 GPa using magnetically driven aluminum impactors. This article presents measurements of the fused-silica Hugoniot over a range from 200 to 1600 GPa using laser-driven shocks with an α -quartz standard. These data are in very good agreement with those obtained with a different driver and standard material. A new shock velocity/particle relation is derived to fit the experimental data.

- J. Bromage, C. Dorrer, and J. D. Zuegel (LLE) report on temporal-contrast measurements of a white-light–seeded noncollinear optical parametric amplifier. Ultra-intense optical parametric chirped-pulse systems require front ends with broad bandwidth and high temporal contrast (p. 145). Temporal cross-correlation measurements of a white-light–seeded noncollinear optical parametric amplifier (NOPA) show that its prepulse contrast exceeds the 120-dB dynamic range of the broadband NOPA-based cross-correlator.
- K. L. Marshall, E. R. Sekera, and K. Xiao (LLE) investigate computational chemistry modeling and design of photoswitchable alignment materials for optically addressable liquid crystal devices (p. 150). Photoalignment technology based on optically switchable “command surfaces” has been receiving increasing interest for liquid crystal optics and photonics device applications. Azobenzene compounds in the form of low-molar-mass, water-soluble salts deposited either directly onto the substrate surface or after dispersion in a polymer binder have been almost exclusively employed for these applications. Past research in this area followed an inefficient, mostly empirical materials design and development approach. Recent computational chemistry advances now afford unprecedented opportunities to develop efficient predictive capabilities that will lead to new photoswitchable alignment layer materials. In this article, computational methods based on the density functional theory and time-dependent density functional theory were employed to study the impact of molecular structure on optical switching properties in photoswitchable methacrylate and acrylamide polymers functionalized with azobenzene and spiropyran pendants. Using these new computational methods, materials can be efficiently designed with low switching energies, enhanced bistability, write/erase fatigue resistance, and high laser-damage thresholds.
- B. W. Plansinis and G. P. Agrawal (LLE and The Institute of Optics, University of Rochester) and W. R. Donaldson (LLE) study the temporal analog of reflection and refraction of optical beams (p. 162). They show numerically and analytically that when an optical pulse approaches a temporal boundary across which the refractive index changes, it undergoes a temporal equivalent of reflection and refraction of optical beams at a spatial boundary. The main difference is that the role of angles is played by changes in the frequency. The frequency dependence of the dispersion of the material in which the pulse is propagating plays a fundamental role in determining the frequency shifts experienced by the reflected and refracted pulses. Their analytic expressions for these frequency shifts allow them to find the condition under which an analog of total internal reflection may occur at the temporal boundary.
- Y. Akbas, A. Stern, G. W. Wicks, and R. Sobolewski (LLE); L. Q. Zhang, Y. Alimi, and A. M. Song (University of Manchester, Manchester, UK); and I. Iñiguez-de-la-Torre, J. Mateos, and T. González (Universidad de Salamanca, Salamanca, Spain) research ultrahigh responsivity of optically active, semiconducting asymmetric nanochannel diodes (ANCD’s) (p. 167). They study the fabrication and optical characterization of novel semiconducting asymmetric nanochannel diodes. They focus on optical properties of ANCD’s and demonstrate that ANCD’s can be operated as very sensitive, single-photon–level, visible-light photodetectors. Their test devices consisted of 1.5- μm -long, $\sim 300\text{-nm}$ -wide channels that were etched in an InGaAs/InAlAs quantum-well heterostructure with a two-dimensional electron gas layer. The ANCD’s I–V curves were collected by measuring the transport current both in the dark and under 800-nm-wavelength, continuous-wave–light laser illumination. In all of the devices studied, the impact of the light illumination was very clear and there was a substantial photocurrent, even for incident optical power as low as 1 nW. The magnitude of the optical responsivity in ANCD’s with the conducting nanochannel increased linearly with a decrease in optical power over many orders of magnitude, reaching a value of almost 10,000 A/W at 1-nW excitation.

Brian S. Rice
Editor

First-Principles Equation of State of Polystyrene and Its Effect on Inertial Confinement Fusion Implosions

Controlled inertial confinement fusion (ICF)¹ has been pursued in laboratories for decades as a possibly viable route to clean energy. Materials involved in ICF target implosions undergo extreme plasma conditions such as warm dense matter (WDM) of temperatures from a few to several hundreds of electron volts and densities from 10^{21} to 10^{25} ions/cm³. The properties of materials in this critical WDM regime have received much attention because of the wide existence of such extreme conditions in the interiors of giant exoplanets,² the atmospheres of stars,³ and laser-produced plasmas,⁴ in addition to ICF capsules. Precisely determining the properties of WDM has proved challenging since the strong coupling and quantum effects play a critical role in these complex systems. High-energy-density (HED) experiments,^{5–7} equipped with accurate diagnostic tools such as x-ray Thomson scattering^{8–10} and x-ray absorption spectroscopy,^{11,12} have begun to provide detailed tests of various theoretical models of WDM.

For ICF capsules consisting of a cryogenic deuterium–tritium (DT) fuel covered by an ablator layer, accurate knowledge of the ablator and DT material properties would advance the understanding of target performance, leading to improved ICF target designs.¹³ The microphysics responsible for the static, dynamic, and optical properties of DT and ablators determines not only the shock strength and timing^{14,15} but also ionization stages,¹⁶ thermal conduction,¹⁷ and nonuniformity growth¹⁸ in ICF implosions. In particular, the equation of state (EOS) of DT and ablators is essential to closing the hydrodynamic equations for ICF simulations and determining the material compressibility¹⁹ and mass ablation rate,²⁰ which, in turn, control the implosion velocity and the growth of the Rayleigh–Taylor instability.¹⁸ In addition, an accurate EOS of ablators can lead to better predictions of the blowoff plasma conditions, which helps tighten the laser–plasma interaction models used in integrated ICF simulations. Precisely determining the EOS of materials under HED conditions has remained elusive in the past because of the complexity that different interactions need to be fully taken into account. A variety of physics models have been adopted to compute the EOS of materials.

For example, the *SESAME* EOS library²¹ was based on the chemical model of matter, while the quotidian equation of state (QEOS)²² was derived from the improved Thomas–Fermi model. The *SESAME* model used a Helmholtz free energy consisting of a cold curve, an ion thermal contribution, and thermal excitation of electrons calculated by the Thomas–Fermi–Dirac average-atom model. Although such global EOS models have been useful and widely used in the past, their accuracy is worth re-examining in order to make reliable ICF designs and to constrain a laser–plasma interaction model since the margin for ignition is typically small.

Hydrocarbon polymers, such as polystyrene (CH), are often chosen as ablators in both indirect-drive^{23–25} and direct-drive^{26–28} ICF targets because they are inexpensive and easy to make. Upon laser or x-ray irradiation, CH can be shocked to high pressures from Mbar to Gbar. Depending on the driving laser or x-ray pulse shape, the shocked CH may also relax to a temperature well below ~ 5 eV at near-solid densities. Just as important as the properties of the DT fuel^{29–45} are to ICF implosions, accurate knowledge of the CH ablator in the WDM regime is also crucial for reliable ICF designs. Studies of plasma properties under HED conditions have become possible in recent years because of advances in first-principles methods. These first-principles investigations have covered the static EOS of a variety of materials including hydrogen/deuterium,^{29–45} carbon,⁴⁶ polystyrene,^{47–50} and polyethylene,⁵¹ as well as the transport and optical properties of hydrogen/deuterium^{17,52–57} in the WDM regime.

In contrast to previous EOS studies of CH in limited ranges of densities and temperatures, we have combined two first-principles methods—the Kohn–Sham density-functional-theory–based molecular dynamics (KSMD) method^{58,59} and the orbital-free molecular dynamics (OFMD) method⁶⁰—to investigate the global EOS of CH in a wide range of plasma conditions. The KSMD method was implemented in the Vienna *ab initio* simulation package (VASP)^{61–63} using the Perdew–Burke–Ernzerhof (PBE) exchange-correlation func-

tion.⁶⁴ Both KSMD and OFMD methods take the many-body coupling and electron degeneracy effects fully into account. The KSMD calculations cover the low-temperature conditions up to the Fermi temperature (T_F), while the OFMD method is used for higher temperatures. In this article, we report on the first-principles EOS (FPEOS) table of CH and its comparisons with both experiments and the *SESAME* model that is currently used in our hydrocodes.⁶⁵ In particular, we illustrate the importance of an accurate CH ablator EOS to understand the one-dimensional (1-D) physics of ICF implosions through radiation–hydrodynamic simulations.

The FPEOS table of CH has been constructed from the KSMD–OFMD calculations for a wide range of densities $\rho = 0.1$ to 100 g/cm^3 and temperatures $T = 1,000$ to $4,000,000 \text{ K}$. The KSMD calculations cover all densities except $\rho = 0.1 \text{ g/cm}^3$ for plasma temperatures up to T_F , while the OFMD method computes higher-temperature and lower-density conditions. These FPEOS data fully cover the plasma conditions of an ablating CH shell. A supercell containing 250 to 432 atoms (C:H = 1:1) with periodic boundary conditions was used. To make the KSMD–OFMD results into a global EOS table for wide HED applications, we also used OFMD calculations to guide

the linear extrapolation of the FPEOS data to both low-density and high-temperature points outside the direct calculations. The global FPEOS table of CH was implemented into the hydrocode *LILAC*⁶⁵ for ICF implosion simulations.

The FPEOS of CH is first compared with experiments and the *SESAME* EOS model. Figure 143.1 (solid lines) plots the principal Hugoniot predicted by our KSMD–OFMD calculations. The KSMD predictions are made to $\sim 60 \text{ Mbar}$, while the OFMD calculations take over and extend up to the high pressure of $P \simeq 5 \text{ Gbar}$. The Hugoniot matching at around $P \sim 20$ to 30 Mbar from the two first-principles (FP) calculations was performed with the “boot-straping” technique.⁶⁶ This technique uses the Hugoniot matching to infer the internal energy E_0 of initial solid CH at room temperature for the OFMD dataset. As seen in Fig. 143.1(a), the global Hugoniot predicted from the KSMD–OFMD calculations smoothly extends from a low pressure of $\sim 0.2 \text{ Mbar}$ to 5 Gbar . The OFMD matchings at both $T = 120,000 \text{ K}$ and $T = 220,000 \text{ K}$ give almost identical Hugoniot predictions at high pressures. In comparison with the widely used *SESAME* EOS model (Table 7593),²¹ the FP calculations predict CH being slightly stiffer in the pressure range of 5 to 80 Mbar

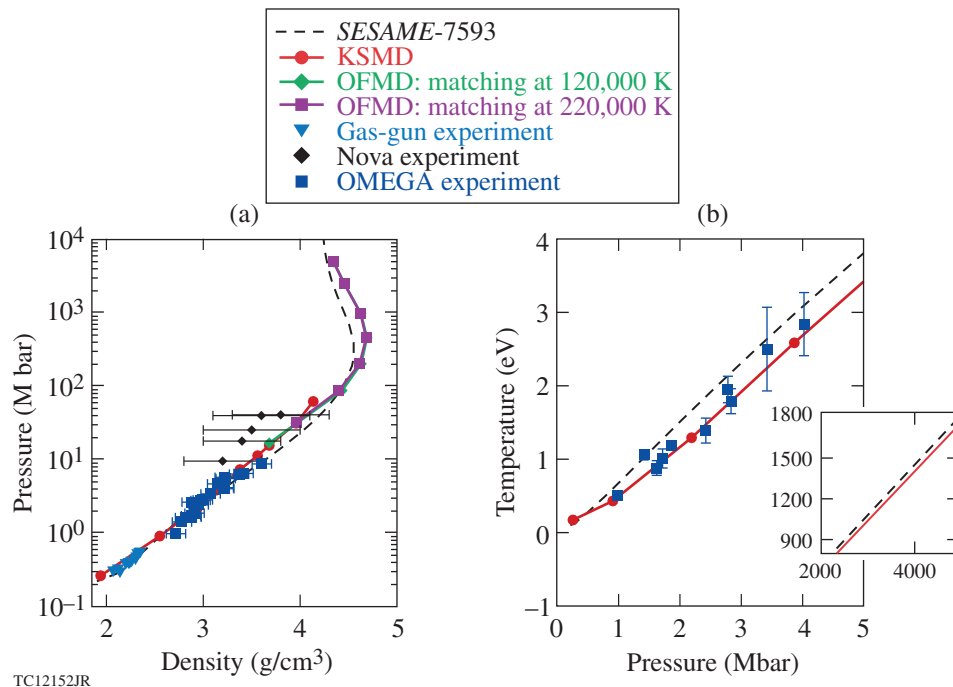


Figure 143.1

(a) The principal Hugoniot pressure as a function of shock density; (b) the temperature of Hugoniot versus pressure. The Kohn–Sham density-functional-theory–based KSMD results (red circles) and the orbital-free molecular-dynamics (OFMD) predictions (purple squares and green diamonds) are compared with the gas-gun experiment,⁶⁷ the Nova experiment,⁶⁸ and the recent impedance-matching experiment⁶⁹ on OMEGA. The prediction of *SESAME*-7593 is plotted with the dashed line.

but softer in higher pressures up to ~ 5 Gbar. The maximum compression has been shifted from the *SESAME*-predicted $\rho_m = 4.55 \text{ g/cm}^3$ at $P = 220 \text{ Mbar}$ to $\rho_m = 4.68 \text{ g/cm}^3$ at $P = 440 \text{ Mbar}$ in the FPEOS because of the lower temperature inferred from FPEOS [see the inset of Fig. 143.1(b)]. In experiments, the EOS of CH has been extensively studied using gas-gun and laser-driven shock waves. The gas-gun experiment⁶⁷ was typically in the low-pressure regime ($P < 1 \text{ Mbar}$), while the laser experiments at the Nova⁶⁸ and Omega Laser Facilities⁶⁹ have recorded shock strengths up to $\sim 40 \text{ Mbar}$. Other shock experiments^{49,70,71} of the CH Hugoniot have explored the pressure range of $P < 5 \text{ Mbar}$. The available experimental data have been compared with the FPEOS and *SESAME* predictions in Fig. 143.1(a). In the pressure range $P < 10 \text{ Mbar}$, both predictions are in good agreement with experiments (within the experimental error). The Hugoniot temperature measured in the recent OMEGA experiment,⁶⁹ however, is in much better agreement with the FPEOS prediction [see Fig. 143.1(b)]. The *SESAME* model predicts a maximum of $\sim 30\%$ -higher Hugoniot temperature because it underestimates the internal energy in this pressure range (discussed in detail below). The stiffer behavior of CH, seen in the Nova experiment [e.g., Fig. 143.1(a)] at high pressures of $P = 10$ to 40 Mbar , seems to qualitatively point toward the FPEOS, even though the experimental error bars were large.

Next, we examine the off-Hugoniot comparison between the FPEOS table and the *SESAME* model in Figs. 143.2 and 143.3, in which the total pressure (P), internal energy (E), and their variations are plotted as functions of CH density for different plasma temperatures. Figures 143.2(a) and 143.2(c) display the direct comparisons of pressure and internal energy between FPEOS (solid lines) and *SESAME* (dashed lines) at $T = 15,625 \text{ K}$ ($\approx 1.35 \text{ eV}$). At this low temperature, large differences in both P and E appear in the low-density regime of $\rho < 3 \text{ g/cm}^3$. To clearly show the variations, the percentage changes of P and E between FPEOS and *SESAME* are plotted in Figs. 143.2(b) and 143.2(d). Figures 143.2(b) and 143.2(d) show that the pressure variations can be as large as approximately -100% in the low-density regime ($\rho < 1.0 \text{ g/cm}^3$) and the energy can vary from $+40\%$ at $\rho = 0.5 \text{ g/cm}^3$ to -20% at high densities. At such a low temperature and not too high densities, it is difficult for models to properly account for all of the important microscopic interactions among the variety of species (atoms, molecules, ions, and electrons) in warm dense plasmas. The first-principles methods take these interactions into account as completely as possible, which can lead to a more-accurate determination of material properties in the WDM regime. When the CH plasma temperature increases to $T = 31,250 \text{ K}$ ($\approx 2.7 \text{ eV}$) and $T = 125,000 \text{ K}$ ($\approx 10.8 \text{ eV}$), the

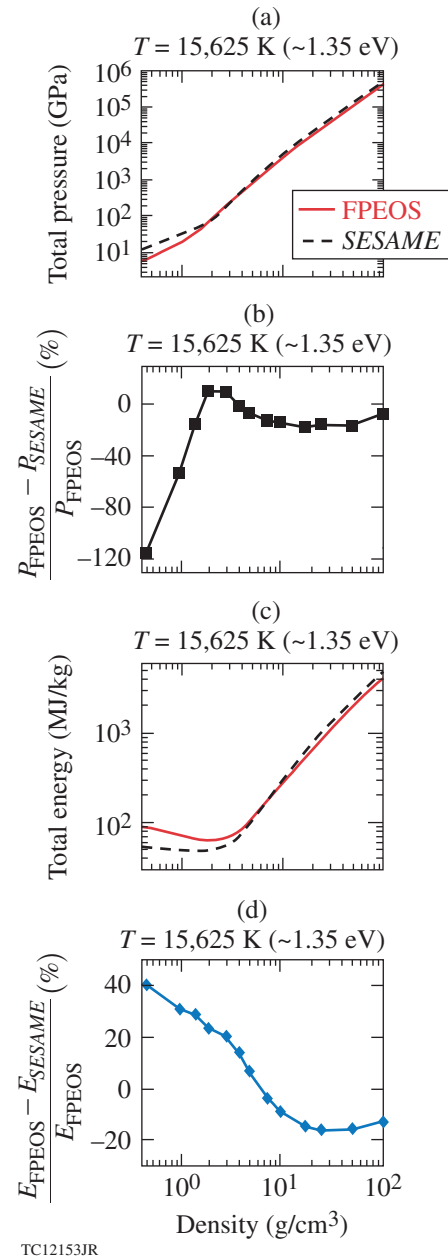
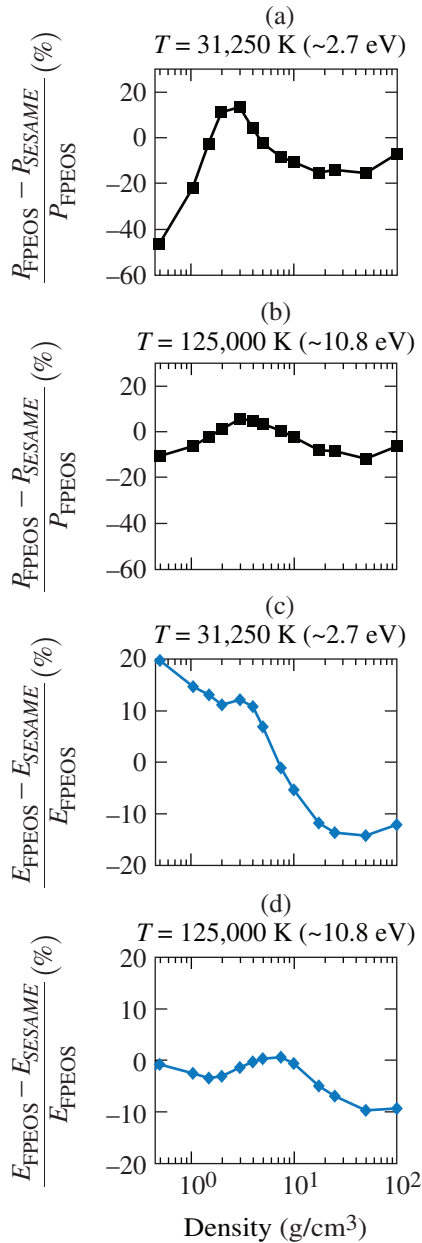


Figure 143.2 The equation-of-state (EOS) comparisons of [(a) and (b)] pressure and [(c) and (d)] internal energy between FPEOS and *SESAME*-7593 as a function of CH density for a plasma temperature of $T \approx 1.35 \text{ eV}$. The actual values of pressure and energy are plotted in (a) and (c), while the percentage variations between FPEOS and *SESAME*-7593 are plotted in (b) and (d).

many-body and quantum effects become less dominant than in the low- T case. Therefore, the percentage variations between FPEOS and *SESAME*, shown in Fig. 143.3, are reduced as the plasma temperature increases. They change from $\pm 20\%$ at $T = 2.7 \text{ eV}$ to within $\sim \pm 10\%$ for the higher temperature of $T = 10.8 \text{ eV}$ [see Figs. 143.3(b) and 143.3(d)].



TC12154JR

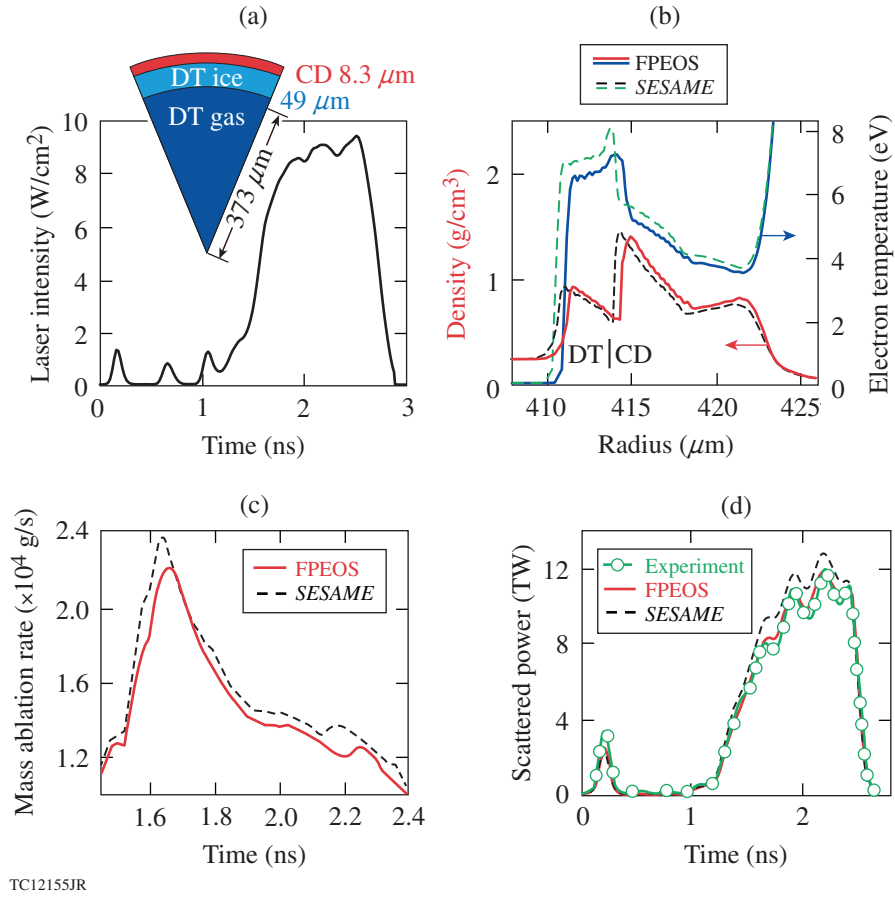
Figure 143.3

Similar to Figs. 143.2(b) and 143.2(d) but for higher plasma temperatures of $T \simeq 2.7$ eV and $T \simeq 10.8$ eV. The variations between FPEOS and *SESAME*-7593 become smaller (toward the $\pm 10\%$ range) as the plasma temperature increases.

With the FPEOS table of CH incorporated into *LILAC*,⁶⁵ we can now simulate ICF implosions. By comparing experiments with the hydrodynamic simulations using both FPEOS and *SESAME* models of CH, we can examine how the more-accurate FPEOS of CH affects the 1-D predictions of target performance. As an example, Figs. 143.4 and 143.5 show the two

hydro-simulation results for a cryogenic DT target implosion on OMEGA. Figure 143.4(a) plots the triple-picket pulse shape^{72–74} with an inset of target dimensions. The cryo-DT target consists of a $49\text{-}\mu\text{m}$ DT layer with an $8.3\text{-}\mu\text{m}$ deuterated plastic (CD) ablator, which is imploded by the low-adiabat laser pulse. The EOS of CD is obtained by mass scaling the FPEOS of CH. The 1-D hydro simulations for both cases have used the same nonlocal thermal-transport model⁷⁵ and cross-beam energy transfer model^{76,77} in the laser-absorption package. During irradiation of the first laser picket, the plastic is ablated and a shock is launched into the shell. Figure 143.4(b) shows the density and temperature profiles as functions of target radius at $t = 0.5$ ns, in which the FPEOS results (solid lines) are compared to the *SESAME* simulation (dashed lines). At this time, the shock has propagated into the DT layer and the plasma temperature in the CD shell is less than ~ 5 eV. The relaxation after the shock brings the CD density below the solid level ($\rho_0 = 1.05$ g/cm³). This is the regime in which large differences ($\sim \pm 20\%$ or more) were found between FPEOS and *SESAME*. As a result, the hydro simulation with FPEOS predicts a lower temperature in the shell (consistent with the lower temperature seen in the shock Hugoniot). This leads to a smaller mass ablation rate of plastic in FPEOS versus *SESAME*, which is shown in Fig. 143.4(c). As the “rocket” effect indicates, less mass ablation rate in FPEOS can lead to a smaller ablation pressure and a slower implosion velocity. We found that at the end of the pulse ($t = 2.5$ ns), the FPEOS-predicted shell travels ~ 20 μm behind the *SESAME* simulation and the ablation pressure is reduced by $\sim 10\%$, from 92 Mbar (*SESAME*) to 83 Mbar with FPEOS. Furthermore, the slower ablation can affect the laser light scattering in the coronal plasma. Figure 143.4(d) compares the two predictions with the scattered-light measurement. It shows that the FPEOS simulation gives better agreement with experiment.

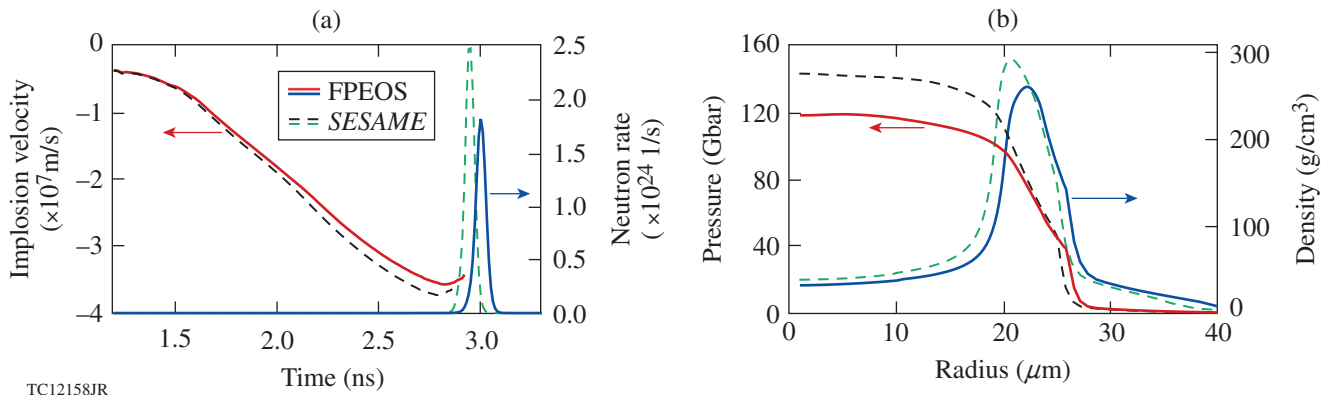
Finally, we discuss the overall target performance between the FPEOS and *SESAME* simulations. Figure 143.5(a) plots the implosion velocities and neutron production rates as functions of time. Because of the smaller mass ablation rate of CH predicted by FPEOS [e.g., Fig. 143.4(c)], the implosion velocity is reduced by $\sim 5\%$, varying from $V_{\text{imp}} \simeq 3.7 \times 10^7$ m/s (*SESAME*) to $V_{\text{imp}} \simeq 3.5 \times 10^7$ m/s (FPEOS). This causes a delay of ~ 50 ps in the neutron bang time (the time at which the neutron rate reaches peak) for the FPEOS simulation. From the scaling law of $Y \propto V_{\text{imp}}^6$ for the neutron yield,^{78–80} the $\sim 5\%$ reduction in V_{imp} can have a significant consequence in neutron production. Figure 143.5(a) shows a lower peak neutron rate in the FPEOS case (blue solid line), which gives a total neutron yield of $Y = 1.1 \times 10^{14}$, dropping from the *SESAME*-predicted value of $Y = 1.5 \times 10^{14}$. At their peak neutron production, Fig. 143.5(b)



TC12155JR

Figure 143.4

The effect of CH-FPEOS on the cryogenic DT target implosion on OMEGA: (a) the triple-picket pulse shape and target dimensions; (b) the density and temperature profiles at $t = 0.5$ ns that are predicted by radiation–hydrodynamic simulations using either FPEOS (solid lines) or *SESAME* (dashed lines) for the plastic ablator; (c) the predicted mass ablation rates as a function of time; and (d) the comparison of scattered-light predictions with experimental measurement.



TC12158JR

Figure 143.5

Comparisons of the implosion prediction between *SESAME* EOS (dashed lines) and FPEOS (solid lines) of CH: (a) the implosion velocity and neutron-production rate as functions of time and (b) the pressure and density as functions of target radius at peak neutron production.

shows the hot-spot pressure and shell-density degradation in the FPEOS simulation. The hot-spot peak pressure is reduced from $P = 142$ Gbar (*SESAME*) to $P = 118$ Gbar (FPEOS), and the DT shell is stagnated at a slightly larger radius and lower peak density for the FPEOS simulation. Also, the neutron-averaged hot-spot temperature decreases from $T_i = 3.6$ keV (*SESAME*) to $T_i = 3.4$ keV (FPEOS), although the change in neutron-averaged $\langle \rho R \rangle$ is only moderate (<5%), $\langle \rho R \rangle = 262$ mg/cm² (*SESAME*) versus $\langle \rho R \rangle = 250$ mg/cm² (FPEOS).

In summary, we combined the two *ab initio* methods of KSMD and OFMD to calculate the equation of state for the ICF ablator material of CH, in a wide range of plasma conditions. The Hugoniot's pressure and temperature, predicted from the FPEOS table, are both in better agreement with experiments. Large differences in both pressure and energy have been observed in the low-temperature WDM regime when the FPEOS is compared with the widely used *SESAME* model. Hydro simulations of an ICF target implosion using the FPEOS of CH predict ~5%-lower implosion velocity, ~10% decrease in ablation pressure, and ~30% neutron yield reduction relative to the usual *SESAME* simulation. These are caused by the smaller mass ablation rate predicted by the CH FPEOS. The reduction of ablation velocity may have implications in nonuniformity growth at the ablation front, which will be examined in future multidimensional hydro simulations. Overall, the predicted scattered light with the FPEOS simulation is in better agreement with experimental measurements. Using our more-accurate FPEOS of ablators in hydrodynamic simulations will lead to improved ICF target design and better predictions of HED physics experiments.

ACKNOWLEDGMENT

This material is based upon work supported by the Department of Energy National Nuclear Security Administration under Award Number DE-NA0001944, the University of Rochester, and the New York State Energy Research and Development Authority. The support of DOE does not constitute an endorsement by DOE of the views expressed in this article. This work was also supported by Scientific Campaign 10 at the Los Alamos National Laboratory, operated by Los Alamos National Security, LLC for the National Nuclear Security Administration of the U.S. Department of Energy under Contract No. DE-AC52-06NA25396.

REFERENCES

1. J. Nuckolls *et al.*, *Nature* **239**, 139 (1972).
2. N. C. Santos, W. Benz, and M. Mayor, *Science* **310**, 251 (2005).
3. G. Fontaine, P. Brassard, and P. Bergeron, *Publ. Astron. Soc. Pac.* **113**, 409 (2001).
4. B. A. Hammel *et al.*, *High Energy Density Phys.* **6**, 171 (2010); D. H. Froula, D. T. Michel, I. V. Igumenshchev, S. X. Hu, B. Yaakobi, J. F. Myatt, D. H. Edgell, R. Follett, V. Yu. Glebov, V. N. Goncharov, T. J. Kessler, A. V. Maximov, P. B. Radha, T. C. Sangster, W. Seka, R. W. Short, A. A. Solodov, C. Sorce, and C. Stoeckl, *Plasma Phys. Control. Fusion* **54**, 124016 (2012).
5. S. H. Glenzer and R. Redmer, *Rev. Mod. Phys.* **81**, 1625 (2009).
6. S. H. Glenzer *et al.*, *Science* **327**, 1228 (2010).
7. A. L. Kritcher *et al.*, *Phys. Rev. Lett.* **107**, 015002 (2011).
8. S. H. Glenzer *et al.*, *Phys. Rev. Lett.* **90**, 175002 (2003).
9. B. Barbrel *et al.*, *Phys. Rev. Lett.* **102**, 165004 (2009).
10. S. P. Regan, K. Falk, G. Gregori, P. B. Radha, S. X. Hu, T. R. Boehly, B. J. B. Crowley, S. H. Glenzer, O. L. Landen, D. O. Gericke, T. Döppner, D. D. Meyerhofer, C. D. Murphy, T. C. Sangster, and J. Vorberger, *Phys. Rev. Lett.* **109**, 265003 (2012).
11. S. M. Vinko *et al.*, *Nature* **482**, 59 (2012).
12. O. Ciricosta *et al.*, *Phys. Rev. Lett.* **109**, 065002 (2012).
13. S. X. Hu, V. N. Goncharov, T. R. Boehly, R. L. McCrory, S. Skupsky, L. A. Collins, J. D. Kress, and B. Militzer, *Phys. Plasmas* **22**, 056304 (2015).
14. T. R. Boehly, V. N. Goncharov, W. Seka, M. A. Barrios, P. M. Celliers, D. G. Hicks, G. W. Collins, S. X. Hu, J. A. Marozas, and D. D. Meyerhofer, *Phys. Rev. Lett.* **106**, 195005 (2011).
15. H. F. Robey *et al.*, *Phys. Rev. Lett.* **111**, 065003 (2013).
16. L. B. Fletcher *et al.*, *Phys. Rev. Lett.* **112**, 145004 (2014).
17. V. Recoules *et al.*, *Phys. Rev. Lett.* **102**, 075002 (2009).
18. V. A. Smalyuk *et al.*, *Phys. Rev. Lett.* **112**, 185003 (2014); V. A. Smalyuk, S. X. Hu, J. D. Hager, J. A. Delettrez, D. D. Meyerhofer, T. C. Sangster, and D. Shvarts, *Phys. Rev. Lett.* **103**, 105001 (2009).
19. S. X. Hu, V. A. Smalyuk, V. N. Goncharov, J. P. Knauer, P. B. Radha, I. V. Igumenshchev, J. A. Marozas, C. Stoeckl, B. Yaakobi, D. Shvarts, T. C. Sangster, P. W. McKenty, D. D. Meyerhofer, S. Skupsky, and R. L. McCrory, *Phys. Rev. Lett.* **100**, 185003 (2008).
20. D. T. Michel, A. K. Davis, V. N. Goncharov, T. C. Sangster, S. X. Hu, I. V. Igumenshchev, D. D. Meyerhofer, W. Seka, and D. H. Froula, *Phys. Rev. Lett.* **114**, 155002 (2015).
21. B. I. Bennett *et al.*, Los Alamos National Laboratory, Los Alamos, NM, Report LA-7130 (1978).
22. R. M. More *et al.*, *Phys. Fluids* **31**, 3059 (1988).
23. S. W. Haan, J. D. Lindl, D. A. Callahan, D. S. Clark, J. D. Salmonson, B. A. Hammel, L. J. Atherton, R. C. Cook, M. J. Edwards, S. Glenzer, A. V. Hamza, S. P. Hatchett, M. C. Herrmann, D. E. Hinkel, D. D. Ho, H. Huang, O. S. Jones, J. Kline, G. Kyrala, O. L. Landen, B. J.

- MacGowan, M. M. Marinak, D. D. Meyerhofer, J. L. Milovich, K. A. Moreno, E. I. Moses, D. H. Munro, A. Nikroo, R. E. Olson, K. Peterson, S. M. Pollaine, J. E. Ralph, H. F. Robey, B. K. Spears, P. T. Springer, L. J. Suter, C. A. Thomas, R. P. Town, R. Vesey, S. V. Weber, H. L. Wilkens, and D. C. Wilson, *Phys. Plasmas* **18**, 051001 (2011).
24. M. J. Edwards, J. D. Lindl, B. K. Spears, S. V. Weber, L. J. Atherton, D. L. Bleuel, D. K. Bradley, D. A. Callahan, C. J. Cerjan, D. Clark, G. W. Collins, J. E. Fair, R. J. Fortner, S. H. Glenzer, S. W. Haan, B. A. Hammel, A. V. Hamza, S. P. Hatchett, N. Izumi, B. Jacoby, O. S. Jones, J. A. Koch, B. J. Koziowski, O. L. Landen, R. Lerche, B. J. MacGowan, A. J. MacKinnon, E. R. Mapoles, M. M. Marinak, M. Moran, E. I. Moses, D. H. Munro, D. H. Schneider, S. M. Sepke, D. A. Shaughnessy, P. T. Springer, R. Tommasini, L. Bernstein, W. Stoeffl, R. Betti, T. R. Boehly, T. C. Sangster, V. Yu. Glebov, P. W. McKenty, S. P. Regan, D. H. Edgell, J. P. Knauer, C. Stoeckl, D. R. Harding, S. Batha, G. Grim, H. W. Herrmann, G. Kyrala, M. Wilke, D. C. Wilson, J. Frenje, R. Petrasso, K. Moreno, H. Huang, K. C. Chen, E. Giraldez, J. D. Kilkenny, M. Mauldin, N. Hein, M. Hoppe, A. Nikroo, and R. J. Leeper, *Phys. Plasmas* **18**, 051003 (2011).
 25. C. Cherfils-Cl  rouin *et al.*, *J. Phys.: Conf. Ser.* **244**, 022009 (2010).
 26. D. D. Meyerhofer, R. L. McCrory, R. Betti, T. R. Boehly, D. T. Casey, T. J. B. Collins, R. S. Craxton, J. A. Delettrez, D. H. Edgell, R. Epstein, K. A. Fletcher, J. A. Frenje, V. Yu. Glebov, V. N. Goncharov, D. R. Harding, S. X. Hu, I. V. Igumenshchev, J. P. Knauer, C. K. Li, J. A. Marozas, F. J. Marshall, P. W. McKenty, P. M. Nilson, S. P. Padalino, R. D. Petrasso, P. B. Radha, S. P. Regan, T. C. Sangster, F. H. S  guin, W. Seka, R. W. Short, D. Shvarts, S. Skupsky, J. M. Soares, C. Stoeckl, W. Theobald, and B. Yaakobi, *Nucl. Fusion* **51**, 053010 (2011).
 27. R. L. McCrory, R. Betti, T. R. Boehly, D. T. Casey, T. J. B. Collins, R. S. Craxton, J. A. Delettrez, D. H. Edgell, R. Epstein, J. A. Frenje, D. H. Froula, M. Gatu-Johnson, V. Yu. Glebov, V. N. Goncharov, D. R. Harding, M. Hohenberger, S. X. Hu, I. V. Igumenshchev, T. J. Kessler, J. P. Knauer, C. K. Li, J. A. Marozas, F. J. Marshall, P. W. McKenty, D. D. Meyerhofer, D. T. Michel, J. F. Myatt, P. M. Nilson, S. J. Padalino, R. D. Petrasso, P. B. Radha, S. P. Regan, T. C. Sangster, F. H. S  guin, W. Seka, R. W. Short, A. Shvydky, S. Skupsky, J. M. Soares, C. Stoeckl, W. Theobald, B. Yaakobi, and J. D. Zuegel, *Nucl. Fusion* **53**, 113021 (2013).
 28. R. S. Craxton, K. S. Anderson, T. R. Boehly, V. N. Goncharov, D. R. Harding, J. P. Knauer, R. L. McCrory, P. W. McKenty, D. D. Meyerhofer, J. F. Myatt, A. J. Schmitt, J. D. Sethian, R. W. Short, S. Skupsky, W. Theobald, W. L. Kruer, K. Tanaka, R. Betti, T. J. B. Collins, J. A. Delettrez, S. X. Hu, J. A. Marozas, A. V. Maximov, D. T. Michel, P. B. Radha, S. P. Regan, T. C. Sangster, W. Seka, A. A. Solodov, J. M. Soares, C. Stoeckl, and J. D. Zuegel, "Direct-Drive Inertial Confinement Fusion: A Review," to be published in *Physics of Plasmas*.
 29. L. Caillabet, S. Mazevet, and P. Loubeyre, *Phys. Rev. B* **83**, 094101 (2011).
 30. L. Caillabet *et al.*, *Phys. Rev. Lett.* **107**, 115004 (2011).
 31. P. Loubeyre, S. Brygoo, J. Eggert, P. M. Celliers, D. K. Spaulding, J. R. Rygg, T. R. Boehly, G. W. Collins, and R. Jeanloz, *Phys. Rev. B* **86**, 144115 (2012).
 32. S. X. Hu, B. Militzer, V. N. Goncharov, and S. Skupsky, *Phys. Rev. Lett.* **104**, 235003 (2010).
 33. S. X. Hu, B. Militzer, V. N. Goncharov, and S. Skupsky, *Phys. Rev. B* **84**, 224109 (2011).
 34. M. A. Morales *et al.*, *High Energy Density Phys.* **8**, 5 (2012).
 35. J. Vorberger, D. O. Gericke, and W. D. Kraeft, *High Energy Density Phys.* **9**, 448 (2013).
 36. V. V. Karasiev *et al.*, *Phys. Rev. B* **88**, 161108(R) (2013).
 37. C. Pierleoni *et al.*, *Phys. Rev. Lett.* **73**, 2145 (1994).
 38. B. Militzer and D. M. Ceperley, *Phys. Rev. Lett.* **85**, 1890 (2000).
 39. J. Cl  rouin and J.-F. Dufr  che, *Phys. Rev. E* **64**, 066406 (2001).
 40. L. A. Collins *et al.*, *Phys. Rev. B* **63**, 184110 (2001).
 41. M. P. Desjarlais, *Phys. Rev. B* **68**, 064204 (2003).
 42. B. Holst, R. Redmer, and M. P. Desjarlais, *Phys. Rev. B* **77**, 184201 (2008).
 43. C. Wang and P. Zhang, *Phys. Plasmas* **20**, 092703 (2013).
 44. A. Becker *et al.*, *Astrophys. J. Suppl. Ser.* **215**, 21 (2014).
 45. L. X. Benedict, "A Review of Equation of State Models for Hydrogen," to be published in *World Scientific Review*.
 46. R. F. Smith *et al.*, *Nature* **511**, 330 (2014).
 47. C. Wang, X.-T. He, and P. Zhang, *Phys. Plasmas* **18**, 082707 (2011).
 48. F. Lambert and V. Recoules, *Phys. Rev. E* **86**, 026405 (2012).
 49. S. Hamel, L. X. Benedict, P. M. Celliers, M. A. Barrios, T. R. Boehly, G. W. Collins, T. D  ppner, J. H. Eggert, D. R. Farley, D. G. Hicks, J. L. Kline, A. Lazicki, S. LePape, A. J. Mackinnon, J. D. Moody, H. F. Robey, E. Schwegler, and P. A. Sterne, *Phys. Rev. B* **86**, 094113 (2012).
 50. S. X. Hu, T. R. Boehly, and L. A. Collins, *Phys. Rev. E* **89**, 063104 (2014).
 51. T. R. Mattsson *et al.*, *Phys. Rev. B* **81**, 054103 (2010).
 52. B. Holst, M. French, and R. Redmer, *Phys. Rev. B* **83**, 235120 (2011).
 53. F. Lambert *et al.*, *Phys. Plasmas* **18**, 056306 (2011).
 54. C. E. Starrett *et al.*, *Phys. Plasmas* **19**, 102709 (2012).
 55. S. X. Hu, L. A. Collins, T. R. Boehly, J. D. Kress, V. N. Goncharov, and S. Skupsky, *Phys. Rev. E* **89**, 043105 (2014).
 56. S. X. Hu, L. A. Collins, V. N. Goncharov, T. R. Boehly, R. Epstein, R. L. McCrory, and S. Skupsky, *Phys. Rev. E* **90**, 033111 (2014).
 57. G. Faussurier and C. Blancard, *Phys. Plasmas* **22**, 042701 (2015).

58. L. Collins *et al.*, Phys. Rev. E **52**, 6202 (1995).
59. J. G. Clérouin and S. Bernard, Phys. Rev. E **56**, 3534 (1997).
60. F. Lambert, J. Clérouin, and G. Zérah, Phys. Rev. E **73**, 016403 (2006).
61. G. Kresse and J. Hafner, Phys. Rev. B **47**, 558 (1993).
62. G. Kresse and J. Hafner, Phys. Rev. B **49**, 14,251 (1994).
63. G. Kresse and J. Furthmüller, Phys. Rev. B **54**, 11169 (1996).
64. J. P. Perdew, K. Burke, and M. Ernzerhof, Phys. Rev. Lett. **77**, 3865 (1996); *ibid.* **78**, 1396(E) (1997).
65. J. Delettrez, R. Epstein, M. C. Richardson, P. A. Jaanimagi, and B. L. Henke, Phys. Rev. A **36**, 3926 (1987).
66. D. Sheppard *et al.*, Phys. Rev. E **90**, 063314 (2014).
67. S. P. Marsh, ed. *LASL Shock Hugoniot Data*, Los Alamos Series on Dynamic Material Properties (University of California Press, Berkeley, CA, 1980).
68. R. Cauble *et al.*, Phys. Plasmas **4**, 1857 (1997).
69. M. A. Barrios, D. G. Hicks, T. R. Boehly, D. E. Fratanduono, J. H. Eggert, P. M. Celliers, G. W. Collins, and D. D. Meyerhofer, Phys. Plasmas **17**, 056307 (2010).
70. M. Koenig *et al.*, Phys. Plasmas **10**, 3026 (2003).
71. N. Ozaki *et al.*, Phys. Plasmas **16**, 062702 (2009).
72. V. N. Goncharov, T. C. Sangster, T. R. Boehly, S. X. Hu, I. V. Igumenshchev, F. J. Marshall, R. L. McCrory, D. D. Meyerhofer, P. B. Radha, W. Seka, S. Skupsky, C. Stoeckl, D. T. Casey, J. A. Frenje, and R. D. Petrasso, Phys. Rev. Lett. **104**, 165001 (2010).
73. T. C. Sangster, V. N. Goncharov, R. Betti, P. B. Radha, T. R. Boehly, D. T. Casey, T. J. B. Collins, R. S. Craxton, J. A. Delettrez, D. H. Edgell, R. Epstein, C. J. Forrest, J. A. Frenje, D. H. Froula, M. Gatu-Johnson, V. Yu. Glebov, D. R. Harding, M. Hohenberger, S. X. Hu, I. V. Igumenshchev, R. Janezic, J. H. Kelly, T. J. Kessler, C. Kingsley, T. Z. Kosc, J. P. Knauer, S. J. Loucks, J. A. Marozas, F. J. Marshall, A. V. Maximov, R. L. McCrory, P. W. McKenty, D. D. Meyerhofer, D. T. Michel, J. F. Myatt, R. D. Petrasso, S. P. Regan, W. Seka, W. T. Shmayda, R. W. Short, A. Shvydky, S. Skupsky, J. M. Soures, C. Stoeckl, W. Theobald, V. Versteeg, B. Yaakobi, and J. D. Zuegel, Phys. Plasmas **20**, 056317 (2013).
74. S. X. Hu, V. N. Goncharov, P. B. Radha, J. A. Marozas, S. Skupsky, T. R. Boehly, T. C. Sangster, D. D. Meyerhofer, and R. L. McCrory, Phys. Plasmas **17**, 102706 (2010).
75. V. N. Goncharov, T. C. Sangster, P. B. Radha, R. Betti, T. R. Boehly, T. J. B. Collins, R. S. Craxton, J. A. Delettrez, R. Epstein, V. Yu. Glebov, S. X. Hu, I. V. Igumenshchev, J. P. Knauer, S. J. Loucks, J. A. Marozas, F. J. Marshall, R. L. McCrory, P. W. McKenty, D. D. Meyerhofer, S. P. Regan, W. Seka, S. Skupsky, V. A. Smalyuk, J. M. Soures, C. Stoeckl, D. Shvarts, J. A. Frenje, R. D. Petrasso, C. K. Li, F. Séguin, W. Manheimer, and D. G. Colombant, Phys. Plasmas **15**, 056310 (2008).
76. I. V. Igumenshchev, W. Seka, D. H. Edgell, D. T. Michel, D. H. Froula, V. N. Goncharov, R. S. Craxton, L. Divol, R. Epstein, R. Follett, J. H. Kelly, T. Z. Kosc, A. V. Maximov, R. L. McCrory, D. D. Meyerhofer, P. Michel, J. F. Myatt, T. C. Sangster, A. Shvydky, S. Skupsky, and C. Stoeckl, Phys. Plasmas **19**, 056314 (2012); D. H. Froula, T. J. Kessler, I. V. Igumenshchev, R. Betti, V. N. Goncharov, H. Huang, S. X. Hu, E. Hill, J. H. Kelly, D. D. Meyerhofer, A. Shvydky, and J. D. Zuegel, Phys. Plasmas **20**, 082704 (2013).
77. V. N. Goncharov, T. C. Sangster, R. Betti, T. R. Boehly, M. J. Bonino, T. J. B. Collins, R. S. Craxton, J. A. Delettrez, D. H. Edgell, R. Epstein, R. K. Follet, C. J. Forrest, D. H. Froula, V. Yu. Glebov, D. R. Harding, R. J. Henchen, S. X. Hu, I. V. Igumenshchev, R. Janezic, J. H. Kelly, T. J. Kessler, T. Z. Kosc, S. J. Loucks, J. A. Marozas, F. J. Marshall, A. V. Maximov, R. L. McCrory, P. W. McKenty, D. D. Meyerhofer, D. T. Michel, J. F. Myatt, R. Nora, P. B. Radha, S. P. Regan, W. Seka, W. T. Shmayda, R. W. Short, A. Shvydky, S. Skupsky, C. Stoeckl, B. Yaakobi, J. A. Frenje, M. Gatu-Johnson, R. D. Petrasso, and D. T. Casey, Phys. Plasmas **21**, 056315 (2014).
78. M. C. Herrmann, M. Tabak, and J. D. Lindl, Nucl. Fusion **41**, 99 (2001).
79. C. D. Zhou and R. Betti, Phys. Plasmas **15**, 102707 (2008).
80. R. Nora, R. Betti, K. S. Anderson, A. Shvydky, A. Bose, K. M. Woo, A. R. Christopherson, J. A. Marozas, T. J. B. Collins, P. B. Radha, S. X. Hu, R. Epstein, F. J. Marshall, R. L. McCrory, T. C. Sangster, and D. D. Meyerhofer, Phys. Plasmas **21**, 056316 (2014).

Hydrodynamic Scaling of the Deceleration-Phase Rayleigh–Taylor Instability

Introduction

In inertial confinement fusion (ICF),¹ a shell of cryogenic deuterium (D) and tritium (T) filled with DT gas is imploded with direct laser illumination (direct drive)² or through an x-ray bath produced inside a laser-irradiated hohlraum (indirect drive).³ Energy from the laser or x ray is absorbed in the plasma near the outer surface of the target, causing mass ablation. The ablation pressure pushes the shell inward by the “rocket effect.” In addition to the Rayleigh–Taylor (RT) unstable outer surface during the acceleration phase, the inner surface of the shell is also unstable to the Rayleigh–Taylor instability (RTI) during the deceleration phase. The RT spikes stream into the hot spot, decreasing the burn volume and increasing the surface-to-volume ratio of the hot spot. This, in turn, increases the conduction losses,⁴ resulting in a reduction in hot-spot temperature. The perturbations rapidly become nonlinear, and a significant fraction of the shell’s kinetic energy is used to feed lateral motion, instead of contributing to the hot-spot pressure through radial compression.^{5,6} The effective areal density ρR of the shell is expected to decrease and degrade the confinement time, burn volume, hot-spot pressure and temperature, and, therefore, the neutron yield. The yield-over-clean (YOC) is used as a measure of the effect of hydrodynamic instabilities on the implosion performance:⁷

$$\text{YOC} = \left[\frac{\text{yield from exp or 3-D/2-D sim}}{\text{yield from 1-D sim}} \right]. \quad (1)$$

In an ICF implosion the initial nonuniformities arise because of ice roughness on the inner surface of the shell (which is usually greater than on the outer surface) and laser imprinting on the outer surface of the target.

The National Ignition Facility (NIF)⁸ was built to perform 1.8-MJ (i.e., ignition-scale) indirect-drive implosions with 192 beams in a polar configuration. X-ray illumination was chosen because it was expected to improve target stability, but at the cost of a lower drive (i.e., reduced energy coupling

to the target). Consequently, the stagnation pressure required for indirect-drive ignition is more than double that for direct drive with the same laser energy. Currently, the NIF is not configured to perform symmetric direct-drive illumination; therefore, it is being used in polar-direct-drive⁹ mode to test direct drive. Polar direct drive is expected to achieve lower performance levels than symmetric drive. OMEGA¹⁰ experiments, on the other hand, routinely use symmetric illumination, so extrapolating OMEGA to the NIF should be viewed as an upper bound of current NIF polar-direct-drive capabilities. Nevertheless, given the low NIF shot rate and high cost, extrapolating OMEGA experimental results to the NIF provides a very valuable tool for guiding future direct-drive experiments on the NIF.

The theory of hydrodynamic equivalence provides a way to extrapolate implosion performance on the OMEGA Laser System to ignition scales. Since scaling of the nuclear yield from an implosion ($Y \sim P_s^2 T_s \tau_b V_b$, where τ_b is the burnwidth and V_b is the neutron-averaged volume or *burn volume*) is dominated by the hot-spot pressure at stagnation P_s , the theory of hydro-equivalent scaling is developed keeping identical P_s for implosions with different driver energies. Unlike the pressure, the temperature at stagnation T_s is not scale invariant and is determined by considering the scaling of the hot-spot thermal conduction (see **Hydro-Equivalent Scaling of the Deceleration Phase**, p. 129). As described in Ref. 11, hydro-equivalent implosions designed to achieve the same stagnation pressure require equal values of the implosion velocity V_{imp} , shell adiabat α_0 , and laser intensity I_L . A consequence of this choice of scaling is that the acceleration-phase RTI also scales hydro-equivalently if the initial seeds of the instability scale proportionally to the target radius R . A complete table of the one-dimensional (1-D) hydrodynamic scaling relations for ICF is listed in Ref. 11. The target dimensions (i.e., radius R and shell thickness Δ) and time t scale with laser energy E_L as

$$R \sim \Delta \sim E_L^{1/3}, \quad t \sim E_L^{1/3}, \quad (2)$$

where $E_{L\text{NIF}}/E_{L\Omega} \approx 4^3$. Therefore, target sizes and laser pulse shapes for extrapolated direct-drive (NIF) ignition-scale implosions are $4\times$ larger and longer than on OMEGA. The goal of this article is to examine the effect of the above hydrodynamic scaling on the deceleration-phase RTI and the hot-spot ignition condition.

Hot-Spot Dynamics and Hydrodynamic Equivalence

This section presents a model that describes the deceleration phase, starting from the hot-spot formation to the onset of ignition. The analysis is similar to that in Ref. 12. We also consider the effect of both losses and reabsorption of bremsstrahlung radiation. A fraction of the radiation energy emitted from the hot spot is reabsorbed at the hot-spot/shell interface; the remaining energy is treated as a loss. In the following subsections an analytic formulation of the hot-spot energy balance and mass ablation from the inner surface of the shell is developed; the effect of the radiation losses on the ignition condition is shown; the scaling of the deceleration-phase RTI is discussed; and the scaling of the YOC and the ignition condition is derived.

1. Hot-Spot Energy Balance

The hot-spot plasma is treated as an ideal gas with highly subsonic flows, and the hot-spot energy equation can be written as follows:

$$\begin{aligned} & \frac{\partial}{\partial t} \left(\frac{p}{\Gamma-1} \right) + \nabla \cdot \left[\tilde{u} \left(\frac{\Gamma p}{\Gamma-1} \right) \right] \\ & = \nabla \cdot \kappa(T) \nabla T - \nabla \cdot \vec{F} + \frac{\theta \rho^2}{4m_1^2} \langle \sigma v \rangle \varepsilon_\alpha, \end{aligned} \quad (3)$$

where $p(r,t)$, $\tilde{u}(r,t)$, and $\rho(r,t)$ are the pressure, velocity, and density of the hot spot, respectively. Since the hot spot is subsonic ($\rho u^2 \ll p$), the kinetic energy is small compared to the internal energy and has been omitted from the terms on the left-hand side. The ideal-gas adiabatic index Γ is $5/3$ for DT gas. The first term on the right-hand side represents Spitzer thermal conduction $\kappa(T) = \kappa_0 T^v$, where $v = 5/2$ and $\kappa_0 = 3.7 \times 10^{69} \text{ m}^{-1} \text{ s}^{-1} \text{ J}^{-5/2}$ for $\ln \Lambda \approx 5$. Energy gained from fusion reaction is given by the third term, where θ is the fraction of total α -particle energy deposited in the hot spot, m_1 is the average mass of DT ions, and ε_α (3.5 MeV) is the energy per α particle. The fusion reactivity follows $\langle \sigma v \rangle \approx C_\sigma T^3$ in the temperature range 3 to 8 keV with $C_\sigma \approx 2.6 \times 10^{-26} \text{ m}^3 \text{ keV}^{-3} \text{ s}^{-1}$. The second term on the right-hand side of Eq. (3) represents the radiation losses, with \vec{F} as the first moment of the radiation field over angle.¹³ The bremsstrahlung emission from the hot spot integrated over all frequencies is given by

$$j = C_b p^2 T^{-3/2}, \quad (4)$$

where $C_b \approx 3.88 \times 10^{-29} Z^3 / (1+Z)^2$ in $\text{J}^{5/2} \text{N}^{-2} \text{m s}^{-1}$, the pressure p is in N/m^2 , temperature T is in joules, and j is in W/m^3 . The ionization fraction Z is 1 for DT gas, with the assumption that there is no high- Z material mixed into the hot spot, which would considerably increase the bremsstrahlung losses. The subsonic hot-spot approximation applied to the momentum equation results in $p \approx p(t)$ (i.e., the hot spot is isobaric). The temperature of the low-density hot spot is much higher than the high-density shell, resulting in a self-similar solution for the hot-spot temperature given by¹⁴

$$T \approx T_c(t) f(\hat{r}) \quad \text{with} \quad f(\hat{r}) = \frac{(1 - \hat{r}^2)^{2/5}}{(1 - 0.15\hat{r}^2)}, \quad (5)$$

where $T_c(t)$ is the temperature of the hot spot's center and $\hat{r} = r/R_{\text{hs}}$ is the radial distance normalized to hot-spot radius R_{hs} . Bremsstrahlung radiation flux leaving a sphere of radius \hat{r} calculated using Eq. (4) is given by

$$F(\hat{r}) = \frac{C_b p^2 T_c^{-3/2} R_{\text{hs}}}{\hat{r}^2} \int_0^{\hat{r}} f^{-3/2} \hat{r}^2 d\hat{r}, \quad \text{for } r < R_{\text{hs}}, \quad (6)$$

$$F(\hat{r}) = \mathcal{L} \frac{C_b p^2 T_c^{-3/2} R_{\text{hs}}}{\hat{r}^2} \frac{\mu_0}{3}, \quad \text{for } r > R_{\text{hs}},$$

assuming that the low-temperature shell does not produce emission. Here,

$$\mu_0 = 3 \times \int_0^1 f^{-3/2} \hat{r}^2 d\hat{r} \approx 2.54$$

and $\mathcal{L}(t)$ is the fraction of emitted energy leaving the hot spot and shell.

The hot-spot energy equation was derived by integrating Eq. (3) from 0 to the hot-spot radius $R_{\text{hs}}(t)$. Since the shell velocity ($\dot{R}_{\text{hs}} \sim 350 \text{ km/s}$) is much greater than the ablation velocity ($V_{\text{abl}} \sim 10 \text{ km/s}$), it was neglected; i.e., $u(R_{\text{hs}}, t) = \dot{R}_{\text{hs}} - V_{\text{abl}} \approx \dot{R}_{\text{hs}}$. The hot-spot energy equation can be written in a dimensionless form as

$$\frac{d}{d\tau} (\hat{p} \hat{R}^5) = \gamma \hat{p}^2 \hat{R}^5 \hat{T}^\sigma - \beta_1 \hat{p}^2 \hat{R}^5 \hat{T}^{-3/2} \hat{\mathcal{L}}(\tau), \quad (7a)$$

$$\gamma = \frac{\varepsilon_\alpha C_\sigma \mu_2}{24 c_k^{2+\sigma}} \left(\frac{p_s R_s}{V_{\text{imp}}} \right) T_*^\sigma, \quad (7b)$$

$$\beta_1 = \mathcal{L}_s \frac{2}{3} \mu_0 C_b \left(\frac{p_s R_s}{V_{\text{imp}}} \right) T_*^{-3/2}, \quad (7c)$$

with $\sigma=1$, $c_k=1.6 \times 10^{-16}$ J/keV, and $\mu_2=3 \times \int_0^1 f \times \hat{r}^2 d\hat{r} \approx 0.7$. The dimensionless variables [see Eqs. (8a) and (8b)] are written in terms of implosion velocity V_{imp} and adiabatic stagnation values for hot-spot radius R_s , pressure p_s , and central temperature T_s . The fraction of emitted energy that is lost \mathcal{L} (or reabsorbed \mathcal{R}) is normalized to its value at stagnation \mathcal{L}_s (or \mathcal{R}_s):

$$\tau = \frac{V_{\text{imp}}}{R_s} t, \quad \hat{p}(\tau) = \frac{p}{p_s}, \quad \hat{R}(\tau) = \frac{R_{\text{hs}}}{R_s}, \quad (8a)$$

$$\hat{\mathcal{L}}(\tau) = \frac{\mathcal{L}}{\mathcal{L}_s}, \quad \hat{\mathcal{R}}(\tau) = \frac{\mathcal{R}}{\mathcal{R}_s}, \quad \hat{T}(\tau) = \frac{T}{T_*},$$

$$T_* = \left(\frac{25 \mu_1}{36 \kappa_0} p_s R_s V_{\text{imp}} \right)^{2/7}. \quad (8b)$$

In Eqs. (7), the parameter γ is proportional to the ratio of the fraction of α -particle energy deposited in the hot spot and the initial shell kinetic energy, and β_1 [also β_2 in Eqs. (10)] is proportional to the ratio of the bremsstrahlung energy emitted from the hot spot and the initial shell kinetic energy.

2. Hot-Spot Mass Ablation and Temperature Equation

The heat and radiation flux leaving the hot spot are recycled back as internal energy and PdV work on the material ablated from the inner surface of the shell (illustrated in Fig. 143.6). We consider that only a fraction of the emitted bremsstrahlung energy (\mathcal{R}) causes ablation, while the remaining fraction \mathcal{L} is treated as a loss in energy [in Eq. (7a)]. Integrating Eq. (3) across the hot-spot boundary (or ablation front) as in Refs. 12, 14, and 15 and using the hot-spot mass ablation rate as $\dot{m}_{\text{abl}} = \rho V_{\text{abl}} = A p V_{\text{abl}}/T$ with $A = m_i/(1+Z)$ gives

$$\begin{aligned} \frac{5}{2A} \dot{m}_{\text{abl}} T_c R_{\text{hs}}^2 &= \frac{6}{5} \kappa_0 T_c^{7/2} R_{\text{hs}} \\ &+ \mathcal{R}(t) \frac{\mu_0}{3} C_b p^2 T_c^{-3/2} R_{\text{hs}}^3, \end{aligned} \quad (9)$$

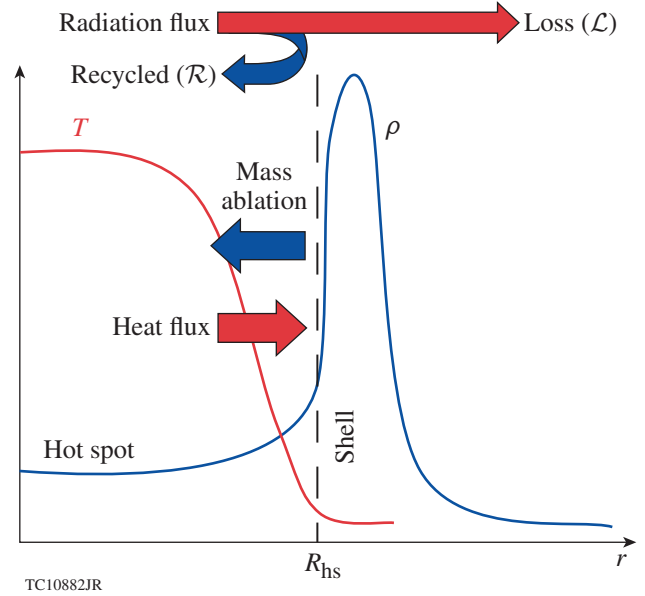


Figure 143.6

Density ρ and temperature T profiles during the deceleration phase of the implosion. The heat flux and a fraction of the emitted radiation energy are recycled back into the hot spot, causing mass ablation from the inner surface of the shell.

Equation (9) can be rewritten using the dimensionless variables in Eq. (8a) as

$$\frac{d}{d\tau} \left(\frac{\hat{p} \hat{R}^3}{\hat{T}} \right) = \hat{R} \hat{T}^{5/2} + \beta_2 \frac{\hat{p}^2 \hat{R}^3}{\hat{T}^{5/2}} \hat{R}(\tau), \quad (10a)$$

$$\beta_2 = \mathcal{R}_s \frac{2 \mu_0 C_b}{5 \mu_1} \left(\frac{p_s R_s}{V_{\text{imp}}} \right) T_*^{-3/2}, \quad (10b)$$

where $\mu_1 = 3 \times \int_0^1 f^{-1} \hat{r}^2 d\hat{r} \approx 1.69$. The ablation velocity includes contributions from both thermal and radiative components. It was calculated by balancing the heat and radiation flux leaving the hot spot with the mass ablation on the inner surface of the shell:

$$V_{\text{abl}} = \frac{12A}{25} \frac{\kappa_0 T_c^{5/2}}{\rho_{\text{shell}} R_{\text{hs}}} + \frac{2A \mu_0}{15} \frac{C_b p^2 T_c^{-5/2} R_{\text{hs}}}{\rho_{\text{shell}}} \mathcal{R}(t). \quad (11)$$

Mass ablation into the hot spot increases the hot-spot density and reduces the temperature but has no effect on the pressure.¹⁵

3. Solution of the Ignition Model

The system of equations governing the deceleration phase includes the hot-spot energy equation, the hot-spot mass equation, and the equation of motion for the imploding shell. They are summarized as follows:

$$\frac{d}{d\tau}(\hat{p}\hat{R}^5) = \gamma\hat{p}^2\hat{R}^5\hat{T}^\sigma - \beta_1\hat{p}^2\hat{R}^5\hat{T}^{-3/2}\hat{\mathcal{L}}(\tau), \quad (12a)$$

$$\frac{d}{d\tau}\left(\frac{\hat{p}\hat{R}^3}{\hat{T}}\right) = \hat{R}\hat{T}^{5/2} + \beta_2\frac{\hat{p}^2\hat{R}^3}{\hat{T}^{5/2}}\hat{\mathcal{R}}(\tau), \quad (12b)$$

$$\frac{d^2\hat{R}}{d\tau^2} = \hat{p}\hat{R}^2. \quad (12c)$$

The last equation [Eq. (12c)] considers the shell to be an incompressible thin piston but with finite mass M_{sh} . The *thin-shell* approximation is discussed in Ref. 14 and is compared to the more-accurate *thick-shell* model in Ref. 15. Although the latter is more accurate, it is substantially complicated and leads to the same ignition-scaling relations (but different proportionality constants). Since the hydrodynamic scaling of the deceleration phase is the primary objective of this article, the thin-shell model is used. The stagnation values for R_s , p_s , and T_s are obtained by solving Eqs. (12) adiabatically, i.e., without α -energy deposition in the hot spot ($\gamma = 0$) and radiation ($\beta_1, \beta_2 = 0$). This leads to relations between the initial and stagnation parameters; the energy conservation requires that $M_{\text{sh}}V_{\text{imp}}^2 = 4\pi p_s R_s^3$ [from Eq. (12c)] and adiabatic compression requires $p(0)R(0)^5 = p_s R_s^5$ [from Eq. (12a)]. Rewriting Eq. (9) in dimensionless form as Eq. (10a) gives $T_* \approx 1.3 T_s$ [in Eq. (8b)]. The initial conditions $\hat{p}(0) = \varepsilon^{-5/2}$, $\hat{R}(0) = \varepsilon^{1/2}$, $\hat{T}(0) = \varepsilon^{-1/2}$, and $\hat{\dot{R}}(0) = -1$ are written in terms of the dimensionless parameter $\varepsilon = M_{\text{sh}}V_{\text{imp}}^2 / 4\pi p(0)R(0)^3 \gg 1$, which is the ratio of the shell's kinetic energy and the hot spot's internal energy at the beginning of the deceleration phase (see Ref. 12). The thin-shell model overestimates the conversion of the shell's kinetic energy to the hot spot (i.e., 100% conversion); in order to limit this transfer, a heuristic finite shell-thickness correction (developed in Ref. 16) was used. Using this correction, the constants in Eqs. (7b), (7c), and (10b) can be rewritten in terms of $\rho\Delta$ (kg/m²) of the shell and T_* (keV) as

$$\gamma = C_\alpha(\rho\Delta)^{3/4}T_*^{-15/8}, \quad (13a)$$

$$\beta_1 = C_{\beta_1}(\rho\Delta)^{3/4}T_*^{-5/8},$$

$$\beta_2 = C_{\beta_2}(\rho\Delta)^{3/4}T_*^{-5/8}, \quad (13b)$$

where

$$C_\alpha = 1.77 \times 10^{-3} \text{ keV}^{-15/8} \text{ m}^{3/2} \text{ kg}^{-3/4},$$

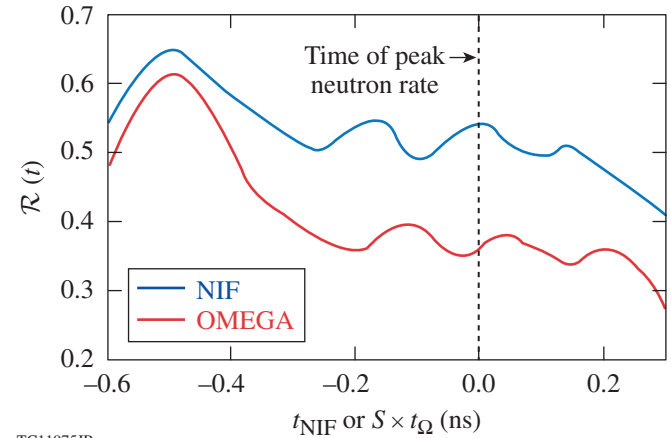
$$C_{\beta_2} = \mathcal{R}_s \times 0.327 \text{ keV}^{5/8} \text{ m}^{3/2} \text{ kg}^{-3/4},$$

and

$$C_{\beta_1} = 2.75 \times (\mathcal{L}_s / \mathcal{R}_s) C_{\beta_2}.$$

For a direct-drive ignition-scale target, the fraction of bremsstrahlung radiation energy reabsorbed by the shell is shown by the blue curve in Fig. 143.7; at stagnation, \mathcal{R}_s is 0.54 and $\beta_1 = 2.34 \times \beta_2$. The hot-spot model [Eqs. (12)] is solved numerically with a large value for ε ($\sim 10^4$). The solution for \hat{p} , \hat{T} , and \hat{R} for a given value of β_1 becomes singular if γ exceeds a critical value γ_{ign} . The γ_{ign} curve shown in Fig. 143.8 is fit with a polynomial as

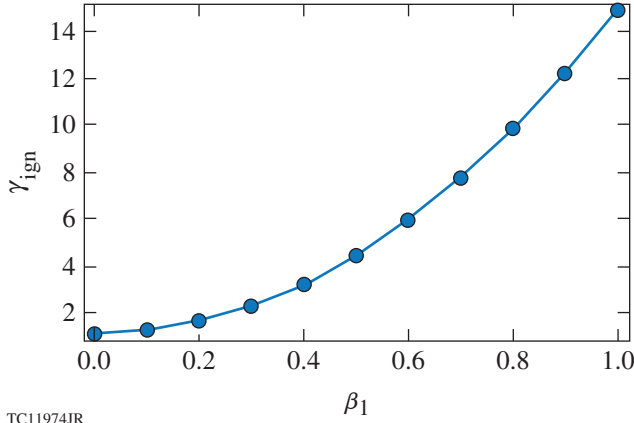
$$\gamma_{\text{ign}} \approx 1.13 + 0.29\beta_1 + 1.89\beta_1^2. \quad (14)$$



TC11975JR

Figure 143.7

The fraction of emitted bremsstrahlung energy from the hot spot that is reabsorbed by the shell (\mathcal{R}) versus normalized NIF time ($S = 4$) is shown for the hydro-equivalent implosions on the NIF (blue) and OMEGA (red) scales. The remaining fraction of the emitted energy (\mathcal{L}) accounts for the radiation losses.



TC11974JR

Figure 143.8

 Plot of γ_{ign} versus β_1 . When $\gamma \geq \gamma_{\text{ign}}$, the solution to Eqs. (12) becomes singular.

The analytic ignition parameter obtained from scaling [Eq. (13a)] can be normalized using the critical value from the model [Eq. (14)] and represented in terms of the no- α quantities; therefore, the no- α hot-spot–ignition condition is given by $\chi_{\text{no } \alpha} = \gamma / \gamma_{\text{ign}} \geq 1$. A more-elaborate compressible model (in Ref. 17) yields the same scaling as Eqs. (13a) and (14) but with different constants of proportionality. The scaling of the ignition parameter $\chi_{\text{no } \alpha}$ can be approximated (as first shown in Ref. 18) with

$$\chi_{\text{no } \alpha} \equiv (\rho R_n)^{0.8} \left(\frac{T_n}{4.7} \right)^{1.6} \text{YOC}^{0.4}, \quad (15)$$

where ρR_n and T_n are the 1-D neutron-averaged areal density in g/cm^2 and temperature in keV, respectively, and a value of $\chi_{\text{no } \alpha} \geq 1$ implies hot-spot ignition. All the quantities in Eq. (15) are evaluated without α -particle deposition. Here, YOC is the ratio of the neutron yield from no- α two-dimensional (2-D) simulations and yield from no- α 1-D simulations. Since alpha heating is negligible in OMEGA implosions, the first step of an OMEGA-to-NIF extrapolation requires using the no- α performance (i.e., $\chi_{\text{no } \alpha}$). Based on the extrapolated value of $\chi_{\text{no } \alpha}$ for a NIF target, one can then determine the level of alpha heating on the NIF. If, after the extrapolation from OMEGA to the NIF, the value of $\chi_{\text{no } \alpha}$ is unity, one can then conclude that the NIF target would have ignited.

4. Hydro-Equivalent Scaling of the Deceleration Phase

In this section we consider the hydrodynamic scaling of the deceleration-phase RTI. The growth rate for the deceleration-phase RTI in the linear regime can be approximated with¹⁹

$$\Upsilon_{\text{RT}} = \alpha \sqrt{\frac{k \langle g \rangle}{1 + k \langle L_{\text{min}} \rangle}} - \beta k \langle V_{\text{abl}} \rangle, \quad (16)$$

where $\langle g \rangle$ is the average acceleration, $\langle L_{\text{min}} \rangle$ is the average minimum density-gradient scale length, $\langle V_{\text{abl}} \rangle$ is the average ablation velocity, and the coefficients α and β are 0.9 and 1.4, respectively. As shown in Ref. 20, increasing V_{abl} and L_{min} reduces the RTI growth rate and the unstable spectrum exhibits a cutoff around $\ell \approx 90$. The stabilizing terms depend on the thermal and radiation transport in the hot spot. The neperes of the deceleration-phase RTI scale as

$$\begin{aligned} N_e^{\text{RT}} &= \alpha \sqrt{\frac{k \langle g \rangle t^2}{1 + k \langle L_{\text{min}} \rangle}} - \beta k \langle V_{\text{abl}} \rangle t \\ &\sim \alpha \sqrt{\frac{\ell (c_{\text{sh}}^2 / V_{\text{imp}}^2)}{1 + \ell (L_{\text{min}} / R_{\text{hs}})}} - \beta \ell \left(\frac{V_{\text{abl}}}{V_{\text{imp}}} \right). \end{aligned} \quad (17)$$

Equation (17) was written in dimensionless form using $k = \ell / R_{\text{hs}}$, $t \sim R_{\text{hs}} / V_{\text{imp}}$, and the sound speed in shell $c_{\text{sh}}^2 \sim P_{\text{sh}} / \rho_{\text{sh}}$. The inertia of the shell is balanced by the hot-spot pressure as $M_{\text{sh}} \ddot{R}_{\text{hs}} = 4\pi R_{\text{hs}}^2 P_h$ with $M_{\text{sh}} \sim \rho_{\text{sh}} R_{\text{hs}}^2 \Delta$; this was used to determine the scaling of the shell acceleration $\ddot{R}_{\text{hs}} \equiv g \sim (c_{\text{sh}}^2 / R_{\text{hs}})$. To determine the scaling of the stabilizing terms, i.e., $(V_{\text{abl}} / V_{\text{imp}})$ and $(L_{\text{min}} / R_{\text{hs}})$, it is necessary to determine the scaling of the thermal conduction and radiation transport in the hot spot and how they differ from the acceleration phase.

Thermal conduction, radiation, and α transports are typically modeled using diffusive terms. The diffusive terms in spherically converging geometry [i.e., $r^{-2} \partial_r (r^2 \partial_r Q)$, where r is the radial coordinate and Q is the diffused quantity] can be written in the reference frame of the ablation front as

$$\frac{1}{(R_{\text{abl}} + \zeta)^2} \frac{\partial}{\partial \zeta} \left[(R_{\text{abl}} + \zeta)^2 \frac{\partial}{\partial \zeta} Q \right], \quad (18)$$

where $\zeta = r - R_{\text{abl}}$, with R_{abl} representing the position of the ablation front. During the acceleration phase, the distance between the critical-density surface where the laser (or x-ray) energy is absorbed and the ablation front corresponds to the region where energy is diffused, i.e., $\zeta \sim (R_c - R_{\text{abl}})$. For

ICF implosions this distance is small compared to R_{abl} , i.e., $(\zeta/R_{\text{abl}}) \sim 0.1 \ll 1$. Therefore, the thermal diffusion term reduces to planar geometry [i.e., $(\partial^2/\partial\zeta^2)Q$] and the convergence effects can be neglected for the outer ablation-front surface. Therefore, the ablative stabilization term (derived in Ref. 11) can be written as $V_{\text{abl}}/V_{\text{imp}} \sim \dot{m}_{\text{abl}}(I_L)\alpha_0^{3/5}/P_{\text{abl}}^{3/5}(I_L)V_{\text{imp}}$, and the outer-surface ablative RTI scales hydro-equivalently as long as I_L , α_0 , and V_{imp} are kept constant. Instead, during the deceleration phase, $\zeta/R_{\text{abl}} \sim 1$; therefore, the convergence effects are significant and the diffusive terms do not scale hydro-equivalently.

Using the scaling relation for the temperature at target center as $T_c \sim E^{0.07} \sim R^{0.21}$, the ablation velocity [Eq. (11)] scales with the target size as

$$\left(\frac{V_{\text{abl}}}{V_{\text{imp}}}\right) \sim \frac{\kappa_0 T_c^{5/2}}{\rho_{\text{sh}} R_{\text{hs}}} \sim \frac{1}{\sqrt{R}}. \quad (19)$$

The temperature scaling was first derived in Ref. 21 and can be retrieved analytically since $T_* \sim T_c \sim R^{2/7}$ from the temperature relation in Eq. (8b) (with V_{imp} and p_s as the constants in scaling). Equation (19) indicates that larger targets exhibit lower ablative stabilization. It will be shown in **Effect of Thermal Conduction: ($V_{\text{abl}}/V_{\text{imp}}$) Scaling** (p. 133) that scaling of the ablative stabilization caused by $(V_{\text{abl}}/V_{\text{imp}})$ is determined solely by thermal conduction, whereas scaling of the finite density-gradient scale-length stabilization $(L_{\text{min}}/R_{\text{hs}})$ is determined by radiation transport (see p. 135). The Atwood number in Eq. (16) for finite L_{min} can be written as

$$A_T \equiv \frac{1}{1 + kL_{\text{min}}} \sim \frac{1}{1 + \ell(L_{\text{min}}/R_{\text{hs}})}. \quad (20)$$

Reabsorption of radiation on the inner surface of the shell enhances the scale length such that $\langle kL_{\text{min}} \rangle \sim 1$ for $\ell < 60$ and $\langle kL_{\text{min}} \rangle \gg 1$ for $\ell > 60$. Therefore, it is useful to assess the scaling of radiation transport using $(L_{\text{min}}/R_{\text{hs}})$ as the normalized scaling parameter. It is shown from simulations (see p. 135) that for NIF-like targets $(L_{\text{min}}/R_{\text{hs}})_{\text{NIF}} \sim 0.1$, while for OMEGA targets $(L_{\text{min}}/R_{\text{hs}})_{\Omega} \sim 0.07$. Since $[(L_{\text{min}}/R_{\text{hs}})_{\text{NIF}}/(L_{\text{min}}/R_{\text{hs}})_{\Omega}] \sim 1.5$, stabilization by L_{min} is enhanced for larger targets, which is an opposite trend compared to ablative stabilization.

Alpha-particle transport is not considered because the hot-spot-ignition condition $\chi_{\text{no } \alpha}$ uses no- α parameters. The alpha particles stopped within the hot spot augment the hot-

spot temperature, and those leaking out of the hot spot deposit their energy on the inner shell surface, driving mass ablation. As shown in Ref. 22, both mechanisms enhance the ablative stabilization of the RTI. In a NIF-size target close to ignition, the stabilization of the RTI from alpha-driven ablation is significant. Even though we use a no- α extrapolation of $\chi_{\text{no } \alpha}$ from OMEGA to the NIF, the alpha-driven ablative stabilization is included through the value of the power index of the YOC [Eq. (15)]. This is discussed in Ref. 7, where it is shown that without ablative stabilization, the power index of the YOC would have been larger (≈ 0.8). It is because of the ablative stabilization that the power index is reduced by half (≈ 0.4), indicating that implosions close to ignition are less affected by the deceleration-phase RTI as the instability growth rates are reduced by alpha-driven mass ablation.

5. Hydro-Equivalent Scaling of the Yield-Over-Clean

The scaling of the Lawson parameter in Eq. (15) using $\rho R \sim E^{1/3}$ and $T \sim E^{0.07}$ can be written as

$$\chi_{\text{no } \alpha} \sim E^{0.38} \text{YOC}_{\text{no } \alpha}^{0.4}. \quad (21)$$

The hydro-equivalent ignition condition on OMEGA considering $E_{\text{NIF}}/E_{\Omega} \sim 64$ is $\chi_{\Omega} = 0.21(\text{YOC}_{\Omega}/\text{YOC}_{\text{NIF}})^{0.4}$. Since the normalized surface-roughness level on NIF targets is $\sim 4\times$ lower than on OMEGA targets, i.e., $(\sigma_{\text{ice}}^{\Omega}/R_{\Omega})/(\sigma_{\text{ice}}^{\text{NIF}}/R_{\text{NIF}}) \sim 4$, the hydro-equivalent ignition condition on OMEGA improves (see Ref. 11) to

$$\chi_{\Omega} = 0.19 \left(\frac{\text{YOC}_{\Omega}}{\text{YOC}_{\text{NIF}}} \right)^{0.4}. \quad (22)$$

The small improvement in the ignition condition from 0.21 to 0.19 occurs only by considering the above-mentioned surface roughness scaling and assumes equal growth factors between NIF and OMEGA during the deceleration phase. Here we also assumed that the laser imprint level on direct-drive OMEGA and extrapolated direct-drive ignition-scale implosions is equal. This choice refers to the most-stringent ignition condition on OMEGA (discussed in Ref. 11).

The yield degradation resulting from the deceleration-phase RTI can occur for two physical reasons: a reduction in the clean volume (i.e., volume within RT spikes) and a reduced coupling of the shell's kinetic energy to hot-spot pressure as the energy is used to drive the RTI. A simple estimate for the YOC, assuming a reduction of the clean volume only (i.e., without considering a drop in hot-spot pressure and temperature compared to without RTI), leads to

$$\text{YOC} \sim \left(\frac{V_c}{V_{1-D}} \right) = \left(1 - \frac{\sigma_0 G_{\text{RT}}}{R_{1-D}} \right)^3, \quad (23)$$

where R_{1-D} is the hot-spot radius in 1-D (i.e., without considering deceleration RTI), $V_c \sim (R_{1-D} - \sigma_0 G_{\text{RT}})^3$ is the hot-spot clean volume under the RTI spikes, σ_0 is the initial perturbation on the inner surface, and G_{RT} is the total growth factor of the RTI spikes into the hot spot. The YOC's from the implosions of the two scales (NIF and OMEGA) are related through the following equation:

$$\text{YOC}_{\text{NIF}} = \left[1 - \left(\frac{\sigma_0^{\text{NIF}} G_{\text{RT}}^{\text{NIF}}}{\sigma_0^{\Omega} G_{\text{RT}}^{\Omega}} \right) \left(\frac{R_{1-D}^{\Omega}}{R_{1-D}^{\text{NIF}}} \right) (1 - \text{YOC}_{\Omega}^{1/3}) \right]^3. \quad (24)$$

The ablative stabilization of the deceleration-phase RTI is different on the two scales, resulting in different growth factors. Simulations have been performed to determine the scaling of G_{RT} and YOC and to predict the hydro-equivalent ignition condition on OMEGA.

Hydro-Equivalent Implosion Design and Simulations of Deceleration-Phase RTI

This section describes the design and performance of the set of hydro-equivalent implosions used in this article. The 2-D simulations of the deceleration phase using the Eulerian radiation-hydrodynamics code *DEC2D/3D*^{23–25} are also described.

The OMEGA-scale target shown in Fig. 143.9(a) is similar to those used in current cryogenic implosions performed on OMEGA.²⁶ This target had an 11- μm plastic (CD) ablator, 41 μm of DT ice, and a 431- μm outer radius. It was imploded with 27 kJ of laser energy, and when simulated with the

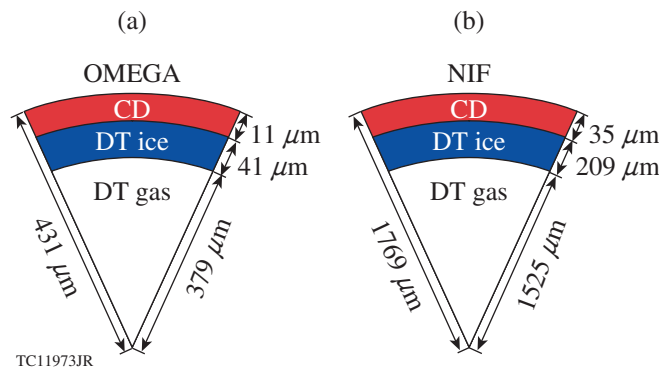


Figure 143.9 Target specifications for (a) an OMEGA-scale and (b) a NIF-scale cryogenic implosion simulation.

1-D hydrocode *LILAC*,²⁷ it achieved an implosion velocity of ~ 360 km/s with an average in-flight adiabat of 3. The hydro-equivalent NIF-scale target [Fig. 143.9(b)] was designed by scaling up the radius of each layer roughly by a factor of 4 since the laser energy was scaled $64\times$ to 1.8 MJ. The NIF-scale target had a 35- μm -thick CD ablator, a 209- μm -thick DT ice layer, and a total radius of 1769 μm . The laser intensity I_L versus normalized time (t/t_{bang}) was kept unchanged [see Fig. 143.10(a)]. The time of peak neutron production, t_{bang} , was 11.42 ns and 2.83 ns for NIF and OMEGA implosions, respectively. The

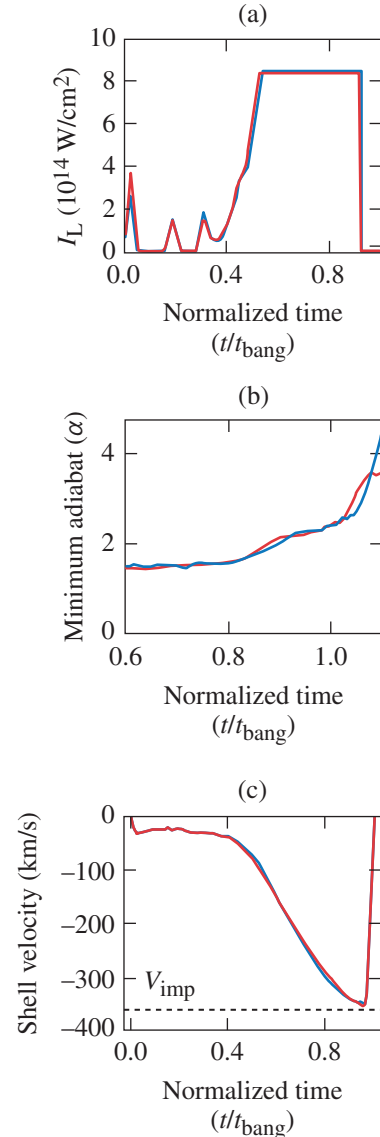


Figure 143.10 Time history of the essential hydrodynamic parameters (a) laser intensity I_L , and (b) fuel adiabat α , and (c) implosion velocity V_{imp} versus normalized time (t/t_{bang}) for the NIF-scale (blue) and hydro-equivalent OMEGA-scale (red) implosions.

target thickness had to be modified slightly to account for the non-scalable effects of radiation preheat in the acceleration phase. This arises because the radiation mean free path (ℓ_m) is the same in both target scales but the thickness of the ablator (CD) layer is $4\times$ less on the OMEGA target, resulting in a lower preheat shielding. To keep the same fuel adiabat [see Fig. 143.10(b)] for implosions of different scales, some of the CD ablator was mass equivalently exchanged with DT ice for the larger targets.¹¹ The implosion velocity for targets of both scales is the same [shown in Fig. 143.10(c)]. The time evolution of the in-flight aspect ratio (IFAR) and the pressure profiles at stagnation P_s for the targets of both scales match closely (see Fig. 143.11), showing that the implosions are in accordance with the theory for 1-D hydro-equivalent scaling.¹¹ Energy in radiation flux leaving the hot-spot boundary [i.e., $(1/e)\rho_{\max}$ and ρ_{\max} (peak of shell density)] was measured. These measure-

ments were used to calculate the fraction of emitted energy that was reabsorbed, $\mathcal{R}(t)$ (see Fig. 143.7), and the fraction that was lost, $\mathcal{L}(t)$. The minimum density-gradient scale length L_{\min} and ablation velocity $V_{\text{abl}} = (\dot{M}_{\text{hs}}/4\pi R_{\text{hs}}^2 \rho_{\text{shell}})$ at the inner surface of the shell were calculated. Radiation transport was turned on/off during the deceleration phase to study the individual effects of thermal conduction and radiation transport on the scaling of V_{abl} and L_{\min} .

The effects of the RTI on the deceleration phase of ICF implosions were studied using the hydrodynamic code *DEC2D/3D*.²⁵ The radial profiles of density, pressure, velocity, and temperature were extracted at the end of the acceleration phase (i.e., when the laser is turned off) from the 1-D NIF-scale simulation. The hydro-equivalent OMEGA profiles were generated by scaling down the size by a factor of 4, producing implosions with an exactly hydro-equivalent acceleration phase; therefore, an exclusive study of the scaling of the deceleration phase is possible. The profiles were mapped onto a 2-D high-resolution grid with single- or multimode velocity perturbations applied at the inner surface of the shell. The velocity perturbations were identical (i.e., hydro-equivalent) on both scales. The deceleration RTI developed at the unstable interface and degraded the implosion performance by reducing the clean volume. Thermal transport, α transport, and multigroup radiation transport were modeled as diffusion processes. Each of these can be turned on/off in the simulation. Since the no-burn case is considered in this article, the α -energy deposition was turned off. In **Effect of Thermal Conduction: ($V_{\text{abl}}/V_{\text{imp}}$) Scaling** (see p. 133), radiation transport was turned off. The next subsection discusses results where both thermal and radiation transport processes were included.

The 2-D axisymmetric simulations (considering ϕ symmetry) were performed on a cylindrical x - z plane over a 90° wedge, with a high resolution of 900×900 grids for the hot spot and shell assembly on both scales. *DEC2D* is an Eulerian radiation-hydrodynamics code²³ with a moving mesh that shrinks radially with the average velocity and maintains a high resolution throughout the convergence during the deceleration phase (i.e., by a factor of ~ 3 to 5). The conservation equations are rewritten in a new dimensionless coordinate system $\xi = r/R(t)$ and $\zeta = z/Z(t)$, where $R(t)$ and $Z(t)$ are assigned functions of time. The computational domain is described by the Eulerian coordinates ξ and ζ varying between 0 and 1. There is no direct remapping involved. Since the actual spatial domain in r and z is compressed in time as a result of the prescribed inward motion of $R(t)$ and $Z(t)$, the high resolution

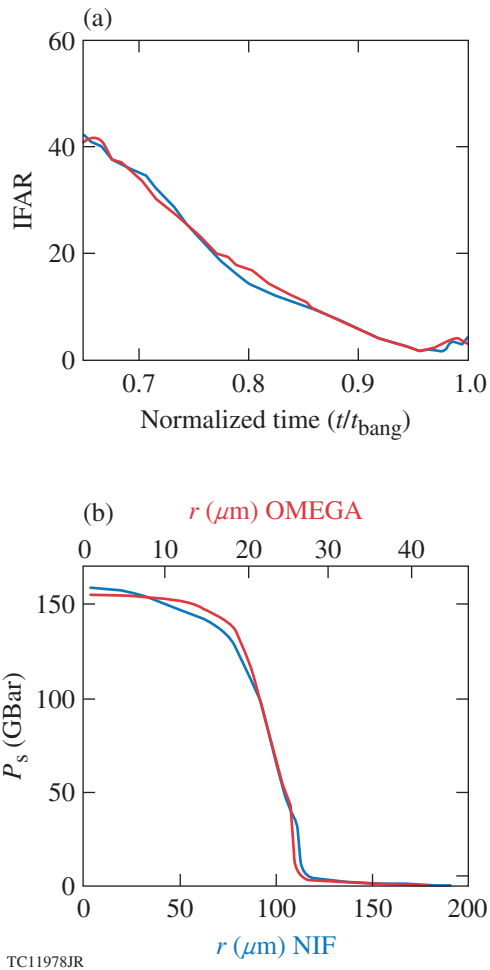


Figure 143.11

(a) In-flight aspect ratio (IFAR) versus normalized time (t/t_{bang}) and (b) pressure at stagnation (P_s) versus radial distance for the NIF-scale (blue) and hydro-equivalent OMEGA-scale (red) implosions.

(900 × 900) is preserved throughout the real spatial domain for the entire simulation. The accuracy has been verified through convergence tests and is good enough to resolve modes up to $\ell = 100$. We use both a second-order centered MacCormack²⁸ scheme with artificial viscosity and second-order HLLC (Harten–Lax–Van Leer–Contact) Riemann solvers²⁹ without artificial viscosity. Earlier versions of *DEC2D* have been used to study the ablative stabilization of the deceleration-phase RTI in Refs. 15 and 20.

Single-mode simulations for a mode number ℓ varying from 2 to 68, with three different initial velocity perturbation amplitudes⁷ ($\Delta V/V_{\text{imp}}$)—0.01%, 0.05%, and 0.1% of implosion velocity V_{imp} —were carried out. The $\Delta V/V_{\text{imp}}$ was chosen to keep the RTI within the linear regime. The time of peak neutron production, t_{bang} , was 1 ns after the laser was turned off on the NIF scale and 250 ps on the OMEGA scale. The single-mode growth factor was calculated as the ratio of the amplitudes at t_{bang} and at $t_{\text{bang}} - 800$ ps into simulation on the NIF scale (or $t_{\text{bang}} - 200$ ps on OMEGA).

Multimode simulations were carried out by including modes $2 \leq \ell \leq 68$. An ℓ^{-2} roll-off spectrum for mode numbers $\ell > 20$ and a constant amplitude for $2 \leq \ell \leq 20$ were used. Simulations were repeated by varying $\Delta V/V_{\text{imp}}$ from 0 (unperturbed) to 4%. The YOQ ($\text{yield}_{2\text{-D}}/\text{yield}_{1\text{-D}}$) was calculated for implosions on both scales. Simulations with an alternative ℓ^{-1} roll-off spectrum show good agreement with these results.

Non-Hydro-Equivalent Physics of the Deceleration Phase

The scaling of the deceleration-phase RTI is determined by scaling the stabilization resulting from mass ablation ($V_{\text{abl}}/V_{\text{imp}}$) and density-gradient scale length ($L_{\text{min}}/R_{\text{hs}}$), which can be understood by studying the effect of thermal conduction and radiation transport during this phase. This section presents the results from simulations and compares them to the analytic scaling.

1. Effect of Thermal Conduction: ($V_{\text{abl}}/V_{\text{imp}}$) Scaling

The analytical scaling of ($V_{\text{abl}}/V_{\text{imp}}$) shown in Eq. (19) can be rewritten using the radius and time-scaling factor $S \equiv R_{\text{NIF}}/R_{\Omega} = 4$ as

$$\frac{V_{\text{abl}}^{\text{NIF}}}{V_{\text{abl}}^{\Omega}} \sim \left(\frac{R_{\text{NIF}}}{R_{\Omega}}\right)^{-0.5} \sim 0.5. \quad (25)$$

On OMEGA the hot-spot mass density at stagnation ρ_s is higher and the hot-spot temperature T_s is lower than on NIF-

scale implosions (see Fig. 143.12), leading to the 1-D scaling of hot-spot temperature as $T \sim R^{0.21}$. This can be attributed to the higher mass ablation rate on OMEGA, which is in qualitative accordance with Eq. (25). The pressure at stagnation P_s is the same on both scales, showing hydro-equivalence.

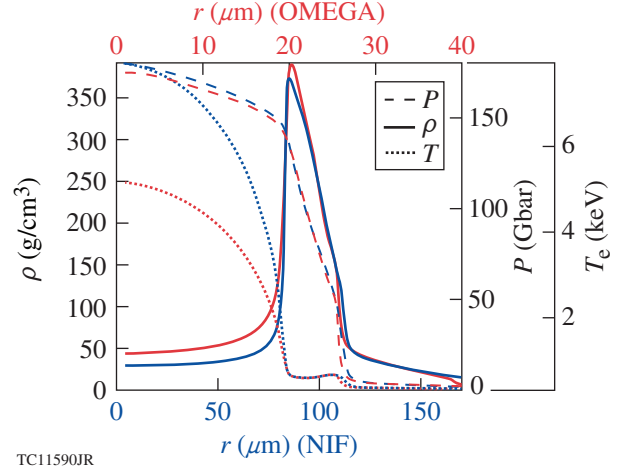


Figure 143.12

Pressure P , density ρ , and temperature T at time of peak neutron rate t_{bang} versus radial distance for NIF-scale (blue) and OMEGA-scale (red) implosions. Simulations were performed using the 1-D code *LILAC*, including thermal conduction (without radiation transport) during the deceleration phase.

The V_{abl} for the implosions of both scales is shown in Fig. 143.13(a). It is clearly seen that thermal conduction determines the scaling of ablation velocity (i.e., $V_{\text{abl}}/V_{\text{imp}}$) because including radiation transport has no effect on the scaling of V_{abl} since it enhances the V_{abl} on both scales equally. Simulations show that

$$\left(\frac{V_{\text{abl}}^{\text{NIF}}}{V_{\text{abl}}^{\Omega}}\right)_{\text{no rad}} \sim \left(\frac{V_{\text{abl}}^{\text{NIF}}}{V_{\text{abl}}^{\Omega}}\right)_{\text{rad}} \sim 0.6, \quad (26)$$

which agrees with the analytical scaling in Eq. (25).

The normalized density-gradient scale length ($L_{\text{min}}/R_{\text{hs}}$) arising from thermal conduction is rather small and has almost no effect on the scaling of the deceleration-phase RTI. From Fig. 143.13(b), considering the simulations without radiation, the normalized scale lengths at stagnation are $(L_{\text{min}}/R_{\text{hs}})_{\text{NIF}} \sim 0.02$ and $(L_{\text{min}}/R_{\text{hs}})_{\Omega} \sim 0.05$. Since $L_{\text{min}}/R_{\text{hs}} \ll 1$ on both scales, it affects only the very high ℓ modes that are already stabilized by ablation and has little effect on the scaling of the deceleration RTI [see Eq. (20)].

While the classical RTI (i.e., no ablation) is exactly hydro-equivalent [see Figs. 143.14(a) and 143.15(a)], the ablative stabilization caused by thermal transport does not scale hydro-equivalently [Fig. 143.14(b)] with the OMEGA target exhibiting higher stabilization.

To study the effect of (V_{abl}/V_{imp}) scaling (i.e., thermal conduction) on the deceleration-phase RTI, a series of single-mode simulations without radiation transport (i.e., only thermal transport) for different ℓ numbers were carried

out. Hydro-equivalent velocity perturbations with a single cosine mode were imposed on the inner surface of the shell. Short-wavelength modes exhibit higher ablative stabilization because of thermal conduction [see Eq. (17) and Fig. 143.15(b)]. The growth factors on the NIF are $\sim 2.7\times$ those on OMEGA, which is in agreement to the scaling in Eq. (17). Multimode simulations show that differences in the deceleration phase of hydro-equivalent implosions have an effect on the YOC ratio, with $YOC_{\Omega} > YOC_{NIF}$ by $\sim 25\%$ when the RTI becomes highly nonlinear (near saturation).

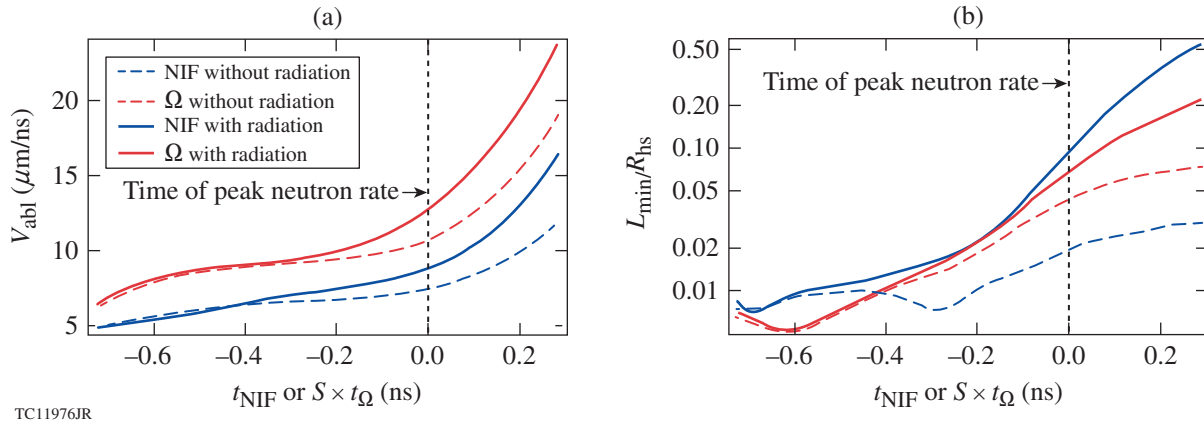


Figure 143.13 (a) Ablation velocity V_{abl} and (b) normalized density scale length L_{min}/R_{hs} versus normalized NIF time ($S = 4$) for NIF (blue) and OMEGA (red) implosions. Simulations were performed using the 1-D code *LILAC*, with (solid lines) and without (dashed lines) radiation transport for the deceleration phase.

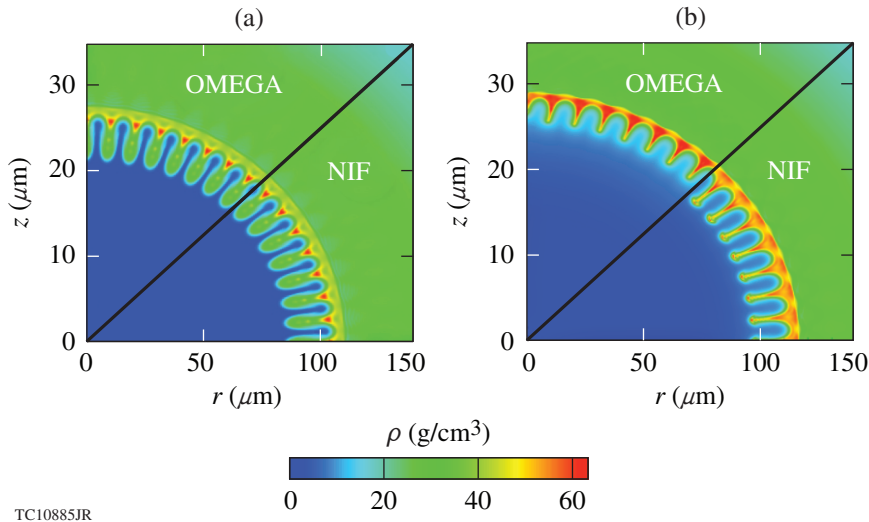
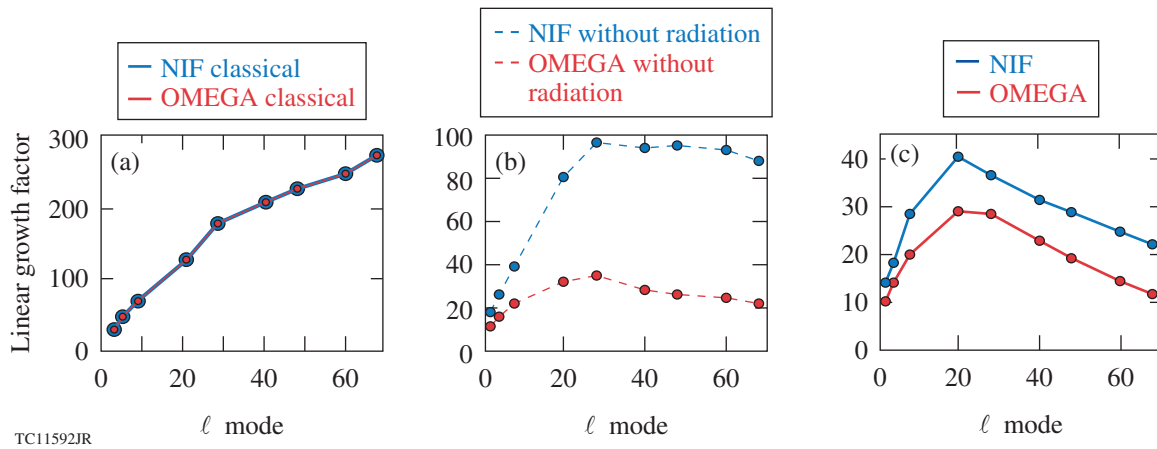


Figure 143.14 Density plots at hydro-equivalent times showing $\ell = 60$ deceleration RT growth on OMEGA (top half) and the NIF (lower half). (a) Simulations without thermal conduction on both scales match perfectly, illustrating that classical RTI is exactly hydro-equivalent. (b) Simulations with ablation caused by thermal transport (only) do not scale hydro-equivalently, resulting in different RT growth.



TC11592JR

Figure 143.15

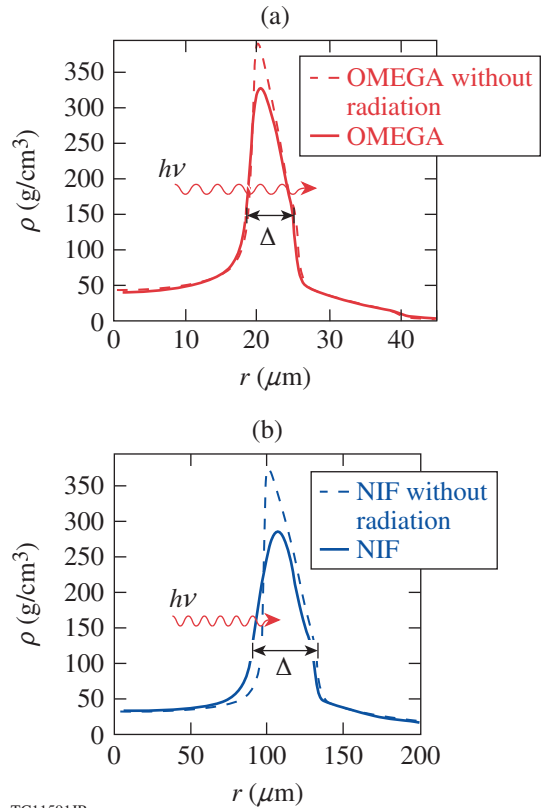
Deceleration-phase RTI linear growth factors versus mode number ℓ for NIF (blue) and OMEGA (red) hydro-equivalent implosions. (a) The classical growth factor, (b) growth factors with thermal transport (i.e., without radiation transport), and (c) growth factors with stabilization related to both thermal and radiation transport are shown.

2. Effect of Radiation Transport: (L_{\min}/R_{hs}) Scaling

In this subsection we discuss the scaling of the RTI stabilization mechanism caused by reabsorption of bremsstrahlung emission from the hot spot. As the central plasma is heated by compression during the deceleration phase, it emits bremsstrahlung radiation. Some of the radiation emitted from the hot spot is absorbed on the inner surface of the shell, causing mass ablation and increasing L_{\min} and V_{abl} during the last 400 ps (NIF-scale time) before bang time t_{bang} (see Fig. 143.13). The mean free path (mfp) of photons with energy $h\nu$ (in DT plasma) is given by the Kramers formula¹³

$$l \approx 2.25 \times 10^4 \frac{\sqrt{T} (h\nu)^3}{\rho^2}, \quad (27)$$

where l is in μm , the electron temperature T and photon energy $h\nu$ are in keV, and the density of plasma ρ is in g/cm^3 . Photons emitted in a 5-keV hot spot exhibit an mfp of $2500 \mu\text{m}$ in the hot spot (considering a mass density of $50 \text{ g}/\text{cm}^3$) and an mfp of $20 \mu\text{m}$ in the cold (200-eV) shell with a mass density of $250 \text{ g}/\text{cm}^3$. The shell thickness for a typical NIF-scale target near stagnation is $\sim 50 \mu\text{m}$, whereas for a hydro-equivalent OMEGA target, the shell is $4\times$ thinner ($\sim 12.5 \mu\text{m}$). Consequently, more of the radiation emitted from the hot spot is reabsorbed by the NIF shell (see Fig. 143.7). The fraction of emitted energy that is reabsorbed by the shell at stagnation (\mathcal{R}_s) is greater on the NIF (0.54) than on OMEGA (0.36). As a result of higher reabsorption, the density-gradient scale length is more enhanced in the NIF target than in the OMEGA target (see Fig. 143.16). A quantitative mea-



TC11591JR

Figure 143.16

Density profiles at time of peak neutron rate for hydro-equivalent (a) OMEGA and (b) NIF implosions. It is shown that radiation reabsorbed by the NIF shell results in a greater enhancement of the scale lengths for the NIF with respect to the OMEGA target.

sure is provided in Fig. 143.13(b); by adding radiation transport to the simulations, the scale length (L_{\min}/R_{hs}) increases by fivefold on the NIF scale, whereas the change is only a factor of 1.6 on OMEGA. Since there is a broad spectrum of emission frequency ν from the hot spot, the photons absorbed deeper in the shell enhance the density scale length; therefore, radiation transport determines the scaling of L_{\min} in hydro-equivalent implosions:

$$\left(\frac{L_{\min}^{\text{rad}}}{L_{\min}^{\text{no rad}}}\right)_{\text{NIF}} > \left(\frac{L_{\min}^{\text{rad}}}{L_{\min}^{\text{no rad}}}\right)_{\Omega}. \quad (28)$$

A comparison of the central hot-spot temperatures for the simulations with and without radiation transport show that radiation transport has little effect on the scaling of the temperature with target size, unlike thermal conduction. The scaling of the temperature²¹ with target size is $T_c \sim R^{0.28}$ without considering radiation transport, and it changes to $T_c \sim R^{0.21}$ when radiation transport is included.

The effect of the (L_{\min}/R_{hs}) scaling on the linear RTI growth factors is shown in Fig. 143.15(c). The RTI on the NIF-scale implosion experiences higher stabilization from enhanced density gradients compared to OMEGA for the same initial perturbation $\Delta V/V_{\text{imp}}$. Similar studies on another target with a high implosion velocity (~ 430 km/s) showed identical trends. Comparing Figs. 143.15(b) and 143.15(c) shows that stabilization of the deceleration-phase RTI caused by ablation velocity ($V_{\text{abl}}/V_{\text{imp}}$) and density scale length (L_{\min}/R_{hs}) scales oppositely with target size. The sta-

bilization related to V_{abl} is predominant on the smaller target, resulting in $(G_{\text{RT}}^{\text{NIF}}/G_{\text{RT}}^{\Omega})_{\text{no rad}} \sim 2.7$, whereas the stabilization related to L_{\min}/R_{hs} scales inversely and reduces the difference to $(G_{\text{RT}}^{\text{NIF}}/G_{\text{RT}}^{\Omega})_{\text{rad}} \sim 1.35$. The impact of thermal conduction is more significant on the scaling of the RTI. The results of single-mode linear growth factors including both thermal conduction and radiation transport show that deceleration-phase RTI growth factors on NIF implosions are $\sim 35\%$ higher than on hydro-equivalent OMEGA implosions.

Scaling of the Ignition Condition

Multimode simulations (see Fig. 143.17) with hydro-equivalent initial perturbations (i.e., equal $\Delta V/V_{\text{imp}}$, described on p. 131) were used to calculate the $\text{YOC}_{\Omega}/\text{YOC}_{\text{NIF}}$ ratio [see Fig. 143.18(a)]. Increasing the nonuniformities results in higher YOC ratios, until the RTI becomes highly nonlinear (as in Fig. 143.17) and saturates at

$$\left(\frac{\text{YOC}_{\Omega}}{\text{YOC}_{\text{NIF}}}\right) \sim 1.17. \quad (29)$$

The scaling of the deceleration-phase RTI discussed in earlier sections is applicable to the linear and moderately nonlinear regimes of the instability. In the highly nonlinear regime the RTI saturates and this phase of the instability scales equivalently (from simulations); therefore, the YOC ratio asymptotes as shown in Fig. 143.18(a). This indicates that the opposite scaling of the ablative and radiative stabilization mitigates their effects on the capsule performance and makes the deceleration RTI almost effectively hydro-equivalent.

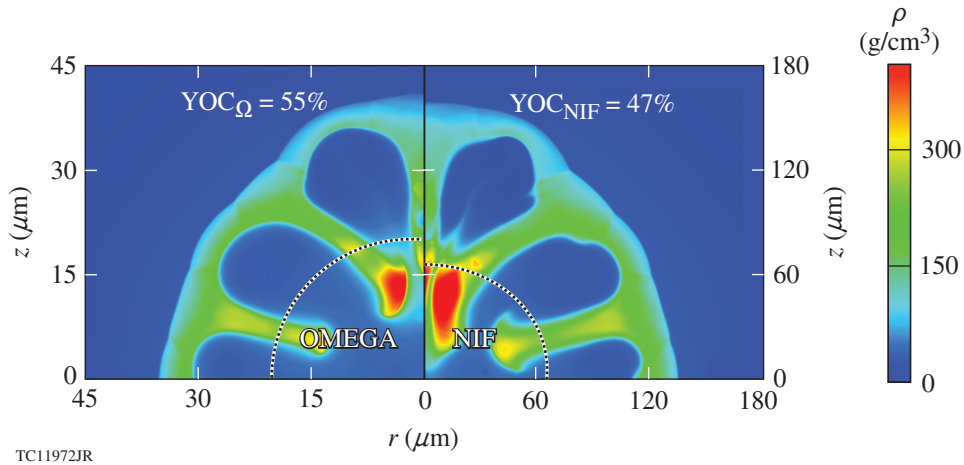
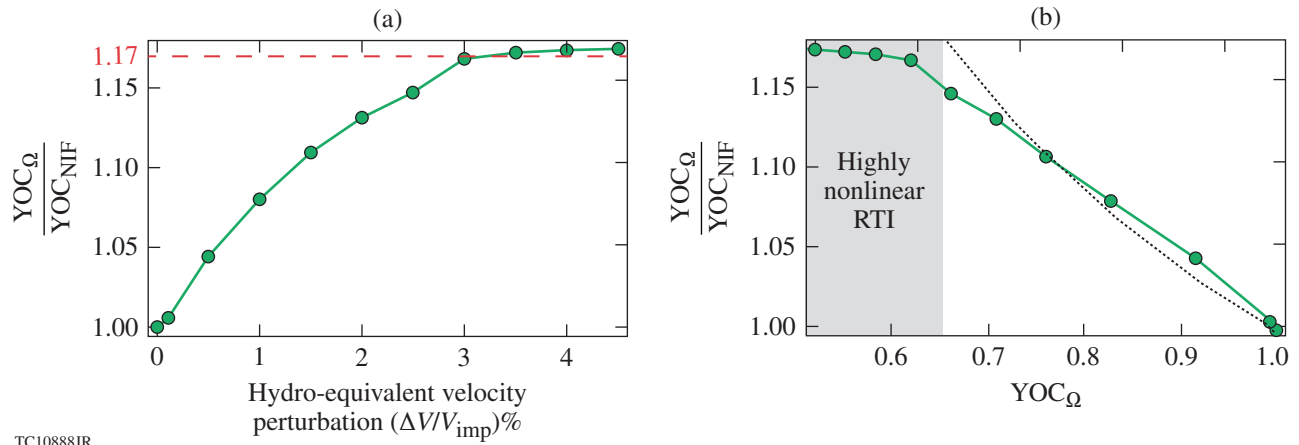


Figure 143.17

Contour plot of the density at bang time, showing nonlinear multimode RTI on NIF and OMEGA scales. The dashed line demarcates the fusion volume (or neutron-averaged volume); the YOC values for this set of hydro-equivalent simulations are indicated.



TC10888JR

Figure 143.18

(a) Results from multimode simulations showing YOC ratio versus velocity perturbation for NIF- and OMEGA-scale implosions asymptote to 1.17 (red dashes). (b) (YOC_{Ω}/YOC_{NIF}) versus YOC_{Ω} from *DEC2D* simulations of the deceleration phase (green solid line/circles) and analytic scaling (black dotted line) matches closely for the linear regime.

The analytic curve [shown in Fig. 143.18(b)] is obtained from Eq. (24) by varying the YOC_{Ω} and using a 35%-higher linear growth factor on the NIF (see **Hydro-Equivalent Scaling of the Yield-Over-Clean**, p. 130); the curve matches well with the multimode simulations in the linear regime and reproduces the YOC ratio of 1.17 obtained from simulations (for a YOC_{Ω} of 0.66, the calculated YOC_{NIF} is 0.56). It is important to note that the formula in Eq. (24) assumes that the yield deterioration is caused by a reduction in the clean volume only; i.e., the hot-spot pressure and temperature are unaltered (compared to 1-D). In the highly nonlinear regime the YOC ratio obtained from simulations deviate from the linear theory [see Fig. 143.18(b)]. This can be attributed to the fact that for such highly nonlinear RTI, the conditions in the burn volume differ from the 1-D predictions because a significant fraction of the shell's kinetic energy is used to drive the instability instead of compressing the hot spot to higher pressures. This effect is being investigated by studying trends in neutron-averaged quantities from deceleration-phase simulations with nonlinear RTI. The scaling of the YOC with the burn average volume will be the subject of a forthcoming publication.

Using the above YOC ratio derived from considering the scaling of the stabilizing effects on the deceleration-phase RTI, the ignition parameter in Eq. (22) is given as $\chi_{\Omega} \approx 0.2$. This is in agreement with the analysis in Ref. 11 and valid within the frame of the 2-D analysis. While 3-D effects on the RTI may lead to a quantitative change of our conclusions, we do not expect any qualitative changes in the scaling results. A similar study in 3-D geometry is the focus of our current research and will be the subject of a forthcoming publication.

Conclusions

A comprehensive study of the scaling of the deceleration-phase RTI has been carried out to assess its impact on the YOC scaling and the hydro-equivalent ignition condition. An analytic model for the hot-spot–ignition condition has been developed, including the emission losses and reabsorption and mass ablation. It is shown that because of the convergence effects, the diffusive terms responsible for ablative stabilization (thermal conduction and radiation transport) do not scale hydro-equivalently with implosion size. Thermal conduction determines the scaling of the ablation velocity V_{abl} during the deceleration phase, and NIF implosions exhibit lower V_{abl} than hydro-equivalent OMEGA implosions. On the other hand, radiation emitted from the hot spot is more effectively reabsorbed by the thicker NIF shell, enhancing the density-gradient scale lengths (L_{min}/R_{hs}) in NIF more than in OMEGA targets. Therefore, mitigation of the deceleration-phase RT instability caused by V_{abl}/V_{imp} and L_{min}/R_{hs} scale oppositely with target size. The linear growth factors on the NIF are 35% higher than on OMEGA. Considering both linear and nonlinear multimode simulations, it has been shown that the deceleration-phase YOC for OMEGA is ~17% higher than the YOC for NIF ignition-scale targets. A no- α Lawson ignition parameter of $\chi_{\Omega} \approx 0.2$ on OMEGA is required to achieve hydro-equivalent ignition for symmetric direct drive on the NIF.

ACKNOWLEDGMENT

The authors thank Dr. K. Anderson, Dr. J. A. Delettrez, and Dr. R. Epstein from the Laboratory of Laser Energetics and Prof. D. Shvarts from Ben-Gurion University of the Negev for many useful discussions. This work has been supported by the U.S. Department of Energy under Cooperative Agreement No. DE-FC02-04ER54789 (Fusion Science Center supported by

the Office of Fusion Energy Sciences) and DE-NA0001944 (National Nuclear Security Administration), the New York State Energy Research Development Authority, and the University of Rochester. The support of DOE does not constitute an endorsement by DOE of the views expressed in this article.

REFERENCES

1. J. Nuckolls *et al.*, *Nature* **239**, 139 (1972).
2. S. E. Bodner, D. G. Colombant, J. H. Gardner, R. H. Lehmborg, S. P. Obenschain, L. Phillips, A. J. Schmitt, J. D. Sethian, R. L. McCrory, W. Seka, C. P. Verdon, J. P. Knauer, B. B. Afeyan, and H. T. Powell, *Phys. Plasmas* **5**, 1901 (1998).
3. J. D. Lindl, *Inertial Confinement Fusion: The Quest for Ignition and Energy Gain Using Indirect Drive* (Springer-Verlag, New York, 1998).
4. R. Kishony and D. Shvarts, *Phys. Plasmas* **8**, 4925 (2001).
5. B. K. Spears, M. J. Edwards, S. Hatchett, J. Kilkenny, J. Knauer, A. Kritcher, J. Lindl, D. Munro, P. Patel, H. F. Robey, and R. P. J. Town, *Phys. Plasmas* **21**, 042702 (2014).
6. A. L. Kritcher *et al.*, *Phys. Plasmas* **21**, 042708 (2014).
7. P. Y. Chang, R. Betti, B. K. Spears, K. S. Anderson, J. Edwards, M. Fatenejad, J. D. Lindl, R. L. McCrory, R. Nora, and D. Shvarts, *Phys. Rev. Lett.* **104**, 135002 (2010).
8. E. I. Moses *et al.*, *Phys. Plasmas* **16**, 041006 (2009).
9. S. Skupsky, J. A. Marozas, R. S. Craxton, R. Betti, T. J. B. Collins, J. A. Delettrez, V. N. Goncharov, P. W. McKenty, P. B. Radha, T. R. Boehly, J. P. Knauer, F. J. Marshall, D. R. Harding, J. D. Kilkenny, D. D. Meyerhofer, T. C. Sangster, and R. L. McCrory, *Phys. Plasmas* **11**, 2763 (2004).
10. T. R. Boehly, D. L. Brown, R. S. Craxton, R. L. Keck, J. P. Knauer, J. H. Kelly, T. J. Kessler, S. A. Kumpan, S. J. Loucks, S. A. Letzring, F. J. Marshall, R. L. McCrory, S. F. B. Morse, W. Seka, J. M. Soures, and C. P. Verdon, *Opt. Commun.* **133**, 495 (1997).
11. R. Nora, R. Betti, K. S. Anderson, A. Shvydky, A. Bose, K. M. Woo, A. R. Christopherson, J. A. Marozas, T. J. B. Collins, P. B. Radha, S. X. Hu, R. Epstein, F. J. Marshall, R. L. McCrory, T. C. Sangster, and D. D. Meyerhofer, *Phys. Plasmas* **21**, 056316 (2014).
12. C. D. Zhou and R. Betti, *Phys. Plasmas* **15**, 102707 (2008).
13. D. Mihalas and B. Weibel-Mihalas, *Foundations of Radiation Hydrodynamics* (Dover Publications, Mineola, NY, 1999).
14. R. Betti, M. Umansky, V. Lobatchev, V. N. Goncharov, and R. L. McCrory, *Phys. Plasmas* **8**, 5257 (2001).
15. R. Betti, K. Anderson, V. N. Goncharov, R. L. McCrory, D. D. Meyerhofer, S. Skupsky, and R. P. J. Town, *Phys. Plasmas* **9**, 2277 (2002).
16. R. Betti and C. Zhou, *Phys. Plasmas* **12**, 110702 (2005).
17. R. Betti, A. R. Christopherson, B. K. Spears, R. Nora, A. Bose, J. Howard, K. M. Woo, M. J. Edwards, and J. Sanz, *Phys. Rev. Lett.* **114**, 255003 (2015).
18. R. Betti, P. Y. Chang, B. K. Spears, K. S. Anderson, J. Edwards, M. Fatenejad, J. D. Lindl, R. L. McCrory, R. Nora, and D. Shvarts, *Phys. Plasmas* **17**, 058102 (2010).
19. H. Takabe *et al.*, *Phys. Fluids* **28**, 3676 (1985).
20. V. Lobatchev and R. Betti, *Phys. Rev. Lett.* **85**, 4522 (2000).
21. C. D. Zhou and R. Betti, *Phys. Plasmas* **14**, 072703 (2007).
22. A. Schiavi and S. Atzeni, *Phys. Plasmas* **14**, 070701 (2007).
23. K. Anderson, R. Betti, and T. A. Gardiner, *Bull. Am. Phys. Soc.* **46**, 280 (2001).
24. A. Bose, P.-Y. Chang, J. R. Davies, and R. Betti, *Bull. Am. Phys. Soc.* **57**, 358 (2012).
25. K. M. Woo, A. Bose, R. Betti, J. A. Delettrez, K. S. Anderson, and R. Epstein, *Bull. Am. Phys. Soc.* **59**, 354 (2014).
26. T. C. Sangster, V. N. Goncharov, R. Betti, T. R. Boehly, D. T. Casey, T. J. B. Collins, R. S. Craxton, J. A. Delettrez, D. H. Edgell, R. Epstein, K. A. Fletcher, J. A. Frenje, V. Yu. Glebov, D. R. Harding, S. X. Hu, I. V. Igumenshchev, J. P. Knauer, S. J. Loucks, C. K. Li, J. A. Marozas, F. J. Marshall, R. L. McCrory, P. W. McKenty, D. D. Meyerhofer, P. M. Nilson, S. P. Padalino, R. D. Petrasso, P. B. Radha, S. P. Regan, F. H. Seguin, W. Seka, R. W. Short, D. Shvarts, S. Skupsky, V. A. Smalyuk, J. M. Soures, C. Stoeckl, W. Theobald, and B. Yaakobi, *Phys. Plasmas* **17**, 056312 (2010).
27. J. Delettrez, R. Epstein, M. C. Richardson, P. A. Jaanimagi, and B. L. Henke, *Phys. Rev. A* **36**, 3926 (1987).
28. R. MacCormack, *J. Spacecr. Rockets* **40**, 757 (2003).
29. E. F. Toro, *Riemann Solvers and Numerical Methods for Fluid Dynamics: A Practical Introduction* (Springer-Verlag, Berlin, 1999).

Shock-Wave Equation-of-State Measurements in Fused Silica up to 1600 GPa

Introduction

Silica is the single most-abundant compound in the earth's mantle and crust and an end member of the MgO-FeO-SiO₂ system that forms those structures.^{1–3} Its behavior at high pressure is fundamental for studies of interest to geophysics, tectonophysics, and the formation of exoplanets.⁴ In both amorphous and crystalline forms, it is a prototype for studying materials at extreme conditions using both static^{5–7} and dynamic^{8–10} compression experiments. The variety of stable polymorphs that exist at ambient pressure makes it possible to cover a wide region of phase space with single-shock techniques. This made it possible to approximate the Grüneisen parameter for solid silica.^{11–13}

Until recently, most high-pressure data for silica were for pressures below 200 GPa, exploring melting and different phase changes in the structure. The development of drivers and techniques at higher pressures has made it possible to study fluid silica produced by TPa shocks using various polymorphs of silica. Understanding material behavior at these extreme conditions is of interest for planetary astrophysics, equation-of-state (EOS) research, and inertial confinement fusion. The principal Hugoniot^{14–16} and release isentrope^{17–19} of α -quartz was measured in the fluid regime (>100 GPa). Research has also been conducted in fused silica,^{16,20–23} stishovite,²¹ and low-density silica foams.^{24–26} This research has enabled one to understand the behavior of materials at the core–mantle boundary on the earth's pressure–temperature conditions where silica would be fluid.²⁷ At higher pressures (>300 GPa), the compressed-silica EOS describes the behavior of material at the core–mantle boundary in super-Earths and other giant exoplanets.²¹ For further increases in pressure along the Hugoniot, silica transitions from a bonded molecular liquid to a dissociated atomic fluid.¹⁶ Alpha-quartz is frequently used as an impedance-matching standard for experiments above 300 GPa (Refs. 17 and 19), allowing one to study other materials at high pressure. These data on fused silica provide added information about silica in this regime.

This article presents results of precision EOS measurements of the fused-silica Hugoniot from 200 to 1600 GPa

using the impedance-matching technique. Previous work measured the fused-silica Hugoniot above the melt curve from 200 to 900 GPa (Refs. 20 and 22). This work extends measurements of the fused-silica Hugoniot well into the dissociated regime and provides lower-pressure data that agree with that of Qi *et al.*²² The latter is significant in that the results of laser-driven experiments using α -quartz as an impedance-matching standard agree well with those from direct-impact measurements using aluminum flyer plates driven by magnetic-field acceleration. Additionally, this agreement increases confidence in the release model recently developed for silica (quartz) as a standard.¹⁹

Method

The Rankine–Hugoniot relations relate the conditions behind a shock discontinuity to those in front of it.²⁸ The relations for conservation of mass and momentum give

$$\frac{\rho_0}{\rho} = 1 - \frac{(u_p)}{U_s}, \quad (1)$$

$$P = \rho_0 U_s u_p, \quad (2)$$

where ρ is the density, ρ_0 is the initial (unshocked) density, u_p is the particle velocity, U_s is the shock velocity, and P is the pressure. If P_0 and ρ_0 are known, measurement of two quantities (typically U_s and u_p) will close these equations and provide an EOS point on the material's Hugoniot.

In this work, the Hugoniot of fused silica was determined by impedance matching (IM) to an α -quartz standard. The IM method relies on the Hugoniot and release curve of a standard to infer the sample's particle velocity from measurements of shock velocity in the standard and the sample. Quartz has recently been established as the preferred standard for EOS experiments because of its transparency at ambient conditions and high shock reflectivity.^{17,19} This technique used the quartz Hugoniot and release curves derived by Knudson and Desjarlais.^{15,19}

These experiments comprise ten older, previously unpublished experiments on the OMEGA laser (shots 55499 to 55508 and 64348)²⁹ and 18 recent experiments using the OMEGA EP laser.³⁰ Both of these frequency-tripled Nd:glass lasers operate at a wavelength of 351 nm. The shock pressures in these experiments were generated using laser pulses ranging from 2- to 6-ns duration, with intensities ranging from ~ 0.2 to 1.7×10^{14} W/cm². The laser spots were all smoothed using distributed phase plates³¹ to achieve shocks with planar regions of either 750 or 1100 μm in diameter.

The targets consisted of 3-mm \times 3-mm flat, *z*-cut, α -quartz baseplates with a nominal thickness of either 50 or 75 μm . A 15- μm -thick layer of parylene (CH) was deposited on the front of the target as a low-*Z* ablator that enhanced the ablation pressure and reduced the production of hard x rays. The laser plasmas produced in this case had temperatures of ~ 2 keV (Ref. 32) such that the attenuation length of x rays in the quartz was < 5 μm (Ref. 33). This limits the preheating of the quartz baseplate to regions far from the point where IM is performed. Fused-silica and α -quartz samples were glued, adjacent to each other, to the back of the baseplate. These were affixed to the baseplate using an ultralow viscosity, UV-cured epoxy that produced glue layers < 3 μm thick. A sketch of the target assembly is shown in Fig. 143.19(a). The fused-silica and quartz samples had initial densities of 2.20 g/cm³ and 2.65 g/cm³, respectively. The refractive indices at 532 nm were 1.461 for the fused silica and 1.547 for the quartz.

Shock velocities were measured using a line-imaging velocity interferometer system for any reflector (VISAR)^{34–37} that

measures the phase change caused by Doppler-shifted light reflecting off a moving surface. At pressures above 150 GPa, both the fused silica and quartz melt and form reflective shock fronts.¹⁶ The materials are both initially transparent so VISAR measures the velocity of the shock front within the material. Antireflective coatings were applied to the back surface of both samples to eliminate ghost reflections from that surface. To resolve 2π ambiguities, two VISAR's with different velocity sensitivities were used. These sensitivities were 3.194 km/s/fringe and 4.375 km/s/fringe for the quartz and 3.389 km/s/fringe and 4.642 km/s/fringe for the fused silica. The VISAR images provided phase shifts resulting from changes in velocity that were analyzed using the Fourier transform method.³⁷ The error in determining the phase was estimated as $\sim 3\%$ of a fringe, resulting in velocity measurements with $< 1\%$ precision because of multiple fringe jumps produced by the shock. The VISAR system used a frequency-doubled Nd:YAG laser operating at 532 nm, and the two streak cameras used 9- and 15-ns sweep durations. Figures 143.19(b) and 143.19(c) provide an example of the raw data and the extracted velocity profile.

The experimental observables were the shock velocity in the quartz and fused-silica samples at the point at which the shock transited the quartz-fused silica interface. The shock velocities in the quartz and fused silica were measured immediately before and after the interface, respectively. The quartz witness (adjacent to the fused-silica sample) monitored the velocity across the glue layer and the planarity of the shock. The initial shock velocity in the fused silica was fit over 300 ps and linearly extrapolated back to the quartz/glue interface to

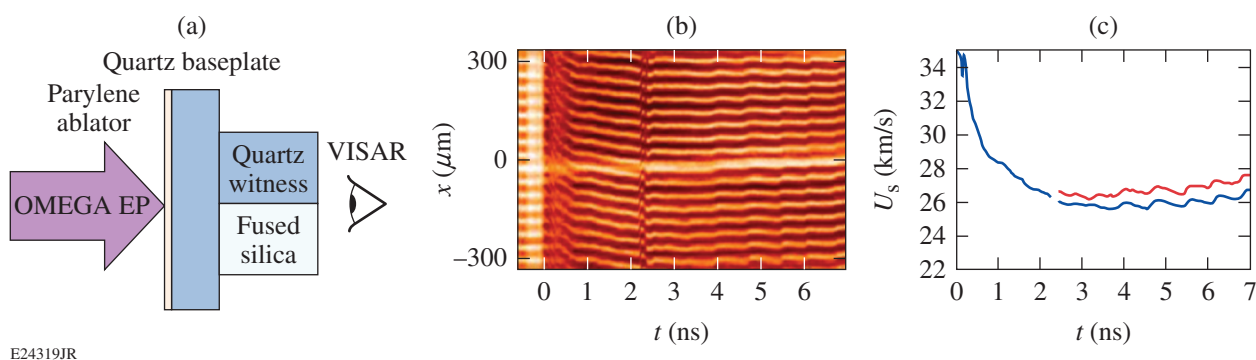


Figure 143.19

(a) Target schematic. (b) Raw VISAR data for shot 17862. Target orientation is the same as in (a). (c) Extracted velocity for shot 17862 showing quartz (blue) and fused silica (red). VISAR: velocity interferometer system for any reflector.

determine the velocity at the location of the interface, assuming no glue layer existed.³⁸

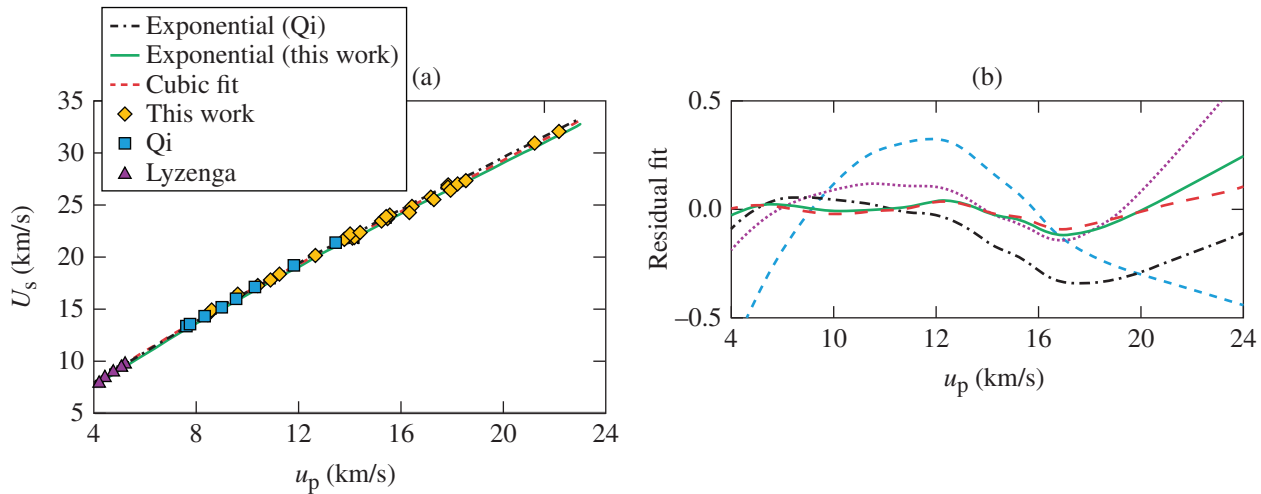
Errors were calculated using the Monte Carlo method, which generates normally distributed random variables based on the mean and standard deviation of an observed quantity. For these shock velocities, this resulted in an observation error <1% from VISAR. The initial density was assumed to have negligible error, and the errors in the quartz Hugoniot and release curve were determined from the covariance matrices for the cubic Hugoniot and effective Grüneisen parameter from Ref. 19.

Results/Discussion

A total of 28 impedance-matching points were used to determine the Hugoniot of fused silica; they ranged in pressure from 260 GPa up to 1570 GPa. The results are given in Table 143.I. The shock speed's dependence on particle velocity (U_s-u_p curve), shown in Fig. 143.20(a), was fit to a cubic polynomial (red dashed line), and the exponential form $U_s = a + bu_p - cu_p e^{-du_p}$ (green line). These are shown as well as the exponential fit from Qi *et al.*²² (black dashed-dotted line). The error bars on the data are smaller than the points in the graph. The cubic and exponential fits were made using

Table 143.I: Shock parameters for fused-silica determined from impedance matching to quartz standard.

Shot	U_s^Q (km/s)	U_s^{FS} (km/s)	u_p^{FS} (km/s)	P^{FS} (GPa)	ρ^{FS} (g/cm ³)
55499	21.58±0.05	21.83±0.06	13.85±0.05	665.5±2.8	6.02±0.05
55500	26.33±0.05	26.92±0.06	17.85±0.06	1057.8±3.7	6.53±0.05
55501	30.18±0.05	30.88±0.06	21.21±0.08	1441.4±6.0	7.03±0.07
55502	31.32±0.05	32.11±0.06	22.19±0.10	1568.6±7.6	7.13±0.08
55503	27.00±0.05	27.30±0.06	18.50±0.06	1111.5±3.8	6.83±0.06
55505	23.51±0.05	24.02±0.06	15.57±0.06	823.1±3.2	6.26±0.05
55506	18.27±0.05	18.37±0.06	11.24±0.05	454.3±2.2	5.67±0.05
55507	17.25±0.05	17.26±0.06	10.39±0.05	394.7±2.1	5.53±0.05
55508	14.43±0.14	14.44±0.06	8.40±0.13	267.1±4.1	5.26±0.12
64348	21.81±0.10	22.16±.017	14.02±0.11	683.8±6.2	5.99±0.13
18752	23.23±0.10	23.51±0.13	15.22±0.11	787.5±6.2	6.24±0.11
18754	21.48±0.10	21.59±0.10	13.79±0.10	655.4±5.3	6.09±0.10
18755	24.60±0.10	24.89±0.10	16.41±0.11	899.2±6.3	6.46±0.10
18757	22.18±0.10	22.33±0.17	14.37±0.11	706.5±6.3	6.18±0.14
18758	25.43±0.10	25.72±0.10	17.13±0.11	969.9±6.6	6.59±0.11
18760	26.24±0.10	26.62±0.10	17.82±0.11	1043.9±6.9	6.66±0.11
18761	23.47±0.10	23.54±0.14	15.49±0.11	802.6±6.4	6.44±0.13
18762	26.34±0.10	26.49±0.10	17.95±0.11	1046.7±7.0	6.83±0.11
18763	24.39±0.10	24.32±0.10	16.31±0.11	872.9±6.2	6.68±0.11
18764	26.74±0.12	27.12±0.10	18.25±0.13	1089.5±8.4	6.73±0.12
18765	25.52±0.10	25.58±0.18	17.26±0.12	971.7±7.8	6.77±0.16
18766	23.48±0.10	23.85±0.10	15.43±0.11	810.2±6.0	6.24±0.10
19485	14.89±0.13	14.80±0.22	8.60±0.13	280.3±4.9	5.26±0.17
19492	17.87±0.14	17.71±0.15	10.90±0.14	424.8±5.9	5.72±0.15
19494	20.08±0.10	20.18±0.14	12.63±0.11	561.1±5.3	5.88±0.12
19498	21.82±0.17	21.65±0.19	14.14±0.18	673.6±9.3	6.34±0.20
19500	21.84±0.10	21.72±0.10	14.14±0.11	676.0±5.4	6.31±0.11
19503	16.24±0.10	16.34±0.10	9.58±0.10	344.7±3.7	5.32±0.10



E24320JR

Figure 143.20

(a) U_s - u_p plot for fused silica. Experimental results from this work (yellow diamonds), Qi *et al.*¹⁹ (blue squares), and Lyzenga *et al.*⁷ (purple triangles) are shown. The exponential fit from Qi *et al.* (black dashed-dotted line) and cubic (red dashed line) and exponential (solid green line) fits from this work are also displayed. The error bars on the data are smaller than the points in the graph. (b) Fits to residual of U_s - u_p relations using a low-order smoothing spline. Cubic (red dashed line) and exponential (green solid line) fits from this work agree with the data. Linear (blue dashed line) and quadratic (purple dotted line) demonstrate systematic error in the fit, and exponential fit from Qi *et al.* (black dashed-dotted line) diverges from experimental results for $u_p > 12$ km/s ($P > \sim 500$ GPa).

weighted nonlinear-least-squares methods to the data in this article and that from both Qi *et al.*¹⁹ and Lyzenga *et al.*⁷ The coefficients and covariance matrix for the cubic fit are given in Tables 143.II and 143.III. Similarly, the parameters for the exponential model are given in Tables 143.IV and 143.V.

Table 143.II: Fit parameters for the cubic U_s - u_p relation of the form $U_s = a_0 + a_1 u_p + a_2 u_p^2 + a_3 u_p^3$.

a_0 (km/s)	a_1	a_2 (km/s) ⁻¹	a_3 (km/s) ⁻²
0.635	1.937	-4.102×10^{-2}	7.925×10^{-4}

The residuals for each of these fits were computed and, for clarity, a low-order spline was fit to each set of residuals and displayed in Fig 143.20(b). Linear (blue dashed line) and quadratic (purple dotted line) fits are also shown for contrast. These residual plots show that the cubic fit and our new exponential fits replicate residual data to similar precision. Importantly, the exponential fit given by Qi *et al.* does not fit these data well, predicting stiffer behavior at higher pressures. This is shown in

the P - ρ Hugoniot data in Fig. 143.21. It should be noted that the Qi fit is based on their molecular dynamics simulations, which agreed with their data up to ~ 630 GPa (the highest pressure reached in their experiments). The simulations were performed for pressures from 86 to 1500 GPa and those simulation results were the basis for their exponential fit.

Note that both our data and the fits (cubic and exponential) to our data agree very well with the data from Qi *et al.* It is the extrapolation of the first-principles molecular dynamics (FPMD)-based exponential fit of Qi *et al.* that is inconsistent with the data presented here. This can be seen in the residuals in Fig. 143.20(b), where the Qi model (black dashed-dotted line) deviates from the data at $u_p > \sim 12$ (km/s). Below that velocity the models and data agree well. That velocity corresponds to ~ 600 GPa, which is approximately the pressure determined by Hicks *et al.* for the transition from a bonded liquid to an atomic fluid along the Hugoniot of fused silica.¹⁶ This implies that the compressibility of the bonded liquid differs from that of the atomic fluid, with the dissociated atomic fluid being more compressible.

Table 143.III: Covariance matrix elements for the cubic U_s - u_p relation given in Table 143.II.

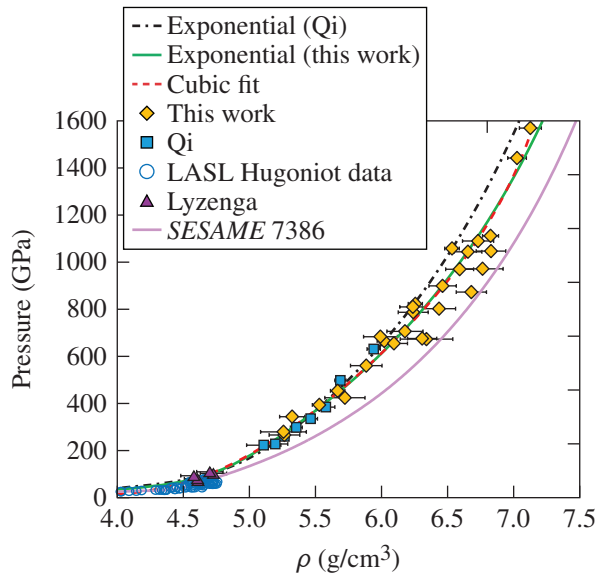
$\sigma_{a_0}^2$ ($\times 10^{-1}$)	$\sigma_{a_0} \sigma_{a_1}$ ($\times 10^{-2}$)	$\sigma_{a_0} \sigma_{a_2}$ ($\times 10^{-3}$)	$\sigma_{a_0} \sigma_{a_3}$ ($\times 10^{-4}$)	$\sigma_{a_1}^2$ ($\times 10^{-3}$)	$\sigma_{a_1} \sigma_{a_2}$ ($\times 10^{-4}$)	$\sigma_{a_1} \sigma_{a_3}$ ($\times 10^{-5}$)	$\sigma_{a_2}^2$ ($\times 10^{-5}$)	$\sigma_{a_2} \sigma_{a_3}$ ($\times 10^{-6}$)	$\sigma_{a_3}^2$ ($\times 10^{-8}$)
1.118	-3.019	2.419	-5.930	8.568	-7.094	1.781	6.033	-1.547	4.041

Table 143. IV: Fit parameters for the exponential U_s-u_p relation of the form $U_s = a + bu_p - cu_p e^{-du_p}$.

a (km/s)	b	c	d (km/s) $^{-1}$
4.972	1.218	2.432	0.396

Table 143.V: Covariance matrix elements for the exponential U_s-u_p relation given in Table 143.IV.

σ_a^2 ($\times 10^{-1}$)	$\sigma_a \sigma_b$ ($\times 10^{-2}$)	$\sigma_a \sigma_c$ ($\times 10^{-2}$)	$\sigma_a \sigma_d$ ($\times 10^{-2}$)	σ_b^2 ($\times 10^{-4}$)	$\sigma_b \sigma_c$ ($\times 10^{-3}$)	$\sigma_b \sigma_d$ ($\times 10^{-3}$)	σ_c^2 ($\times 10^{-1}$)	$\sigma_c \sigma_d$ ($\times 10^{-2}$)	σ_d^2 ($\times 10^{-3}$)
1.900	-1.005	-4.749	-2.101	5.386	2.116	1.075	1.004	1.149	2.809



E24321JR

Figure 143.21

P - ρ Hugoniot curve. The exponential fit from Qi *et al.*¹⁹ clearly lies above the data and fits computed using this work and data from Qi *et al.* and Lyzenga *et al.*⁷ This implies that the fit by Qi is less compressible than the experimental data. Exponential fit and cubic fit from this work are indistinguishable for pressures <1400 GPa. Above 1400 GPa, the cubic fit begins to diverge and is not valid for extrapolation to pressures >1600 GPa. All data use the same labels as Fig. 143.20(a). Los Alamos Scientific Laboratory shock Hugoniot data (open blue circles) and the SESAME 7386 table (magenta line) are included for completeness.

Conclusion

The Hugoniot of fused silica shocked to the fluid state was measured by impedance matching to α -quartz for pressures up to 1600 GPa. The results from these laser-driven experiments are in good agreement over the range of 200 to 600 GPa with results using magnetically driven aluminum flyer plates, a significant departure from past experience comparing the two drive platforms. The results extend the measurements for the fused-

silica Hugoniot well into the region where silica is expected to dissociate into an atomic fluid. This may explain why recent FPMD predictions by Qi *et al.*²² underpredict the compressibility of silica at the higher pressures. Using this data and that of Qi and Lyzenga, a new U_s-u_p curve was generated for the range of 200 to 1600 GPa. The cubic polynomial presented in Table 143.II and a fit using the form $U_s = a + bu_p - cu_p e^{-du_p}$ given in Table 143.IV were found to model the data equally well. The significant curvature in the cubic model is undesirable for extrapolation to pressures above 1600 GPa. Therefore, the exponential model is preferred for extrapolation since at higher pressures it asymptotes to a linear U_s-u_p relationship.

ACKNOWLEDGMENT

This material is based upon work supported by the Department of Energy National Nuclear Security Administration under Award Number DE-NA0001944, the University of Rochester, and the New York State Energy Research and Development Authority. The support of DOE does not constitute an endorsement by DOE of the views expressed in this article.

REFERENCES

1. J. W. Morgan and E. Anders, Proc. Natl. Acad. Sci. **77**, 6973 (1980).
2. S. K. Saxena, Geochim. Cosmochim. Acta **60**, 2379 (1996).
3. Y. Fei, H.-K. Mao, and B. O. Mysen, J. Geophys. Res. **96**, 2157 (1991).
4. R. J. Hemley, C. T. Prewitt, and K. J. Kingma, Rev. Mineral. Geochem. **29**, 41 (1994).
5. L. S. Dubrovinsky *et al.*, Nature **388**, 362 (1997).
6. D. Andrault *et al.*, Science **282**, 720 (1998).
7. Q. Williams and R. Jeanloz, Science **239**, 902 (1988).
8. J. Wackerle, J. Appl. Phys. **33**, 922 (1962).
9. R. G. McQueen, J. N. Fritz, and S. P. Marsh, J. Geophys. Res. **68**, 2319 (1963).

10. G. A. Lyzenga, T. J. Ahrens, and A. C. Mitchell, *J. Geophys. Res. B* **88**, 2431 (1983).
11. S.-N. Luo *et al.*, *Phys.-Usp.* **45**, 435 (2002).
12. S.-N. Luo *et al.*, *Geophys. Res. Lett.* **29**, 36 (2002).
13. J. A. Akins and T. J. Ahrens, *Geophys. Res. Lett.* **29**, 31 (2002).
14. D. G. Hicks, T. R. Boehly, P. M. Celliers, J. H. Eggert, E. Vianello, D. D. Meyerhofer, and G. W. Collins, *Phys. Plasmas* **12**, 082702 (2005).
15. M. D. Knudson and M. P. Desjarlais, *Phys. Rev. Lett.* **103**, 225501 (2009).
16. D. G. Hicks, T. R. Boehly, J. H. Eggert, J. E. Miller, P. M. Celliers, and G. W. Collins, *Phys. Rev. Lett.* **97**, 025502 (2006).
17. T. R. Boehly, J. E. Miller, D. D. Meyerhofer, J. G. Eggert, P. M. Celliers, D. G. Hicks, and G. W. Collins, in *Shock Compression of Conducted Matter—2007*, edited by M. Elert, M. D. Furnish, R. Chau, N. Holmes, and J. Nguyen (American Institute of Physics, Melville, NY, 2007), Vol. 955, pp. 19–22.
18. S. Brygoo, D. G. Hicks, P. Loubeyre, J. H. Eggert, S. McWilliams, P. M. Celliers, T. R. Boehly, R. Jeanloz, and G. W. Collins, “Development of Melted Quartz as an Impedance-Matching Standard for Strong Laser Shock Measurements (unpublished).”
19. M. D. Knudson and M. P. Desjarlais, *Phys. Rev. B* **88**, 184107 (2013).
20. S. Brygoo *et al.*, *Nature Materials* **6**, 274 (2007).
21. M. Millot *et al.*, *Science* **347**, 418 (2015).
22. T. Qi *et al.*, *Phys. Plasmas* **22**, 062706 (2015).
23. R. G. Kraus *et al.*, *J. Geophys. Res., E, Planets* **117**, E09009 (2012).
24. J. E. Miller, “High-Pressure Equation-of-State of Porous-Ta₂O₅,” Ph.D. thesis, University of Rochester, 2007.
25. M. D. Knudson and R. W. Lemke, *J. Appl. Phys.* **114**, 053510 (2013).
26. K. Falk, C. A. McCoy, C. L. Fryer, C. W. Greeff, A. L. Hungerford, D. S. Montgomery, D. W. Schmidt, D. G. Sheppard, J. R. Williams, T. R. Boehly, and J. F. Benage, *Phys. Rev. E* **90**, 033107 (2014).
27. T. Lay, Q. Williams, and E. J. Garnero, *Nature* **392**, 461 (1998).
28. M. B. Boslough and J. R. Asay, in *High-Pressure Shock Compression of Solids*, edited by J. R. Asay and M. Shahinpoor, High-Pressure Shock Compression of Condensed Matter (Springer, New York, 1993), pp. 7–42.
29. T. R. Boehly, Laboratory for Laser Energetics, private communication (2014).
30. L. J. Waxer, D. N. Maywar, J. H. Kelly, T. J. Kessler, B. E. Kruschwitz, S. J. Loucks, R. L. McCrory, D. D. Meyerhofer, S. F. B. Morse, C. Stoeckl, and J. D. Zuegel, *Opt. Photonics News* **16**, 30 (2005).
31. Y. Lin, T. J. Kessler, and G. N. Lawrence, *Opt. Lett.* **20**, 764 (1995).
32. M. A. Barrios, D. G. Hicks, T. R. Boehly, D. E. Fratanduono, J. H. Eggert, P. M. Celliers, G. W. Collins, and D. D. Meyerhofer, *Phys. Plasmas* **17**, 056307 (2010).
33. B. L. Henke, E. M. Gullikson, and J. C. Davis, *At. Data Nucl. Data Tables* **54**, 181 (1993).
34. L. M. Barker and R. E. Hollenbach, *J. Appl. Phys.* **43**, 4669 (1972).
35. L. M. Barker and K. W. Schuler, *J. Appl. Phys.* **45**, 3692 (1974).
36. P. M. Celliers *et al.*, *Appl. Phys. Lett.* **73**, 1320 (1998).
37. P. M. Celliers, D. K. Bradley, G. W. Collins, D. G. Hicks, T. R. Boehly, and W. J. Armstrong, *Rev. Sci. Instrum.* **75**, 4916 (2004).
38. M. A. Barrios, T. R. Boehly, D. G. Hicks, D. E. Fratanduono, J. H. Eggert, G. W. Collins, and D. D. Meyerhofer, *J. Appl. Phys.* **111**, 093515 (2012).

Temporal-Contrast Measurements of a White-Light-Seeded Noncollinear Optical Parametric Amplifier

Introduction

Ultra-intense laser systems being developed will use the full potential of deuterated potassium dihydrogen phosphate (DKDP) for high-energy optical parametric chirped-pulse amplification (OPCPA).^{1,2} Noncollinear pumping of DKDP produces broadband gain for supporting pulses as short as 10 fs. Large-aperture DKDP crystals (>400 mm) make it possible to use Nd:glass lasers as kilojoule pump sources.³ The front ends for these systems must provide broadband pulses centered around 910 nm to match the gain of DKDP when pumped at 527 nm at the optimum noncollinear angle.³ Their output must be compressible and focusable to maximize the on-target intensity, and the temporal prepulse contrast must be extremely high to avoid perturbing the target before the interaction with the main pulse.

This article presents our temporal contrast measurements of a prototype front end that were first presented in 2011 (Ref. 4) and have been further analyzed and described in more detail. The front end produces microjoule pulses with 210 nm of bandwidth (full width at 10%) centered at 910 nm. Previous front-end demonstrations used the idler from the first amplifier stage to seed subsequent amplifiers in either a chirped collinear geometry¹ or angularly dispersed geometry.² Here an alternate approach is evaluated, based on the generation of white-light continuum (WLC) in a sapphire plate.⁴ This approach simplifies the requirements for the seed oscillator and pump lasers and removes the need to precisely set the spectral chirp of the pump¹ or eliminate the angular dispersion of the idler.² Although WLC-seeded noncollinear optical parametric amplifiers (NOPA's) have been used for over a decade as tunable sources of femtosecond pulses,⁴⁻⁷ their prepulse contrast has not been measured using cross-correlators with sufficient bandwidth and dynamic range. In this work, a NOPA-based cross-correlator has been developed⁸ for this purpose with a dynamic range, bandwidth, and resolution of 120 dB, 150 nm, and 250 fs, respectively. Measurements over a 350-ps window show that the uncompressed output of a WLC-seeded NOPA has a prepulse contrast that exceeds the 120-dB dynamic range of the cross-correlator up to -5 ps before the main peak.

Experimental Setup and Results

The front end shown in Fig. 143.22 is similar to previously reported systems.⁹⁻¹¹ Oscillator pulses were stretched to seed a Yb-doped-fiber chirped-pulse-amplification (CPA) system to produce 250-fs, 11- μ J, 1046-nm pulses at 500 kHz. A portion (1.6 μ J) was weakly focused into a 4-mm sapphire plate

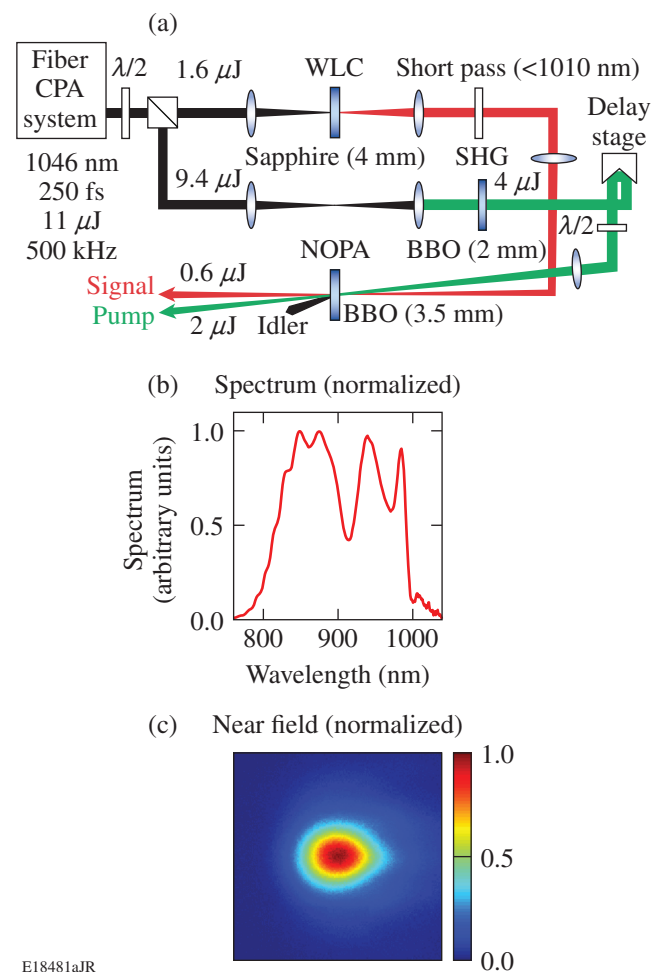


Figure 143.22 (a) Experimental setup; (b) NOPA spectrum; (c) NOPA near-field fluence (normalized), imaged at the BBO crystal. BBO: beta-barium borate; CPA: chirped-pulse amplification; NOPA: noncollinear optical parametric amplifier; SHG: second-harmonic generation; WLC: white-light continuum.

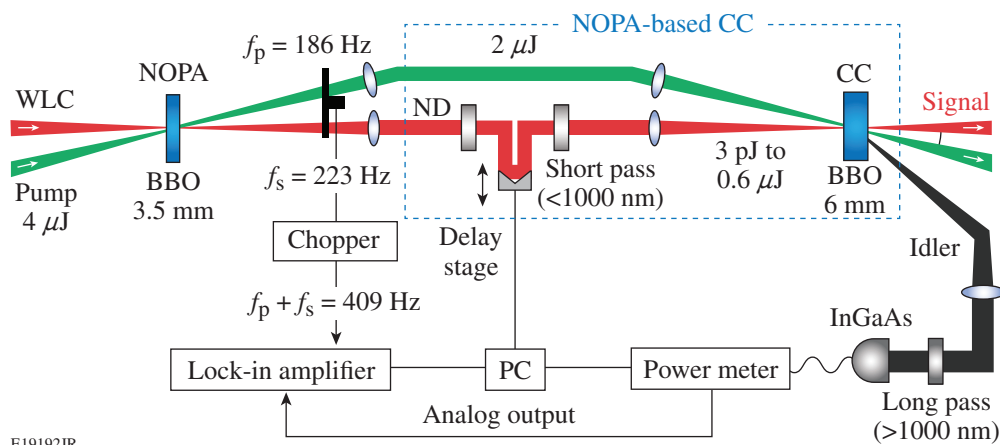
to generate the WLC seed.⁴ The remainder was frequency doubled, producing 4 μJ for pumping the NOPA, which was a 3.5-mm-thick beta-barium borate (BBO) crystal cut at 21.6°. The NOPA's spectrum and beam profile are shown in Fig. 143.22. The spectrum full width at half maximum (FWHM) was 175 nm (full width at 10% = 210 nm) and the pulse energy was 600 nJ [1.3%-rms (root mean square) pulse to pulse]. The internal noncollinear angle in the BBO crystal was set to 2.3° to maximize the bandwidth and minimize spatiotemporal aberrations induced by the angular-dependent gain of the NOPA.¹¹ The chirp of the WLC and NOPA ($\sim 1300 \text{ fs}^2$) was removed using a standard fused-silica prism compressor to produce 13-fs pulses ($1.07\times$ the Fourier transform limit).

A cross-correlator (CC) based on the NOPA process⁸ was developed to measure the temporal contrast of the uncompressed pulses directly from the NOPA (see Fig. 143.23). The residual NOPA pump pulses (2 μJ , 523 nm, 250 fs) provide the temporal gate by pumping a second, thicker BBO crystal (6 mm, 27.1°) aligned noncollinearly for maximum bandwidth. Although this pump beam has been partially depleted by the signal in the NOPA ($\sim 50\%$) and will therefore have a non-Gaussian beam profile, this scheme allows for the maximum available pump pulse energy to be used in both the NOPA and CC, maximizing the gain and dynamic range, which would be significantly reduced if the available power were split between the two crystals. The part of the pulse under test (signal) that temporally overlaps the pump is amplified, producing a non-degenerate idler pulse centered at 1250 nm. The signal pulse was sampled over a 350-ps range by varying the delay between the pump and signal and measuring the idler with an InGaAs power meter (Agilent 81624B). One feature of NOPA-based

CC's is that they provide broadband gain and serve as a pre-amplifier for the detection system. When optimally configured, the unsaturated gain is 39 dB with a bandwidth of 150 nm.

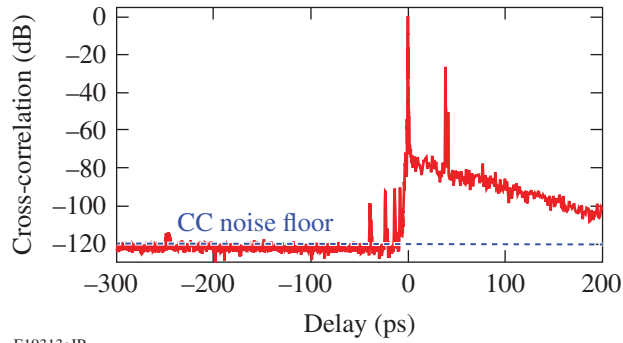
Several techniques were used to minimize noise that would otherwise limit the dynamic range of the CC. Since the signal and idler are non-degenerate, background noise from signal scattering in the CC crystal is reduced by placing a long-pass filter (Schott RG1000, 7 mm thick) before the power meter. Further rejection of scattering and parametric fluorescence from the CC is obtained using a lock-in detection technique as previously demonstrated for second-order autocorrelators.^{12,13} The pump and signal beams are chopped at 186 and 223 Hz, respectively, and the idler component at the sum frequency (409 Hz) from the analog output of the InGaAs power meter is measured using a lock-in amplifier. As a result of the spectral filtering and lock-in detection, all of the available pump and signal energy can be used without saturating the detection system when sampling a low-intensity temporal region of the pulse under test. Calibrated neutral-density filters are inserted in the signal path when sampling the main peak to ensure that the pump pulse is not depleted and, therefore, that the idler power is proportional to the attenuated signal intensity. The CC dynamic range of 120 dB results from the combination of the neutral-density filters (60 dB), the adjustable gain of the InGaAs power meter (40 dB), and the dynamic range of the lock-in detection scheme (20 dB).

A cross-correlation measurement of the uncompressed NOPA pulse is shown in Fig. 143.24. The CC noise floor was determined to be 120 dB below the peak by blocking either the pulse under test or the CC pump. Apart from several discrete



E19192JR

Figure 143.23
Schematic for the NOPA and NOPA-based cross-correlator (CC). PC: personal computer.



E19313aJR

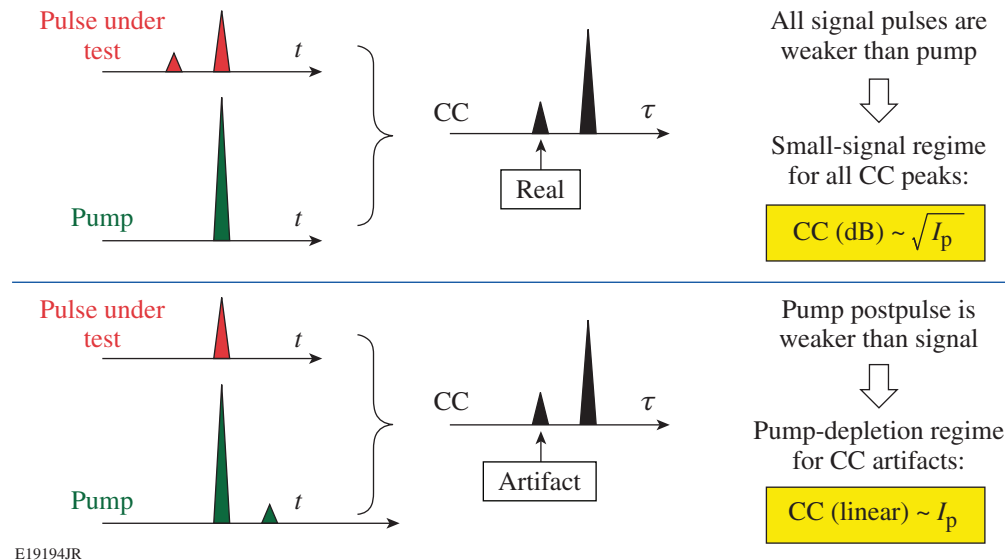
Figure 143.24
Cross-correlation scan.

peaks, the prepulse contrast up to 5 ps before the main peak exceeds the 120-dB CC dynamic range. Note that the width of the uncompressed pulse (~ 300 fs) has not been deconvolved from these measurements. Therefore, if the peak intensity increase from compressing the pulse from 300 fs to 13 fs is ~ 13 dB, the compressed pulse contrast exceeds 133 dB.

Determining whether discrete peaks are real prepulses or artifacts caused by gate or pump postpulses is a problem common to all cross-correlators. For a NOPA-based device, however, the main pump pulse provides much more gain for the signal than is provided by lower-intensity pump noise. (The necessary by-product of gain, a parametric fluorescence background, is mitigated using the two-frequency lock-in

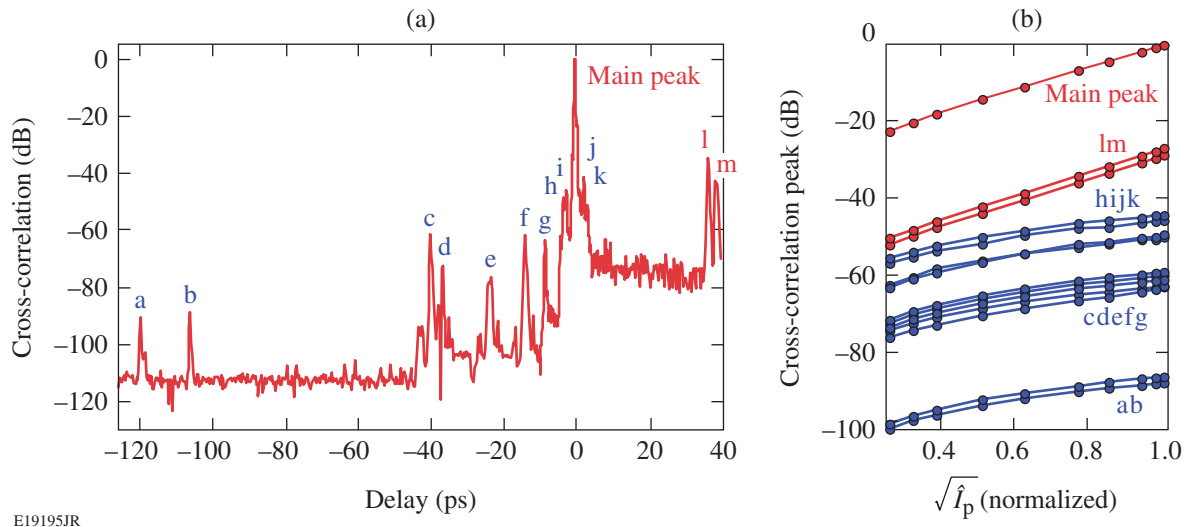
technique.) Moreover, the nature of each peak (whether it is an actual prepulse on the signal-under-test or a measurement artifact created by a postpulse on the pump) can be determined from its scaling with the intensity of the pump (shown schematically in Fig. 143.25). A prepulse on the signal that overlaps with the main pump pulse experiences the maximum small-signal gain; therefore, the CC peak scales exponentially with the pump field.¹⁴ In terms of the pump intensity I_p , the small-signal scaling on a logarithmic scale is $CC(\text{dB}) \sim \sqrt{I_p}$. Alternatively, when a weak pump postpulse overlaps with the main signal peak, the CC gain is much lower. In this “small-pump” limit, the CC peak scales linearly with I_p ; therefore, on a logarithmic plot, $CC(\text{dB}) \sim \log_{10}(I_p)$.

Measurements of the discrete peaks are shown in Fig. 143.26. To emphasize any artifacts, the maximum peak gain of the CC was reduced from 39 to 17 dB by halving the thickness of the CC crystal and increasing the pump spot size. The magnitude of each peak was measured as the pump polarization was rotated using a half-wave plate to vary the amplitude of the phase-matched component of the pump along the crystal axis. The normalized intensity of the pump in terms of the half-wave-plate angle is $\hat{I}_p = \cos^2(2\theta)$. Figure 143.26 shows that all peaks before the main peak scale following the small-pump scaling, $CC(\text{dB}) \sim \log_{10}(\hat{I}_p)$, and are, therefore, artifacts from pump postpulses. Therefore, the prepulse contrast for the uncompressed pulses does not exceed 120 dB.



E19194JR

Figure 143.25
Schematic showing the different intensity scalings to determine whether a cross-correlation peak is caused by a true prepulse before the pulse under test or is an artifact caused by the CC pump postpulse.

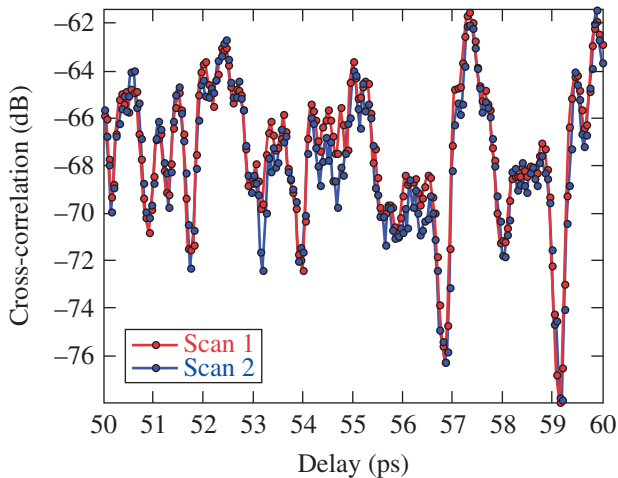


E19195JR

Figure 143.26

(a) Cross-correlation scan taken at reduced CC gain (17 dB) to emphasize artifacts from pump postpulses. (b) Magnitude of each peak for varying normalized pump field ($\sqrt{\hat{I}_p}$). The red curves correspond to the main pulse under test and crystal reflections; the blue curves correspond to artifacts produced by CC pump postpulses.

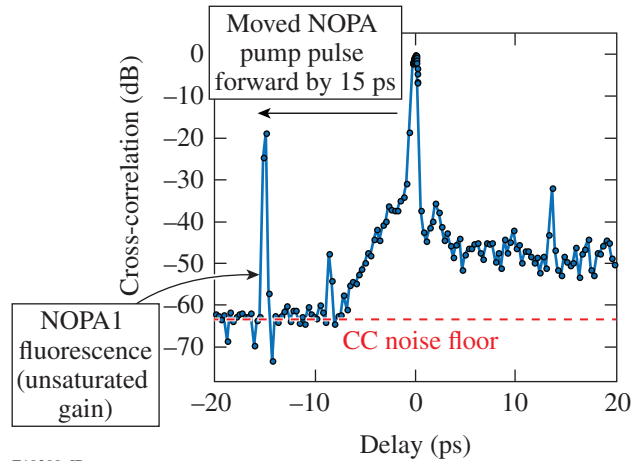
One unexpected feature of the CC measurements is the exponential tail following the main CC peak. The tail has a time constant of 29 ps, an intensity contrast greater than 80 dB, and an energy contrast of 56 dB. It was found that the temporal modulation was repeatable from scan to scan (as shown in Fig. 143.27) and, therefore, is not random noise. Furthermore, very similar scans were measured at a later time when the crystal used to generate the WLC was changed from sapphire to undoped yttrium aluminum garnet. Lastly, Fig. 143.28 shows



E19199JR

Figure 143.27

Section of the postpulse tail, showing the repeatability from scan to scan.



E19200aJR

Figure 143.28

Cross-correlation scan when the NOPA pump pulse was temporally shifted 15 ps before the seed pulse. This shows that a tail is present when there is no gain in the NOPA.

measurements of the unamplified WLC, where the NOPA pump was temporally shifted 15 ps before the seed. These measurements suggest that the tail is not caused by gain in the NOPA. Unfortunately, the dynamic range for the reduced signal level was not sufficiently high (~ 63 dB) to determine whether the tail was also present with the pulse of fluorescence created by the pump pulse. Therefore, it has not been determined if the tail is a result of the WLC process or if it is caused by the CC

optics. Nonetheless, there are typically additional picosecond-pumped NOPA stages before the stretcher, with at least 50 dB of gain, that would suppress the tail to an insignificant level.¹⁵ Furthermore, the temporal contrast after the main pulse is an issue in a CPA system only when self-phase modulations during the amplification of the chirped pulses leads to weaker satellite prepulses.¹⁶

Conclusions

This article reports the first broadband, high-dynamic-range, temporal contrast measurements of a WLC-seeded NOPA. The NOPA-based cross-correlator that was developed for this purpose has a dynamic range, bandwidth, and resolution of 120 dB, 150 nm, and 250 fs, respectively. A simple technique for distinguishing between real prepulses and pump artifacts for any cross-correlator based on parametric amplification has been demonstrated. Measurements over a 350-ps window show that the uncompressed output of the WLC-seeded NOPA has a prepulse contrast that exceeds the 120-dB dynamic range of the cross-correlator up to 5 ps before the main peak. These results, combined with a previous analysis of the WLC-seeded NOPA,¹¹ supports its potential as a front end for ultra-intense OPCPA systems.

ACKNOWLEDGMENT

This material is based upon work supported by the Department of Energy National Nuclear Security Administration under Award Number DE-NA0001944, the University of Rochester, and the New York State Energy Research and Development Authority. The support of DOE does not constitute an endorsement by DOE of the views expressed in this article.

REFERENCES

1. Y. Tang *et al.*, *Opt. Lett.* **33**, 2386 (2008).
2. V. V. Lozhkarev *et al.*, *Opt. Express* **14**, 446 (2006).
3. V. V. Lozhkarev *et al.*, *Laser Phys.* **15**, 1319 (2005).
4. J. Bromage, C. Dorrer, and J. D. Zuegel, in *Advances in Optical Materials*, OSA Technical Digest (CD) (Optical Society of America, Washington, DC, 2011), Paper JWC2.
5. M. K. Reed *et al.*, *J. Opt. Soc. Am. B* **12**, 2229 (1995).
6. T. Wilhelm, J. Piel, and E. Riedle, *Opt. Lett.* **22**, 1494 (1997).
7. A. Shirakawa *et al.*, *Appl. Phys. Lett.* **74**, 2268 (1999).
8. E. J. Divall and I. N. Ross, *Opt. Lett.* **29**, 2273 (2004).
9. T. V. Andersen *et al.*, *Opt. Express* **14**, 4765 (2006).
10. C. Schriever *et al.*, *Opt. Lett.* **33**, 192 (2008).
11. J. Bromage, C. Dorrer, and J. D. Zuegel, *Opt. Lett.* **35**, 2251 (2010).
12. A. Braun *et al.*, *Opt. Lett.* **20**, 1889 (1995).
13. P. F. Curley *et al.*, *Opt. Commun.* **120**, 71 (1995).
14. G. Cerullo and S. De Silvestri, *Rev. Sci. Instrum.* **74**, 1 (2003).
15. J. Bromage, C. Dorrer, M. Millecchia, J. Bunkenburg, R. Jungquist, and J. D. Zuegel, in *Conference on Lasers and Electro-Optics 2012*, OSA Technical Digest (online) (Optical Society of America, 2012), Paper CTh1N.7.
16. D. N. Schimpf *et al.*, *Opt. Express* **16**, 10,664 (2008).

Computational Chemistry Modeling and Design of Photoswitchable Alignment Materials for Optically Addressable Liquid Crystal Devices

Introduction

Photoalignment technology has received great interest as an alternative to buffed alignment layers for generating high-quality, uniform molecular alignment in liquid crystal (LC) devices. Numerous examples exist in the literature where photoalignment technology has been applied to the development of new LC devices designed to solve difficult application problems in optics and photonics.^{1–9} The near-IR laser-damage resistance of coumarin-based photoalignment layers, developed at the Laboratory for Laser Energetics (LLE), approaches that of fused silica (over 60-J/cm², 1-ns pulse). In addition, these layers have made it possible to fabricate a wide variety of photoaligned LC devices for high-peak-power laser applications, including wave plates, beam shapers, apodizers, and radial polarization converters.^{1–4} Certain classes of photosensitive materials (e.g., azobenzenes and spiropyrans) can undergo *reversible* changes in molecular shape when exposed sequentially to UV or visible light. For azobenzene materials, this photomechanical isomerization between the rod-like *trans* state and the bent *cis* state occurs rapidly and reversibly over time scales of milliseconds at energy levels in the UV and visible regions of <250 mW/cm² [Fig. 143.29(a)].^{10,11} For example, azobenzene molecules attached as pendants to a polymer back-

bone through a flexible hydrocarbon spacer chain can function as a photoactive “command surface.” These pendants, when deposited on the inner surfaces of an LC device as an alignment coating, can be switched optically between two different alignment states using low-incident-energy polarized UV and visible light.^{11–13} This photoisomerization of the azobenzene pendants on the alignment coating redirects the orientation of the LC material in contact with the coating surface in response to the wavelength of the polarized “write” (UV) or “erase” (visible) incident light. Depending on the molecular geometry of the polymeric command surface, the resultant LC reorientation could be constrained to occur either out of plane (orthogonal) or in plane (azimuthal) of the substrate. A conceptual drawing of this behavior is shown in Fig. 143.29(b).

In previously reported work, we identified a series of commercially available azobenzene photoswitchable alignment materials with 1054-nm, 1-ns laser-damage thresholds ranging from 28 to 67 J/cm², which is comparable to reported values for coumarin photoalignment materials used in passive photoaligned LC devices intended for high-peak-power laser applications.^{6,14} Such optically switchable azobenzene command surfaces are being investigated actively for use in an “optically

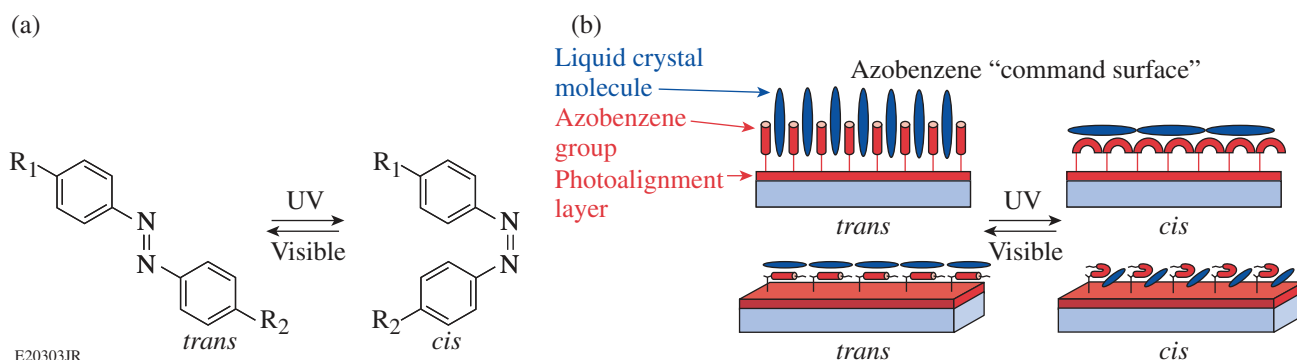


Figure 143.29

(a) *Trans*–*cis* isomerization in azobenzenes. (b) Photoswitchable “command surfaces” with azobenzene pendant groups. Azobenzene groups in the elongated *trans* state (left) cause liquid crystal (LC) molecules to adopt an orientation parallel to the azobenzene’s long molecular axis, while azobenzenes in the bent *cis* state (right) switch the orientation of the LC to a near-parallel orientation to the substrate to minimize their free energy. Depending on the molecular structure of the command surface, the resultant LC reorientation could be constrained to occur either out of the substrate plane (top) or in the plane of the substrate (bottom). This change in orientation induces a change in the polarization, phase, or amplitude of an incident optical beam.

addressed” LC spatial beam shaper concept intended for high-peak-power beam shaping in the 4-PW, 10-ps OMEGA EP Nd:glass solid-state laser at LLE.^{6,14} These optically addressed LC beam shapers are intended ultimately to replace electro-optical LC programmable spatial light modulators. Their application is limited to low-fluence locations in OMEGA EP beamlines because of the low laser-damage thresholds (250 to 500 mJ/cm² at 1054-nm, 1-ns pulse width) of the conductive oxide coatings required for their operation. A schematic diagram of the device concept is shown in Fig. 143.30. The LC molecules can be spatially varied between two alignment states by using low-energy polarized UV/visible light incident on the photoswitchable polymer alignment coating. This provides the in-system write/erase flexibility of electro-optical LC spatial beam shapers while eliminating conductive coatings and electrical interconnects that reduce laser-damage threshold and increase device fragility and complexity, respectively.

To date, the bulk of ongoing research in photoswitchable alignment coating technology is limited primarily to one class of photoactive chromophore (azobenzenes) in the form of low-molar-mass, water-soluble salts deposited either directly on the substrate surface or dispersed in a polymer binder. Progress in developing new photoalignment material systems with enhanced properties has been limited by the largely empirical “trial-and-error” approach, based on intuition and previous experience, that has been used to date. This process is time consuming, labor intensive, and wasteful of costly and potentially scarce materials resources because of the need to synthesize a large number of compounds to establish trends in physical properties. Applying computational chemistry methods to the design and development of new photoswitchable alignment materials

presents itself as an unprecedented opportunity to develop predictive capabilities that will lead to materials with low switching energies, enhanced bistability, and resistance to both write/erase fatigue and laser damage. The effectiveness of this approach has been demonstrated widely in the pharmaceutical industry and in the development of organic light-emitting diode materials and LC mesogens.¹⁵ As recently as 2015, computational studies of functional group effects on azobenzene chromophores are beginning to appear in the literature.^{16,17} Earlier studies to determine free-space volume,¹⁸ photoisomerization mechanisms, relationships between molecular structure and thermal relaxation,¹⁸ dipole moments, polarizabilities, Gibbs free energies, highest-occupied/lowest-unoccupied molecular orbital (HOMO/LUMO) band-gap energies, and chemical potentials using semiempirical computational chemistry methods have also been reported.¹⁷ In this work, we describe efforts to extend the application of the density functional theory (DFT) and time-dependent density functional theory (TDDFT) to determine the effect of molecular structure and functional groups on optical switching state energies in a series of novel photoswitchable alignment methacrylate and acrylamide polymers functionalized with azobenzene and spiropyran pendants.

Computational Chemistry Methods

Three types of computational methods are widely used in molecular mechanics and excited-state calculations. *Semiempirical* quantum chemical methods such as Zerner’s intermediate neglect of differential overlap (ZINDO)¹⁹ have the advantage of reduced computational time (and cost) by using existing experimental data with approximations to fit the calculations according to known parameters. This savings in computational time is obtained at a penalty; the method is

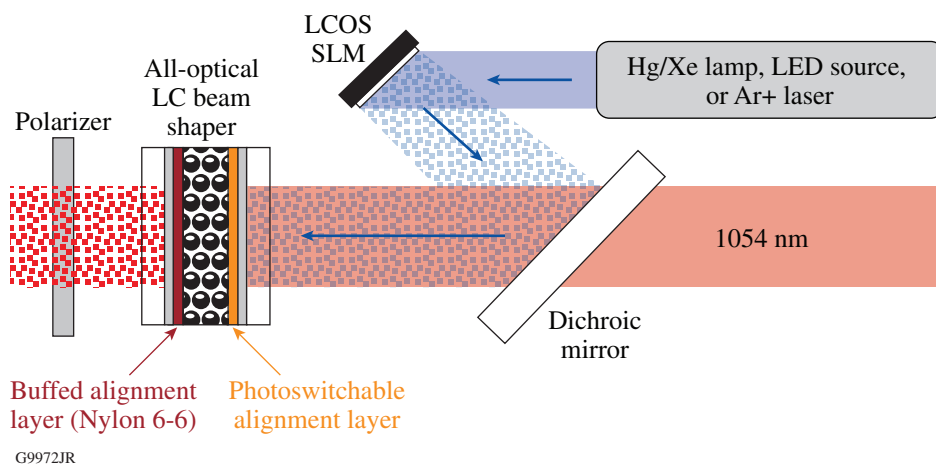


Figure 143.30

A conceptual layout for an all-optical beam shaper using a switchable photoalignment coating. Incident UV light from any number of incoherent or coherent sources [Hg/Xe lamp, light-emitting-diode (LED) source, or Ar+ or HeCd laser] provides the write illumination to a liquid crystal on silicon (LCOS) device, whose image plane is focused onto the photoalignment layer within the device. Patterns produced on the LCOS are written, erased, and rewritten on the photoalignment layer using either alternating UV incident polarizations or serial applications of UV and visible light. Alternatively, patterns can be written and erased directly using a raster-scanned polarized UV laser source. SLM: spatial light modulator.

limited in accuracy by the degree of similarity between the molecule being studied and existing molecules that are used as the parameter source. *Ab initio* methods are not based on existing experimental data but instead employ simulations that are run “from the beginning” using physical principles. The most frequently employed method for *ab initio* calculations is the Hartree–Fock method, which is based on several key assumptions: (1) all nuclei are motionless with respect to the electrons; (2) electron orbitals are expressed as one-electron functions centered on each atom; and (3) the multi-electron calculation of the model is given by the sum of all single-electron calculations of the molecule.²⁰ Relativistic effects and electron correlation effects (electron–electron interactions) are generally neglected. One disadvantage of the Hartree–Fock method is that its accuracy decreases with increasing molecular size.²⁰ Hartree–Fock calculations are usually used to approximate the ground-state energy of a molecular system. Post-Hartree–Fock methods such as the configuration interaction-single (CIS) method have been developed to allow excited-state calculations. Although these improved methods provide better accuracy, they do so at a substantially increased computational cost, are limited to single excitations, and are not highly accurate for larger molecules.^{20–22}

Recently, DFT and TDDFT have emerged as useful and efficient methods for calculating ground-state and excited-state properties, respectively.²³ These methods replace the many-electron wave function (a complex mathematical function in multidimensional space that takes into account individual electrons) used in Hartree–Fock calculations with an electron density function in three spatial dimensions. This approach greatly reduces the computational time without substantially sacrificing accuracy.²⁴ Figure 143.31 compares computed visualizations of wave functions versus electron density func-

tions for the same molecule. The TDDFT method models the evolution of the system’s electron density as a function of time in response to an external disturbance.²³ Jacquemin^{25,26} and Perpète²⁷ used TDDFT extensively to model the absorbance spectra of a series of indigo, nitro-diphenylamine, and anthraquinone-based organic dyes and consistently demonstrated the high accuracy of TDDFT for these materials. These results, along with our previous experience in using DFT and TDDFT for similar calculations in large, complex molecular systems,²⁸ led us to choose this computational method for our studies.

Computational Resources

All DFT and TDDFT calculations were conducted using one of two computer servers in the LLE Computing Facility (LCF): a Dell PowerEdge R710 server [8-core, 2.4-GHz Intel Xeon E5530 CPU (16 virtual cores with hyperthreading), 48 GB of memory connected to NFS4 computing storage over a 1-GB network] or an HP ProLiant SL250s Gen 8 server (24-core, 2.4-GHz Intel Xeon E5-2695v 2 CPU) with 256 GB of memory connected to BFS4 compute storage over a 1-GB network. Schrödinger’s Materials Science Suite Release 2014-3 (Ref. 29) was the primary software package used for the computations. Molecular structures for evaluation were constructed using *Maestro*, the visualization component of the Material Science Suite. *Maestro* includes a qualitative optimization routine that rapidly generates an approximate minimum-energy configuration of the molecular structure. Pre-optimized molecular structure files generated by *Maestro* were then used as input to the *Jaguar* computational chemistry engine contained in the Materials Science Suite for a more-rigorous geometry optimization using DFT. For certain molecular structures, it became necessary to repeat the DFT optimization process several times when the structures reached a level of complexity that exceeded the allowable iteration limits. The fully energy-minimized

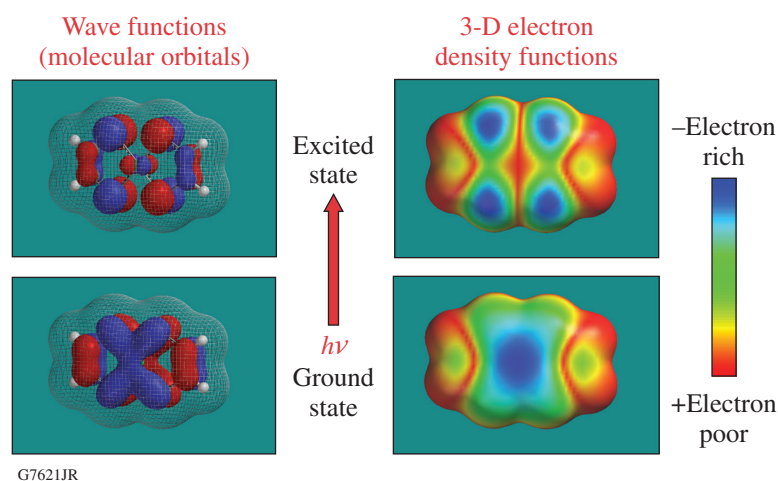


Figure 143.31

A comparison of computed visualizations of wave functions versus electron density functions for the same molecule.

structures were then used as input for the TDDFT calculations used to model the excited-state absorption spectra. (This work will be reported in a future publication.)

For ground-state geometry calculations, we used the basis set 6-31G** for the initial qualitative minimizations since it allowed us to use polarization on all atoms (including hydrogens); it can also produce good results with minimal computational resources. To determine single-point energy values for the *trans* and *cis* states of azobenzenes (and the corresponding open-ring and closed-ring forms of spiropyrans), we initially used the 6-311G-3DF-3PD basis set. This basis set has two sizes of extended Gaussian functions and produces a more-exact solution to the Schrödinger equation, but because of the large amount of computational resources required and long computation times (more than 168 h for one compound), it was used primarily for the final energy calculations.

Table 143.VI lists the computational parameters used to model all of the candidate materials evaluated in this study. Once this series of parameters had been established, only the

Table 143.VI: Computational parameters used to model the investigated candidate materials. The only variable for each computational run was the maximum number of iterations (shown in red), which needed to be increased for more-complex structures.

	Optimization	Energy
Input		
Basis Set	6-31G	6-311G-3DF-3PD
Polarization	**	none
Diffuse	none	none
Theory		
Level of theory	DFT	DFT
SCF spin treatment	restricted	restricted
Recommended	B3LYP	B3LYP
Self-consistent field		
Accuracy level	ultrafine	ultrafine
Initial guess	atomic overlap	atomic overlap
Maximum iterations	200	200
Energy change	5×10^{-5}	5×10^{-5}
rms density matrix change	5×10^{-6}	5×10^{-6}
Optimization		
Maximum steps	500	N/A
Convergence criteria	default	N/A
Initial Hessian	Schlegel guess	N/A
Output		
Calculation stage	At end of job	At end of job

iteration limits were changed to provide enough computing cycles for the self-consistent field (SCF) energy to converge for more-complex structures. Computation of the electronic spectrum for each compound after completing the DFT energy optimization is initiated by selecting the TDDFT option under the “Theory” tab of the *Jaguar* software menu.

Modeling Strategy

Our initial goal for this effort was to evaluate molecular structural elements that would contribute to a high level of bistability in the photoswitchable alignment layer. The following components are considered beneficial in achieving a high level of bistability for optical switching: (1) a significant difference in the isomerization activation energy; (2) a reduced potential energy level for the *cis* state to prevent relaxation back to the *trans* state; and (3) the free-space volume required by the core and pendants (for in-plane switching). The energy diagram in Fig. 143.32 shows how the first two parameters can affect system bistability. If the isomerization energy barrier between the two states becomes too large, it will become difficult to achieve optical switching.³⁰

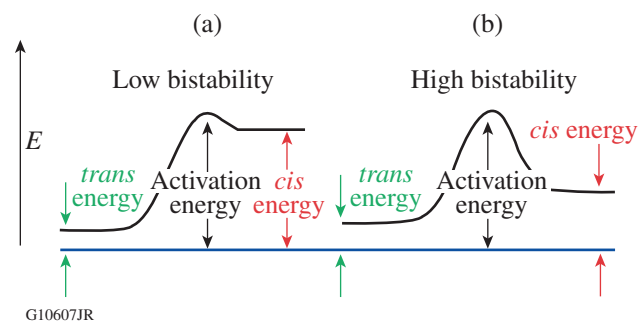


Figure 143.32

Comparison of energy diagrams for photoswitchable azobenzene alignment layers. (a) A system with low bistability. The activation energy barrier required to switch from the *trans* state to the *cis* state is large, while the energy barrier for the reverse transition from *cis* to *trans* is relatively shallow, making it easier to convert back to the *trans* isomer. (b) A system with high bistability. Here the energy barrier between both the *trans*–*cis* and *cis*–*trans* states is large, and once switched into the *cis* state, the material will remain in that state indefinitely. The large activation energy barrier also means that a larger amount of optical energy will be necessary to induce switching.

In this work, we concentrated on modeling the energy difference between the *trans* and *cis* states in methacrylate and acrylamide oligomers, which consist of a single photomechanically switchable chromophore substituted with various terminal functional groups that is linked by an alkyl spacer chain, or “tether,” to a backbone consisting of several methacrylate or acrylamide monomeric repeat units. Figure 143.33 shows a typi-

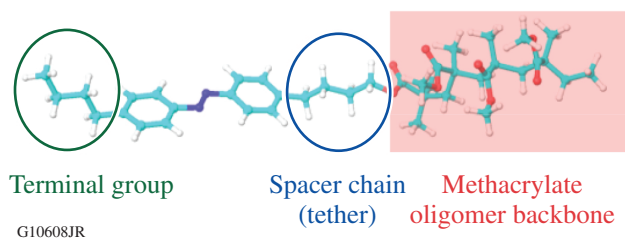


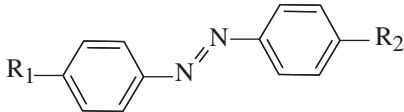
Figure 143.33

An example of a single azobenzene repeat unit used in the simulations. This azobenzene contains a four-carbon alkyl *terminal group* and is connected to the methacrylate oligomer on the far right by a four-carbon spacer chain, or *tether*. A large number of these short backbones consisting of such “repeat units” would be linked together to form the polymer backbone by polymerization of the methacrylate groups at the ends of the oligomer chain.

cal example of such a model compound based on a methacrylate backbone and an azobenzene chromophore.

Because of the large amounts of computational resources and time required to accurately model a complete polymer system with a large number of repeat units, we chose to limit the modeling to oligomers with only one tethered chromophore and four repeat units in the backbone. To compare the terminal functional group’s contributions to the *trans* and *cis* energy states, the alkyl spacer chain length was limited to four repeat units. Computational efforts focused on three different molecular aspects: (1) the length of the alkyl tether, (2) the composition of the terminal group attached to the azobenzene core, and (3) the oligomer backbone structure. Typical computation times for each oligomeric material ranged from 10 min to >96 h for geometry optimization and 5 min to >120 h for energy calculations, depending on the complexity of the structure.

Table 143.VII: Comparison of calculated versus literature values for a series of substituted azobenzene chromophores. Note that the calculated energy values in this table are expressed as negative numbers to aid comparison to literature values; elsewhere, energy differences are reported as the absolute values for simplicity.

 G10609JR	R ₁	R ₂	<i>trans</i> energy (hartrees)	<i>cis</i> energy (hartrees)	Energy difference (hartrees)	Energy difference (kJ/mol)	
						Calculated	Literature values ¹⁷
	H	H	-572.78	-572.75	0.0239	-62.69	-64.20
	OH	H	-648.00	-647.97	0.0250	-65.76	-69.50
	EtOH	H	-726.62	-726.60	0.0241	-63.26	-66.20
	NO ₂	NH ₂	-832.64	-832.62	0.0243	-63.39	-66.67
	H	NH ₂	-628.14	-628.11	0.0244	-64.19	-70.10

To initially test the modeling accuracy of the *Jaguar* software, we conducted *trans* and *cis* potential energy calculations using the 6-31G(d,p) basis set on a series of substituted azobenzene chromophores reported in the literature by Piyanzina *et al.*¹⁷ Table 143.VII compares the results obtained from these calculations to the literature values. The agreement between the calculated and literature results is remarkable, considering that Piyanzina *et al.* used in their calculations the more-complex (and computationally intensive) 6-31G++G (d,p) basis set that is reported to produce more-accurate results than 6-31G (d,p) because of the inclusion of additional functions that provide a better fit to the Schrödinger equation.

Results and Discussion

1. Azobenzene Chromophores

a. Effect of flexible alkyl tether length. The effect of alkyl tether length on the oligomer potential energy for materials containing an azobenzene core in the *trans* and *cis* isomeric states, respectively, was initially modeled with a methoxy group occupying the *para* position on the azobenzene core to reduce computation time. Methacrylate and acrylamide oligomers with backbones composed of four repeat units and alkyl tether chain lengths ranging from C₁ to C₁₂ were evaluated (Fig. 143.34). Table 143.VIII gives the calculated energies for the *trans* and *cis* states for the methacrylate and acrylamide oligomers, respectively. Both data sets are plotted in Fig. 143.35 for comparison.

For the methacrylates, alkyl tether lengths of 5, 6, 8, 9, and 11 carbon atoms produced lower differences in isomerization state energy, with the 6 and 11 carbon tethers providing the greatest reductions in the isomerization energy state. Sudden and steep variations in energy differences as the tether length increased

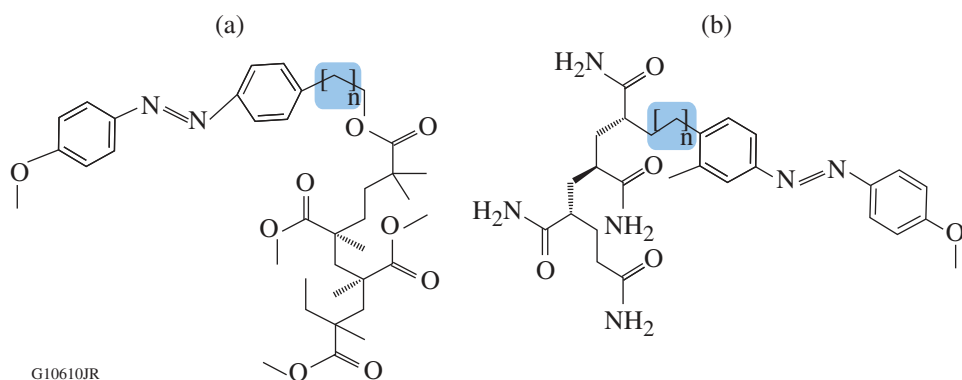


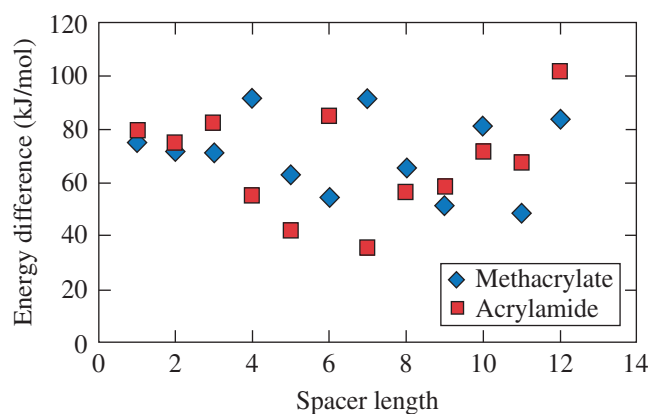
Figure 143.34

Molecular structures of the oligomeric methoxy-substituted azobenzene materials used to test the effect of alkyl tether length on potential energy in the *trans* and *cis* states: (a) methacrylate backbone; (b) acrylamide backbone. Both backbones were limited to four repeat units. The tether length n ranged from C_1 to C_{12} .

G10610JR

Table 143.VIII: Calculated potential energy difference values for the *trans* and *cis* energy states for methoxy-substituted azobenzene cores tethered to methacrylate and acrylamide backbones by alkyl chains ranging in length from 1 to 12 carbon atoms. The values in red indicate those materials with the lowest energy state differences.

Spacer length	<i>trans</i> energy (hartrees)	<i>cis</i> energy (hartrees)	Energy difference	
			(hartrees)	(kJ/mol)
Methacrylate backbone				
1	-2149.20	-2149.18	0.0285	74.87
2	-2188.53	-2188.50	0.0272	71.48
3	-2227.84	-2227.82	0.0271	71.22
4	-2267.16	-2267.13	0.0348	91.45
5	-2306.47	-2306.45	0.0241	63.20
6	-2345.78	-2345.76	0.0208	54.55
7	-2385.11	-2385.08	0.0350	91.90
8	-2424.40	-2424.38	0.0251	65.81
9	-2463.73	-2463.71	0.0195	51.15
10	-2503.06	-2503.03	0.0310	81.31
11	-2542.37	-2542.35	0.0184	48.36
12	-2581.69	-2581.66	0.0319	83.86
Acrylamide backbone				
1	-1715.97	-1715.94	0.0302	79.21
2	-1755.28	-1755.25	0.0286	75.16
3	-1794.59	-1794.56	0.0314	82.41
4	-1833.91	-1833.89	0.0210	55.18
5	-1873.23	-1873.21	0.0160	41.91
6	-1912.55	-1912.52	0.0323	84.88
7	-1951.86	-1951.84	0.0135	35.35
8	-1991.17	-1991.15	0.0215	56.32
9	-2030.49	-2030.47	0.0223	58.63
10	-2069.81	-2069.78	0.0271	71.27
11	-2109.12	-2109.10	0.0255	67.08
12	-2148.45	-2148.41	0.0387	101.64



G10611JR

Figure 143.35

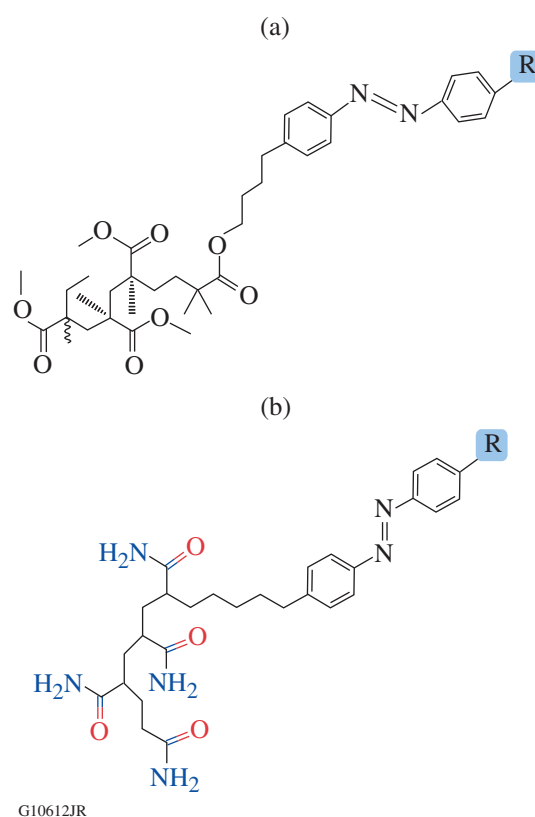
Plot of the calculated difference in energy between *trans* and *cis* states versus tether length for the data shown in Table 143.VIII.

were also observed, with an apparent odd–even effect occurring when the tether contained between 8 and 12 carbon atoms. We speculate that this effect may be caused by chain folding in the alkyl tether and must be investigated in more detail.

In contrast, the acrylamide oligomers show the lowest *trans*–*cis* isomerization energy differences when the alkyl tethers contains 4, 5, 7, 8, and 9 carbon atoms, with some of these values noticeably smaller than those of their methacrylate counterparts. No odd–even effect as a function of tether chain length is seen in this series. It would be of interest to see if the effect occurs if the tether length is longer than 12 carbon atoms. The large differences in isomerization state energies observed in the methacrylate oligomer with C_4 and C_7 tethers and the acrylamide oligomer with a C_{12} tether imply that these materials would be a poor choice for a photoalignment coating intended for bistable switching applications.

b. Effect of terminal groups. We evaluated 22 different terminal groups computationally to determine their individual effects on the potential energy difference between the *trans* and *cis* state when used as substituents on azobenzene cores linked through a four-carbon tether to the same methacrylate and acrylamide backbones used in the computations in the previous subsection. Representative structures for these oligomers are shown in Fig 143.36. Calculated values for both methacrylate and acrylamide oligomers with azobenzene cores are included as a benchmark reference.

Table 143.IX gives the calculated differences in the *trans* and *cis* energy states for oligomers containing alkyl-substituted



G10612JR

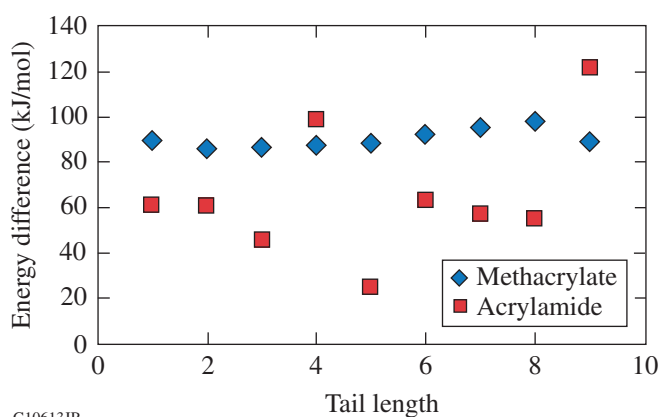
Figure 143.36

Molecular structures of the oligomeric azobenzene materials used to evaluate the effect of a variety of terminal groups (denoted as “R” in the figure) on potential energy in the *trans* and *cis* states: (a) methacrylate backbone; (b) acrylamide backbone. Both the backbones and alkyl tether chains were limited to four repeat units.

azobenzene chromophores. In Fig. 143.37, both data sets are plotted as a function of the terminal alkyl group carbon number for comparison. The alkyl terminal group length appears to have a limited ability to lower the isomerization state energy difference in the methacrylate oligomers. Only a slow, steady increase in energy difference between the *trans* and *cis* states is observed as the alkyl chain increases, reaching a maximum at C_8 and then dropping back at C_9 to the same value as seen for shorter chain lengths. In contrast, changing the alkyl terminal chain length in the acrylamide oligomers produces large fluctuations in isomerization state energy differences between C_3 and C_5 , a plateau between C_6 to C_8 , and a sharp jump at C_9 . All of the acrylamide oligomers (with the exception of those containing C_4 and C_9 terminal groups) show consistently lower *trans*–*cis* energy state differences than their methacrylate counterparts. They also show the lowest (25.10 for C_5) and highest (121.83 for C_9) energy differences of all evaluated alkyl terminal groups.

Table 143.IX: Calculated values of *trans-cis* isomerization energy for tethered azobenzenes with various alkyl terminal group lengths on methacrylate and acrylamide backbones. The azobenzene is tethered to the backbone using a four-carbon alkyl chain. The values in red indicate those materials with the lowest energy state differences.

Terminal group	<i>trans</i> energy (hartrees)	<i>cis</i> energy (hartrees)	Energy difference	
			(hartrees)	(kJ/mol)
Methacrylate backbone				
None	-2152.63	-2152.60	0.0333	87.50
Methyl	-2191.954	-2191.92	0.0342	89.78
Ethyl	-2231.27	-2231.24	0.0328	86.21
Propyl	-2270.59	-2270.55	0.0331	86.83
Butyl	-2309.90	-2309.87	0.0334	87.79
Pentyl	-2349.22	-2349.189	0.0336	88.24
Hexyl	-2388.54	-2388.50	0.0351	92.21
Heptyl	-2427.85	-2427.82	0.0366	96.02
Octyl	-2467.17	-2467.13	0.0373	97.85
Nonyl	-2506.49	-2506.45	0.0340	89.26
Acrylamide backbone				
None	-1719.40	-1719.37	0.0227	59.71
Methyl	-1758.71	-1758.68	0.0233	61.14
Ethyl	-1798.03	-1798.01	0.0232	60.90
Propyl	-1837.32	-1837.33	0.0175	45.82
Butyl	-1876.67	-1876.63	0.0377	98.97
Pentyl	-1915.97	-1915.96	0.0096	25.10
Hexyl	-1955.30	-1955.28	0.0243	63.67
Heptyl	-1994.60	-1994.58	0.0217	56.90
Octyl	-2033.92	-2033.90	0.0209	54.80
Nonyl	-2073.25	-2073.21	0.0464	121.83



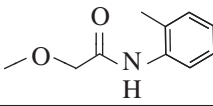
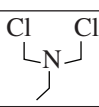
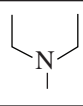
G10613JR

Figure 143.37

Plot of the difference in energy between *trans* and *cis* states versus alkyl terminal group length for the data shown in Table 143.IX.

Table 143.X lists the remaining terminal groups used as substituents on azobenzene methacrylate and acrylamide oligomers evaluated computationally for their *trans-cis* isomerization state energies. For the methacrylate oligomers shown in Table 143.X, the smallest difference in *trans-cis* isomerization energy levels occurs for those materials containing the cyanate ester and 2-methoxy-N-(2-methylphenyl) acetamide terminal groups. For these compounds, the *trans-cis* isomerization energy differences were lower than those for the same backbone containing an unsubstituted azobenzene core by 16% and 72%, respectively. The acrylamide oligomers also show a large decrease in *trans-cis* isomerization state energy differences with the 2-methoxy-N-(2-methylphenyl) acetamide group (62%). The fluoroalkane terminal group produced the largest decrease in the study (nearly 70% lower than the unsubstituted azobenzene core).

Table X: Calculated values of *trans*–*cis* isomerization energy for tethered azobenzenes with a variety of terminal groups on methacrylate and acrylamide backbones.

Backbone	Terminal group	Structure	<i>trans</i> energy (hartrees)	<i>cis</i> energy (hartrees)	Energy difference (hartrees)	Energy difference (kJ/mol)
Methacrylate	None		-2152.63	-2152.60	0.0333	87.50
Acrylamide			-1719.40	-1719.37	0.0227	59.71
Methacrylate	Chloro	— Cl	-2612.23	-2612.19	0.0338	88.71
Acrylamide			-2179.00	-2178.97	0.0229	60.06
Methacrylate	Fluoro	– F	-2251.87	-2251.83	0.0336	88.11
Acrylamide			-1818.62	-1818.61	0.00676	17.76
Methacrylate	Trichloromethyl	– CCl ₃	-3570.71	-3570.68	0.0322	84.62
Acrylamide			-3137.45	-3137.43	0.0214	56.09
Methacrylate	Trifluoromethyl	– CF ₃	-2489.67	-2489.64	0.0303	79.58
Acrylamide			-2056.43	-2056.41	0.0247	64.73
Methacrylate	Cyanate ester	—O—C≡N	-2320.06	-2320.03	0.0278	73.07
Acrylamide			-1886.80	-1886.70	0.0274	71.99
Methacrylate	Hydroxyl	— OH	-2227.86	-2227.82	0.0336	88.17
Acrylamide			-1794.61	-1794.58	0.0321	84.35
Methacrylate	2-methoxy-N-(2-methylphenyl)acetamide		-2706.24	-2706.23	0.00939	24.65
Acrylamide			-2272.94	-2272.93	0.00855	22.46
Methacrylate	Amino	— NH ₂	-2207.99	-2207.96	0.0336	88.25
Acrylamide			-1774.72	-1774.70	0.0219	57.47
Methacrylate	Nitrile	C≡N	-2244.88	-2244.84	0.03304	86.76
Acrylamide			-1811.58	-1811.60	0.0208	54.50
Methacrylate	N, N-bis (chloromethyl)ethanamine		-3245.11	-3245.08	0.0305	80.02
Acrylamide			-2811.81	-2811.79	0.0261	68.54
Methacrylate	Diethylamino		-2365.24	-2365.21	0.0305	79.98
Acrylamide			-1932.00	-1931.97	0.0236	62.07
Methacrylate	Piperidine		-2403.36	-2403.32	0.034	90.70
Acrylamide			-1970.12	-1970.09526	0.0280	73.45
Methacrylate	Pyrrolidine		-2364.00	-2364.001	0.03340	89.25
Acrylamide			-1930.81	-1930.78	0.0235	61.79

G10625JR

2. Spiropyran Chromophores

Preliminary modeling using the same methods as used for **Azobenzene Chromophores** (p. 154) was applied to acrylamide oligomers containing methoxy-substituted spiropyran chromophores tethered to the backbone using alkyl chains of varying lengths [Fig. 143.38(a)]. Unlike azobenzenes, where no bonds are broken during photoisomerization, spiropyrans

undergo a reversible photomediated ring opening/closing reaction upon absorption of UV and visible light [Fig. 143.38(b)].

Table 143.XI compares the calculated energy difference between the closed and open forms for an unsubstituted spiropyran chromophore tethered to an acrylamide oligomer backbone by a C₄ alkyl chain to the calculated *trans*–*cis* photo-

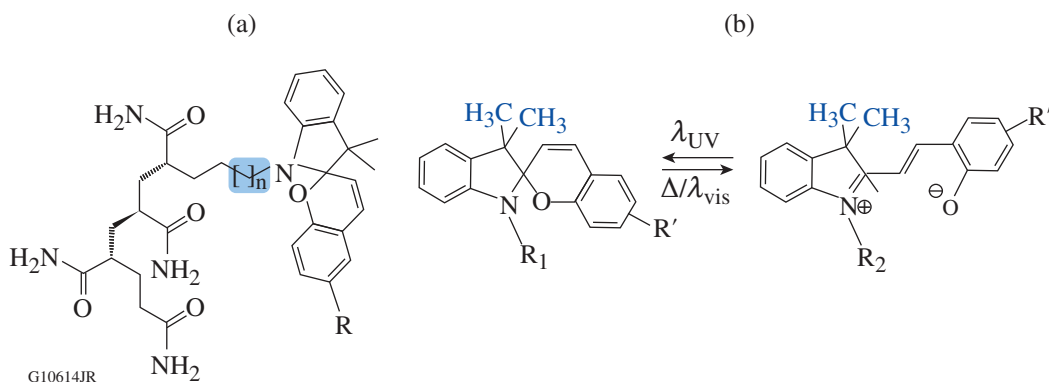


Figure 143.38

(a) A methoxy-substituted spiropyran tethered with alkyl chains of differing lengths to an acrylamide backbone (the tether is shaded in blue); (b) the mechanism for photomediated ring opening/closing reaction in spiropyrans.

Table 143.XI: The calculated energy difference between the closed and open forms for an unsubstituted spiropyran chromophore tethered to an acrylamide backbone by a C₄ alkyl chain. For comparison we have included the calculated energy differences for the *trans*–*cis* photoisomerization states in an unsubstituted azobenzene chromophore connected to an acrylamide backbone or methacrylate backbone using the same tether length.

Backbone	Chromophore	Terminal group	Spacer length	Open-form energy (hartrees)	Closed-form energy (hartrees)	Energy difference	
						(hartrees)	(kJ/mol)
Acrylamide	Azobenzene	None	4	-1719.40	-1719.37	0.0227	59.71
	Spiropyran			-1972.72	-1972.75	0.0316	83.01
Methacrylate	Azobenzene			-2152.63	-2152.60	0.0333	87.50

isomerization energy differences for unsubstituted azobenzene chromophores connected to acrylamide and methacrylate backbones using the same tether length. Although the energy state differences for the spiropyran acrylamide oligomer are higher than for the corresponding azobenzene oligomer, they are comparable to those calculated for the azobenzene chromophore connected to a *methacrylate* backbone through a C₄ alkyl chain. Calculations are in progress to determine the closed-form and open-form energy differences for other spiropyran oligomers with methacrylate, acrylamide, and siloxane backbones tethered to substituted spiropyran chromophores using a variety of alkyl chain lengths.

Conclusions and Future Work

Computational modeling was used to determine the properties of a series of oligomeric methacrylate and acrylamide photoswitchable alignment layer materials intended as potential candidates for use in an optically switchable LC laser beam shaper. Photoisomerization energy state differences in model compounds were calculated using DFT and TDDFT compu-

tational methods (Materials Science Suite, Schrödinger, Inc.) employing the 6-31G** basis set. Twenty-two different terminal functional groups were evaluated computationally to determine their individual effects on the energy difference between the *trans* and *cis* isomerization-state energy levels (one of the three factors affecting bistability in photoswitchable alignment layers) when they were used as substituents on azobenzene cores linked through a four-carbon tether to methacrylate and acrylamide backbones. The effect of the alkyl tether connecting the chromophore to the oligomer backbone on the isomerization state energy differences of the methacrylate and acrylamide oligomers was also investigated computationally. This work revealed a number of key findings:

1. When methoxy-substituted azobenzene chromophores are tethered to a *methacrylate oligomer*, lower energy differences between the *trans* and *cis* isomerization states occur for alkyl tether lengths of 5, 6, 8, 9, and 11 carbons. The C₆ and C₁₁ tethers produce the smallest energy difference, implying that they are a good choice for a photoalignment

coating intended for bistable switching applications. For the same core and an alkyl tether length of C₄, replacing the methoxy terminal group on the azobenzene core with alkyl groups up to C₉ appears to have a limited ability to lower the isomerization-state energy difference, while cyanate ester and 2-methoxy-N-(2-methylphenyl) acetamide terminal groups are highly effective in producing the smallest differences in *trans*–*cis* isomerization energy levels.

2. *Acrylamide oligomers* tethered to a methoxy-substituted azobenzene chromophore show the smallest *trans*–*cis* isomerization energy differences for alkyl tethers containing 4, 5, 7, 8, and 9 carbon atoms, in some cases considerably smaller than those of the corresponding methacrylate oligomers. Unlike what was seen for methacrylate oligomers, replacing the methoxy group on the azobenzene core with C₅ and C₉ terminal alkyl groups shows a *significant* reduction in *trans*–*cis* isomerization-state energies. With the exception of C₄ and C₉ terminal groups, all of the acrylamide oligomers with alkyl-substituted azobenzene cores show consistently lower *trans*–*cis* isomerization-state energy differences than do their methacrylate counterparts. Other terminal functional groups that show a large decrease in *trans*–*cis* isomerization-state energy differences are the 2-methoxy-N-(2-methylphenyl) acetamide group (62%) and the fluoroalkane terminal group (70%) as compared to an unsubstituted azobenzene core.
3. With only a few exceptions, acrylamide oligomers as a group exhibit lower *trans*–*cis* isomerization energy differences than methacrylate oligomers with the same structure, making them (in the absence of other factors) preferred candidates for photoswitchable device applications where good bistability is required.

Considerable work remains in developing these computational tools and methodologies into a reliable, predictive capability for photoswitchable alignment layer design. The observed odd–even effect in the *trans*–*cis* isomerization energies as a function of tether chain length seen for methoxy-azobenzene-methacrylate oligomer systems must be more fully investigated for longer tether lengths and on different oligomeric backbones (e.g., methacrylate, acrylamide, siloxane) to determine if it is specific to one oligomer class. Both the transition state energy and the swept volume produced by motion of the chromophore pendant (both azobenzenes and spiropyranes) will be determined by transition state modeling (DFT) and molecular dynamics simulations using the *Jaguar* and *Desmond* components of the Materials Science Suite,

respectively. Highly intensive computational modeling of systems with up to 15 or more backbone segments, along with targeted synthesis and characterization of the most-promising candidate materials from these studies, will lead to both a more-detailed understanding of these materials systems and sufficient quantities of materials for characterization studies and device development activities.

ACKNOWLEDGMENT

This material is based upon work supported by the Department of Energy National Nuclear Security Administration under Award Number DE-NA0001944, the University of Rochester, and the New York State Energy Research and Development Authority. The support of DOE does not constitute an endorsement by DOE of the views expressed in this article. The authors acknowledge M. Charissis of LLE's Computer Support Group for his help in supporting our computation efforts on LLE's Computing Facility. We also acknowledge Dr. S. Kwak and Dr. S. Murdock of Schrödinger LLC for their helpful discussions and guidance in conducting this work.

REFERENCES

1. C. Dorrer, S. K. H. Wei, P. Leung, M. Vargas, K. Wegman, J. Boulé, Z. Zhao, K. L. Marshall, and S. H. Chen, *Opt. Lett.* **36**, 4035 (2011).
2. K. L. Marshall, S. K.-H. Wei, M. Vargas, K. Wegman, C. Dorrer, P. Leung, J. Boule III, Z. Zhao, and S. H. Chen, in *Liquid Crystals XV*, edited by I. C. Khoo (SPIE, Bellingham, WA, 2011), Vol. 8114, Paper 81140P.
3. K. L. Marshall, C. Dorrer, M. Vargas, A. Gnolek, M. Statt, and S.-H. Chen, in *Liquid Crystals XVI*, edited by I. C. Khoo (SPIE, Bellingham, WA, 2012), Vol. 8475, Paper 84750U.
4. K. L. Marshall, J. Gan, G. Mitchell, S. Papernov, A. L. Rigatti, A. W. Schmid, and S. D. Jacobs, in *Liquid Crystals XII*, edited by I. C. Khoo (SPIE, Bellingham, WA, 2008), Vol. 7050, Paper 70500L.
5. S. R. Nersisyan *et al.*, *Opt. Express* **21**, 8205 (2013).
6. K. L. Marshall, D. Saulnier, H. Xianyu, S. Serak, and N. Tabiryan, in *Liquid Crystals XVII*, edited by I. C. Khoo (SPIE, Bellingham, WA, 2013), Vol. 8828, Paper 88280N.
7. J. Vernon *et al.*, *Crystals* **3**, 234 (2013).
8. J. P. Vernon *et al.*, *Opt. Express* **21**, 1645 (2013).
9. J. P. Vernon *et al.*, *Advanced Optical Materials* **1**, 84 (2013).
10. M. Schadt, H. Seiberle, and A. Schuster, *Nature* **381**, 212 (1996).
11. K. Ichimura, *Chem. Rev.* **100**, 1847 (2000).
12. A. Muravsky *et al.*, *J. Soc. Inf. Disp.* **15**, 267 (2007).
13. O. Yaroshchuk and Y. Reznikov, *J. Mater. Chem.* **22**, 286 (2012).
14. K. L. Marshall, O. Didovets, and D. Saulnier, in *Liquid Crystals XVIII*, edited by I. C. Khoo (SPIE, Bellingham, WA, 2014), Vol. 9182, Paper 91820J.

15. E. G. Lewars, *Computational Chemistry: Introduction to the Theory and Applications of Molecular and Quantum Mechanics*, 2nd ed. (Springer, Dordrecht, The Netherlands, 2011).
16. P. C. Chen and Y. C. Chieh, *J. Mol. Struct. (Theochem)* **624**, 191 (2003).
17. I. Piyanzina *et al.*, *J. Mol. Model.* **21**, 1 (2015).
18. C. Ruslim and K. Ichimura, *Macromolecules* **32**, 4254 (1999).
19. M. C. Zerner, *ZINDO, A Semiempirical Quantum Chemistry Program*, Quantum Theory Project (University of Florida, Gainesville, FL, 1996).
20. W. J. Hehre, *Ab Initio Molecular Orbital Theory* (Wiley, New York, 1986).
21. I. N. Levine, *Quantum Chemistry*, 4th ed. (Prentice-Hall, Englewood Cliffs, NJ, 1991), pp. 455–544.
22. C. J. Cramer, *Essentials of Computational Chemistry: Theories and Models* (J. Wiley, West Sussex, England, 2002), pp. 153–189.
23. E. Runge and E. K. U. Gross, *Phys. Rev. Lett.* **52**, 997 (1984).
24. K. I. Ramachandran, G. Deepa, and K. Namboori, *Computational Chemistry and Molecular Modeling: Principles and Applications* (Springer-Verlag, Berlin, 2008).
25. D. Jacquemin *et al.*, *J. Chem. Phys.* **124**, 74104 (2006).
26. D. Jacquemin *et al.*, *J. Chem. Phys.* **121**, 1736 (2004); M. Dubecký *et al.*, *J. Chem. Phys.* **133**, 244301 (2010).
27. E. A. Perpète *et al.*, *J. Chem. Theory Comput.* **2**, 434 (2006).
28. K. L. Marshall, R. Wang, M. Coan, A. G. Noto, K. Leskow, R. Pauszek, and A. Moore, in *Liquid Crystals XI*, edited by I. C. Khoo (SPIE, Bellingham, WA, 2007), Vol. 6654, Paper 66540F.
29. Schrödinger Materials Science Suite, Release 2014-3 (Jaguar, ver. 8.5 and Maestro, ver. 9.9), Schrödinger, New York, NY 10036-4041.
30. J. G. Meier, R. Ruhmann, and J. Stumpe, *Macromolecules* **33**, 843 (2000).

The Temporal Analog of Reflection and Refraction of Optical Beams

Reflection and refraction of light at a dielectric interface and Snell's law describing them have been known for centuries and are topics discussed at length in physics textbooks.^{1,2} However, their temporal analog, where an electromagnetic pulse arrives at a temporal interface, has attracted much less attention.^{3,4} A temporal interface is the boundary in time separating two regions of different refractive indices. In this article we discuss "reflection" and "refraction" of optical pulses at such a temporal boundary during their propagation inside a dispersive medium. Previous works have examined temporal reflection and refraction in nondispersive media assuming that refractive index changes everywhere in the medium at a certain time.^{3,4} This is analogous to examining the case of normal incidence in space. Temporal changes in the refractive index have also been studied recently in the context of adiabatic wavelength conversion.⁵⁻¹¹

From a physics perspective, a spatial boundary breaks translational symmetry. As a result, the momentum of a photon can change but its energy must remain unaffected. In the case of a static temporal boundary, momentum of the photon remains unchanged but its energy must change. For this reason, a change in angle at a spatial interface translates into a change in the frequency of incident light when reflection and refraction occur at a temporal interface. We focus on optical pulses propagating inside a dispersive medium to reveal novel temporal and spectral features occurring when the pulse experiences reflection and refraction at a moving temporal boundary.

To simplify the following discussion, we assume that the optical pulse is propagating inside a waveguide with the dispersion relation $\beta(\omega)$ such that neither its polarization nor its transverse spatial shape changes during propagation. When the pulse contains multiple optical cycles, $\beta(\omega)$ can be expanded in a Taylor series around its central frequency ω_0 as¹²

$$\beta(\omega) = \beta_0 + \beta_1 (\omega - \omega_0) + \frac{\beta_2}{2} (\omega - \omega_0)^2, \quad (1)$$

where we neglect all dispersion terms higher than the second order. Physically β_1 is the inverse of the group velocity and β_2 is the group velocity dispersion (GVD). In the case of a moving temporal boundary, we work in a reference frame in which the boundary is stationary. Using the coordinate transform $t = T - z/v_{\text{GB}}$, where T is the time in the laboratory frame and v_{GB} is the velocity of the temporal boundary, the dispersion relation in the moving frame becomes

$$\beta'(\omega) = \beta_0 + \Delta\beta_1 (\omega - \omega_0) + \frac{\beta_2}{2} (\omega - \omega_0)^2 + \beta_{\text{B}} H(t - T_{\text{B}}), \quad (2)$$

where $\Delta\beta_1 = \beta_1 - 1/v_{\text{GB}}$ is a measure of a pulse's relative speed. The parameter $\beta_{\text{B}} = k_0 \Delta n$ ($k_0 = \omega_0/c$) is the magnitude of the change in the propagation constant caused by the sudden index change Δn at the temporal boundary located at $t = T_{\text{B}}$. The Heaviside function $H(t - T_{\text{B}})$ takes a value of 0 for $t < T_{\text{B}}$ and 1 for $t > T_{\text{B}}$. For $t > T_{\text{B}}$, the last term in Eq. (2) shifts the dispersion curve by β_{B} , leading to different propagation constants in the two temporal regions. We stress that by including dispersion and allowing for a traveling boundary we have expanded on the concept of temporal reflection and refraction given in Ref. 3.

To study the impact of a temporal boundary, we write the electric field associated with the optical pulse in the form

$$E(\vec{r}, t) = \hat{x} F(x, y) A(z, t) \exp(i\beta_0 z - i\omega_0 t), \quad (3)$$

where $F(x, y)$ is the transverse spatial profile and $A(z, t)$ is the slowly varying envelope of the pulse. Use of Maxwell's equations together with the dispersion relation in Eq. (2) then leads to the following time-domain equation:¹²

$$\frac{\partial A}{\partial z} + \Delta\beta_1 \frac{\partial A}{\partial t} + i \frac{\beta_2}{2} \frac{\partial^2 A}{\partial t^2} = i\beta_{\text{B}} H(t - T_{\text{B}}) A. \quad (4)$$

For numerical purposes we normalize this equation using

$$\tau = \frac{t}{T_0}, \quad \xi = \frac{z}{L_D}, \quad A(z, t) = \sqrt{P_0} U(\xi, \tau), \quad (5)$$

where T_0 is the width, P_0 is the peak power of the incident pulse, and $L_D = T_0^2 / |\beta_2|$ is the dispersion length. The normalized amplitude $U(\xi, \tau)$ satisfies

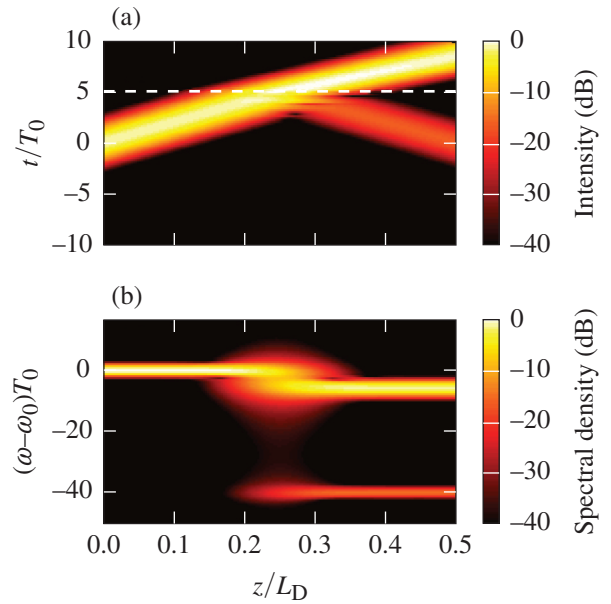
$$\frac{\partial U}{\partial \xi} + d \frac{\partial U}{\partial \tau} + b_2 \frac{i}{2} \frac{\partial^2 U}{\partial \tau^2} = i\beta_B L_D H(\tau - \tau_B) U. \quad (6)$$

where $d = \Delta\beta_1 L_D / T_0$, $\tau_B = T_B / T_0$, and $b_2 = \pm 1$ depending on the sign of β_2 .

We solved Eq. (6) numerically with the standard split-step Fourier method,¹² assuming a Gaussian shape of input pulses. For the numerical simulations that follow, the temporal boundary was located at $\tau_B = 5$ and the dispersion was taken to be normal ($b_2 = +1$). We chose $d = 20$ to ensure that the center of the optical pulse would cross the boundary halfway through the total propagation length of $\xi = 0.5$.

As a first example of temporal reflection and refraction, Fig. 143.39 shows (a) temporal and (b) spectral evolutions of a Gaussian input pulse for $\beta_B L_D = 100$. The temporal evolution in part (a) is strikingly similar to an optical beam hitting a spatial boundary. From Fig. 143.39(a) we see that the trailing edge of the pulse reaches the boundary near $\xi = 0.15$ as the faster temporal boundary begins to overtake the optical pulse. Although most of pulse energy is transmitted across the boundary, the pulse “bends” toward it and its speed changes. The transmitted pulse is also narrower in time, similar to how a refracted optical beam becomes narrower in space when it is bent toward the spatial interface. A small part of pulse energy is “reflected” and begins traveling away from the temporal boundary. This reflected pulse has the same temporal width but its speed increases considerably. In this case both the energy and momentum of a photon must change simultaneously while crossing the boundary.

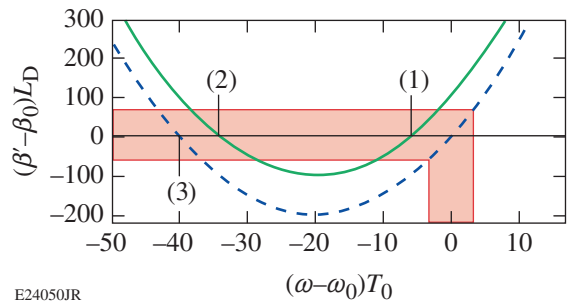
Figure 143.39(b) shows how temporal changes are accompanied by a multitude of spectral changes. In particular, notice how the spectrum shifts and splits as the pulse crosses the temporal boundary. Recall that the temporal analog of an angle is the frequency. From a fundamental perspective, spectral



E24049JR

Figure 143.39 Evolution of (a) the pulse shape and (b) the spectrum in the presence of a temporal boundary at $\tau_B = 5$ (dashed white line) with $\beta_B L_D = 100$. Time is measured in a reference frame that moves with the temporal boundary.

changes occur because a temporal boundary breaks symmetry in time. As a result, photon momentum in the moving frame (or β') must be conserved while photon energy (or ω) may change. This suggests that the dispersion relation in Eq. (2) should be able to explain all spectral changes. Figure 143.40 shows dispersion curves for $\tau < \tau_B$ (dashed blue) and $\tau > \tau_B$ (solid green). In the moving frame, the slope of these curves gives the speed of the pulse relative to the temporal boundary,



E24050JR

Figure 143.40 Normalized dispersion curves for $\tau < \tau_B$ (dashed blue) and $\tau > \tau_B$ (solid green). The shaded region shows the spectral extent of the input pulse and the corresponding range of propagation constants for $\tau < \tau_B$. The slope of the dispersion curve is related to the speed of the pulse relative to the traveling temporal boundary.

rather than the actual group velocity. As mentioned earlier, even though β (related to photon momentum) is not conserved, the corresponding quantity β' is conserved in the moving frame. We use this conservation law to understand the spectral shifts of refracted and reflected pulses.

To conserve β' when transitioning from the $\tau < \tau_B$ region to the $\tau > \tau_B$ region, each frequency component must shift from the dashed curve to a point on the solid curve with the same value of β' . Because the curve is locally parabolic, the two frequencies at points (1) and (2) on the solid curve match the initial value of β' . Only point (1) is a valid solution, however, since the slope, related to the speed of the pulse, should have the same sign for the transmitted pulse. The entire pulse spectrum shifts toward the red side (for $\beta_B > 0$) since each frequency component of the pulse must shift accordingly. Since the slope of the dispersion curve at the new central frequency is different, the transmitted pulse must travel at a different speed relative to the temporal boundary. This change in the group velocity is what leads to the apparent bending observed in Fig. 143.39(a).

The reflected pulse is caused by the second point on the dashed curve that has the same propagation constant, marked as point (3) in Fig. 143.40. This point must have the opposite slope to ensure that the pulse reflects back into the $\tau < \tau_B$ region. We stress that the reflected pulse does not travel backward in time or space; rather its speed is increased so much that it moves away from the temporal boundary. Both the reflected pulse and the temporal boundary continue to propagate through the dispersive medium in the $+z$ direction. Figure 143.39(b) shows that the spectrum of the reflected pulse is shifted toward the red side by about $\Delta\nu = 40/(2\pi T_0)$ or by more than 6 THz for a pulse with $T_0 = 1$ ps. It also shows that the energy transfer occurs over a relatively small distance during which the pulse passes through the temporal boundary.

So far we have considered only the central frequency of the optical pulse. However, the pulse has a finite spectral width and β' must be conserved for all frequencies in the spectrum. In Fig. 143.40, the shaded region shows the width of the input pulse spectrum and the corresponding range of propagation constants for $\tau < \tau_B$. We can see that the shaded region on the transmitted curve covers a much wider spectral region than on the incident curve. This leads to the spectral broadening and temporal narrowing of the refracted pulse. If the sign of β_B was reversed, shifting the curve in the opposite direction, the pulse spectrum would be compressed and the pulse would correspondingly broaden in time.

One may ask how much the momentum changes in the laboratory frame. It is easy to see that $\beta = \beta' + (\omega - \omega_0)/v_{GB}$. Since β' remains constant, β changes by an amount $(\omega - \omega_0)/v_{GB}$. Clearly, a moving boundary breaks both temporal and spatial symmetries, forcing momentum and energy to change simultaneously. This is similar to the behavior observed in interband photonic transitions.¹³

To obtain analytic expressions for the spectral shifts caused during temporal reflection and refraction, we impose the requirement of momentum conservation in the dispersion relation given in Eq. (2). To do so, we choose a specific frequency component, i.e., the center frequency ω_0 , and set $\beta'(\omega) = \beta_0$ in Eq. (2), resulting in the quadratic equation

$$\frac{\beta_2}{2}(\omega - \omega_0)^2 + \Delta\beta_1(\omega - \omega_0) + \beta_B H(t - T_B) = 0. \quad (7)$$

The last term vanishes for $t > T_B$ and the two solutions of the quadratic equation are

$$\omega_i = \omega_0 \quad \text{and} \quad \omega_r = \omega_0 - 2(\Delta\beta_1/\beta_2). \quad (8)$$

These solutions represent the incident and reflected frequencies and correspond to the points (1) and (3), respectively, in Fig. 143.40. The transmitted frequency is found by noting that the last term in Eq. (7) is finite for $t > T_B$ and has the value β_B . Solving the quadratic equation again, we obtain

$$\omega_t = \omega_0 + \frac{\Delta\beta_1}{\beta_2} \left[-1 \pm \sqrt{1 - \frac{2\beta_B\beta_2}{(\Delta\beta_1)^2}} \right]. \quad (9)$$

As discussed earlier, only the positive sign corresponds to a physical solution shown as point (2) in Fig. 143.40. In the limit $\Delta\beta_1 \gg \sqrt{\beta_B\beta_2}$, this equation can be approximated as

$$\omega_t = \omega_0 - \frac{\beta_B}{\Delta\beta_1} = \omega_0 - \frac{k_0\Delta n}{\Delta\beta_1}. \quad (10)$$

The numerical results shown in Fig. 143.39 agree with these analytic expressions derived using the concept of momentum conservation.

The analytical results found in this article provide considerable insight into the phenomena of temporal reflection and refraction of optical pulses. Consider first the frequency shift of the reflected pulse: Eq. (8) indicates that this shift depends

on both the sign and magnitude of the GVD governed by the parameter β_2 . In particular, it disappears as $\beta_2 \rightarrow 0$. It follows from Eq. (2) that the parabolic dispersion curve seen in Fig. 143.40 reduces to a straight line in this limit, indicating that point (3) in Fig. 143.40 ceases to exist. Note also that the direction of frequency shifts depends on the nature of GVD. A red shift occurring for normal dispersion becomes a blue shift in the case of anomalous dispersion. Another noteworthy feature is that the frequency shifts do not depend on the refractive index change Δn across the temporal boundary. Of course, the energy transferred to the reflected pulse depends strongly on the magnitude of β_B . These features are analogous to what occurs at a spatial interface.

We now ask how large the spectral shift can be for the reflected pulse. As discussed earlier, a spectral shift of about 6 THz occurs for the parameters used in Fig. 143.39. Equation (8) indicates that even larger spectral shifts are possible by reducing the magnitude of the GVD parameter; i.e., by operating close to the zero-dispersion wavelength of the waveguide used to observe this phenomenon.

The refracted pulse also undergoes a spectral shift that is analogous to a change in the direction of an optical beam refracted at a spatial boundary. As seen in Eq. (9), this shift depends on the magnitude of β_B , in addition to the GVD parameter β_2 and the differential group delay (DGD) $\Delta\beta_1$ of the pulse. In the limit $\Delta\beta_1 \gg \sqrt{\beta_B\beta_2}$, the spectral shift becomes independent of β_2 . Its magnitude in all cases is much smaller than that found for the reflected pulse. As an example, for an index change of $\Delta n = 10^{-4}$ and $\Delta\beta_1 = 100$ ps/m, this shift is about 1 THz at a wavelength of 1.06 μm .

Although Eqs. (8) and (9) provide the expected frequency shifts, they do not have an obvious resemblance to the spatial laws of reflection and refraction. Indeed, it is difficult to find analogous relations since the concept of an angle, familiar in the spatial context, is replaced with the DGD $\Delta\beta_1$, indicating the speed of the pulse relative to a temporal boundary. Nevertheless, one may gain some insight if we use the location of extremum of the dispersion curve in Fig. 143.40 as a reference frequency ω_c , where the slope $d\beta/d\omega = 0$. If we shift the origin in Fig. 143.40 so that all frequencies are measured from the reference frequency $\omega_c = \omega_0 - \Delta\beta_1/\beta_2$ and use the notation $\Delta\omega = \omega - \omega_c$, the reflected and transmitted frequencies are related to the input frequency as

$$\Delta\omega_r = -\Delta\omega_i, \quad \Delta\omega_t = \Delta\omega_i \sqrt{1 - \frac{2\beta_B\beta_2}{(\Delta\beta_1)^2}}. \quad (11)$$

The first equation is analogous to the law of reflection. The second one can be written in the following suggestive form:

$$\Delta\omega_t = \Delta\omega_i \cos \alpha, \quad \sin \alpha = \sqrt{\frac{2\beta_B\beta_2}{(\Delta\beta_1)^2}}. \quad (12)$$

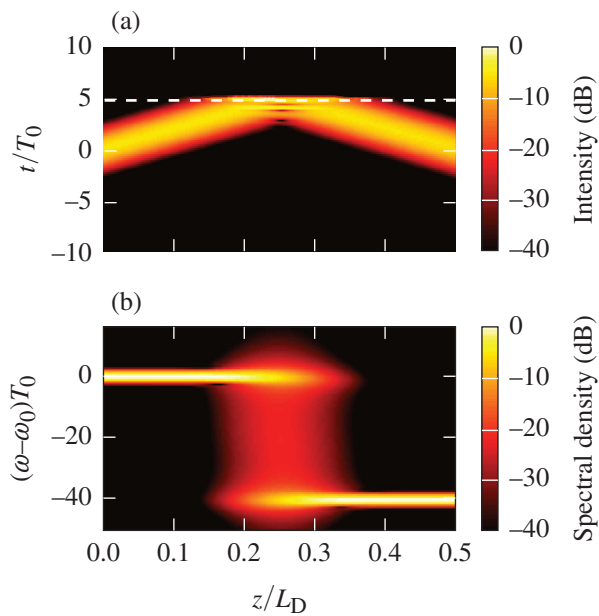
For small values of β_B , α remains relatively small, resulting in small frequency shifts during refraction and small changes in the pulse speed. Frequency shifts increase with increasing β_B . At some value of parameters, α becomes $\pi/2$ and $\Delta\omega_t$ vanishes. At that point, the transmitted pulse's central frequency coincides with the frequency ω_c .

We must ask what happens if β_B is large enough that α loses its meaning. Since $\Delta\omega_t$ becomes undefined, no refracted pulse can form past the temporal boundary and the incident pulse must be totally reflected. This is the temporal analog of the well-known phenomenon of total internal reflection (TIR). The condition for the temporal TIR is found from Eq. (12) to be

$$\sqrt{2\beta_B\beta_2} > \Delta\beta_1. \quad (13)$$

Temporal TIR can also be understood from the two dispersion curves shown in Fig. 143.40. When β_B is large enough to shift the green curve in Fig. 143.40 completely out of the shaded region, momentum conservation or phase matching cannot be achieved for any spectral component of the incident pulse. As a result, no pulse energy can enter the $\tau > \tau_B$ region beyond the temporal boundary; however, the momentum can still be conserved for the reflected pulse. As a result, the pulse should be completely reflected at the boundary. We performed numerical simulations to confirm that this is indeed the case. Figure 143.41 shows the numerical results for $\beta_B L_D = 280$, a value that places the transmitted curve just above the shaded region. As predicted by our simple theory, there is no transmitted pulse and the entire pulse is reflected. The spectral evolution in Fig. 143.41(b) shows how the pulse energy is transferred to the reflected pulse over a small distance after the trailing end of the incident pulse hits the temporal boundary. Closer inspection reveals that a portion of the pulse extends past the temporal boundary, forming a temporal analog to the evanescent wave.

The existence of temporal TIR seems to contradict the findings in Ref. 3, where a temporal analog of Snell's law is derived that does not allow for TIR to occur. However, the study in Ref. 3 did not include the effects of dispersion. Indeed, our theory shows that no reflection occurs if β_2 is set to 0.



E24052JR

Figure 143.41

(a) Temporal and (b) spectral evolutions of an optical pulse undergoing total internal reflection (TIR) at a temporal boundary located at $\tau_B = 5$ (dashed white line). The index change is large enough that $\beta_B L_D = 280$. Time is measured in a reference frame that moves with the temporal boundary.

In summary, we have shown that when an optical pulse approaches a moving temporal boundary across which the refractive index changes, it undergoes a temporal equivalent of reflection and refraction of optical beams at a spatial boundary. The main difference is that the role of angle is played by changes in the frequency. The dispersion curve of the material in which the pulse is propagating plays a fundamental role in determining the frequency shifts experienced by the reflected and refracted pulses. The analytic expressions that we were able to obtain for these two frequency shifts show that the spectral shift is relatively small for the refracted pulse but can be quite large for the reflected pulse. Moreover, the shifts can be either on the red side or on the blue side of the spectrum of the incident pulse, depending on the nature of both the group-velocity dispersion and the refractive index change. These spectral shifts are caused by a transfer of energy between the pulse and the temporal boundary while the number of photons is conserved.³ Because our temporal boundary is induced by an external source, this is not a closed system and energy is not conserved in the pulse. We have also indicated the conditions under which an optical pulse experiences the temporal analog of TIR. Numerical results confirm all analytical predictions

based on the physical concept of momentum conservation in the moving frame.

An experimental observation of reflection, refraction, and TIR at a temporal boundary will be of immense interest. Our estimates show that changes in the refractive index across this boundary can be as small as 10^{-6} for verifying our theoretical and numerical predictions. The main issue is how to control the relative speed of the pulse with respect to the temporal boundary. One possibility is to use a traveling-wave electro-optic modulator in which a microwave signal propagates at a different speed than that of the optical pulse. A pump-probe configuration in which cross-phase modulation would be used to produce a moving temporal boundary may also be possible but will require pump pulses of high energies.

ACKNOWLEDGMENT

This material is based upon work supported by the Department of Energy National Nuclear Security Administration under Award Number DE-NA0001944, the University of Rochester, and the New York State Energy Research and Development Authority. The support of DOE does not constitute an endorsement by DOE of the views expressed in this article.

REFERENCES

1. M. Born and E. Wolf, *Principles of Optics: Electromagnetic Theory of Propagation, Interference, and Diffraction of Light*, 7th expanded ed. (Cambridge University Press, Cambridge, England, 1999), pp. 752–758.
2. B. E. A. Saleh and M. C. Teich, *Fundamentals of Photonics*, 2nd ed. (Wiley-Interscience, Hoboken, NJ, 2007).
3. J. T. Mendonça and P. K. Shukla, *Phys. Scr.* **65**, 160 (2002).
4. Y. Xiao, D. N. Maywar, and G. P. Agrawal, *Opt. Lett.* **39**, 574 (2014).
5. M. F. Yanik and S. Fan, *Phys. Rev. Lett.* **93**, 173903 (2004).
6. M. Notomi and S. Mitsugi, *Phys. Rev. A* **73**, 051803(R) (2006).
7. S. F. Preble, Q. Xu, and M. Lipson, *Nat. Photonics* **1**, 293 (2007).
8. T. Tanabe *et al.*, *Phys. Rev. Lett.* **102**, 043907 (2009).
9. T. Kampfrath *et al.*, *Opt. Lett.* **34**, 3418 (2009).
10. T. Kampfrath *et al.*, *Phys. Rev. A* **81**, 043837 (2010).
11. A. Nishida *et al.*, *Appl. Phys. Lett.* **101**, 161118 (2012).
12. G. P. Agrawal, *Nonlinear Fiber Optics*, 5th ed. (Academic Press, Boston, 2013).
13. M. Castellanos Muñoz *et al.*, *Phys. Rev. Lett.* **112**, 053904 (2014).

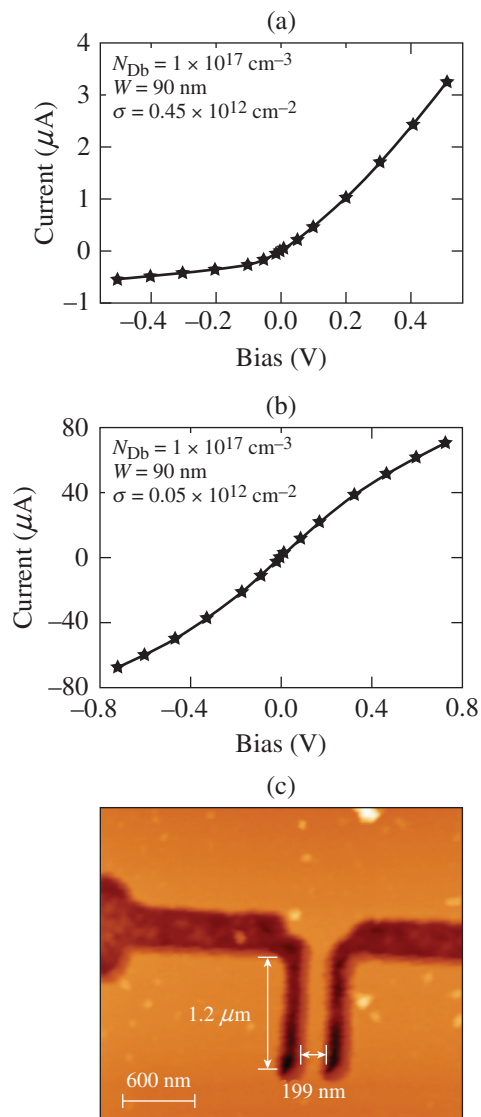
Ultrahigh Responsivity of Optically Active, Semiconducting Asymmetric Nanochannel Diodes

Introduction

Room-temperature nanodevices based on quantum confinement and/or ballistic nonlinearities are intrinsic nanostructures, not simply scaled-down conventional circuitry, and are gaining wide-spread research attention. Among the nanodevices, one of the most popular is the asymmetric nanochannel diode (ANCD), also referred to as a self-switching diode (SSD), first proposed by Song *et al.*¹ ANCD's, contrary to conventional diodes, do not rely on energy-barrier concepts to achieve rectification, but rather their nonlinear current–voltage (I – V) characteristics result from the carrier transport in an asymmetric nanochannel. The ANCD planar geometry allows for a flexible design and easy integration as a multi-element sensor or with either optical nanoconcentrators or THz coupling antennas. Based on Monte Carlo (MC) simulations, ANCD's are expected to be efficient THz generators,² which have been demonstrated to be viable THz detectors.³

Typically, carrier transport in ANCD's is confined to a two-dimensional electron gas (2DEG) layer in order to take advantage of the 2DEG ultrahigh mobility and, in this way, minimize the carrier transient time. Depending on the device's dimensions and/or fabrication process and the level of its control, there are two basic types of SSD's: “normally OFF” devices with a channel open/depleted at zero bias and “normally ON” devices, where the channel is always conducting. These two types exhibit quite different I – V curves, as shown in Figs. 143.42(a) and 143.42(b), where MC simulations⁴ of two ANCD's of the same geometry are presented but with different values for the surface charge σ .

Despite the popularity of SSD's, extensive fundamental and applied research is still needed to fully understand their direct current (dc) and radio-frequency (rf) carrier transport through the asymmetric nanochannel, as well as their performance in both the THz and optical radiation ranges. Our work presented here focuses on photoresponse properties of ANCD's, and we demonstrate that especially normally ON devices possess a very strong, intrinsic internal photoelectron gain mechanism, making them very attractive as possible room-temperature ultrafast optical detectors with single-photon sensitivity.



E24323JR

Figure 143.42 Monte Carlo (MC) results for I – V curves of an asymmetric nanochannel diode (ANCD) with a channel width $W = 90 \text{ nm}$ and two different values of the surface charge σ , leading to (a) a depleted channel and diode-like characteristics, (b) a conducting channel (effective width of 80 nm at zero dc bias) and nonlinear characteristics, and (c) an atomic force microscope image of an actual device.

Device Fabrication and Experimentation

Our tested devices consisted of $\sim 1.2\text{-}\mu\text{m}$ -long and $\sim 200\text{-}$ to 300-nm -wide channels [see Fig. 143.42(c)] and were fabricated on an InGaAs/InAlAs quantum-well heterostructure grown on an InP wafer. The fabrication started with the formation of mesa structures by wet chemical etching with an $\text{H}_3\text{PO}_4/\text{H}_2\text{O}_2/\text{H}_2\text{O}$ -based solution. Ohmic contacts were then formed by thermal evaporation of 50 nm of Au/Ge/Ni alloy, followed by a 200-nm Au layer. Finally a nanochannel was defined using electron-beam lithography and wet chemical etching.

The ANCD I–V curves were collected by measuring the transport current for the voltage-source biasing condition, both in the dark and under light illumination. For optical excitation, we used 800-nm -wavelength continuous-wave (cw) radiation generated by a commercial, non-mode-locked Ti:sapphire laser. The same laser system, but in the pulsed mode, was used for time-domain response characterization studies. For these measurements, our diodes were dc biased and illuminated with a train of 100-fs -wide pulses with an average power of about $400\text{ }\mu\text{W}$. The electrical output was registered using a bias-tee and a fast 6-GHz -bandwidth sampling oscilloscope.

Experimental Results and Analysis

Figure 143.43 presents a family of direct current I–V characteristics of a normally OFF device, measured in the dark (black dots) and with a single- μW level of light illumination (see figure caption) focused on the device. We note that the curve measured in the dark well resembles the one presented in Fig. 143.42(a). The unbiased ANCD is clearly in the OFF state and, when biased, a diode-like characteristic is well reproduced. A leakage current at negative bias is ascribed to the relatively large channel width of this ANCD sample, while the change of the slope near 3-V bias is caused, according to MC simulations, by velocity saturation associated with electron scattering from Γ into the L satellite valley.

The impact of the light illumination is very strong, as illustrated in the top left inset in Fig. 143.43, where we plot a family of photocurrent characteristics versus the bias voltage. The observed behavior very strongly points to optical gating of the nanochannel. In fact, the first quadrant (positive voltage and positive photocurrent) of the inset graph closely resembles the characteristics of a field-effect transistor (FET), except that here the various curves of the graph correspond to different optical intensities with a threshold optical power of about $0.9\text{ }\mu\text{W}$.

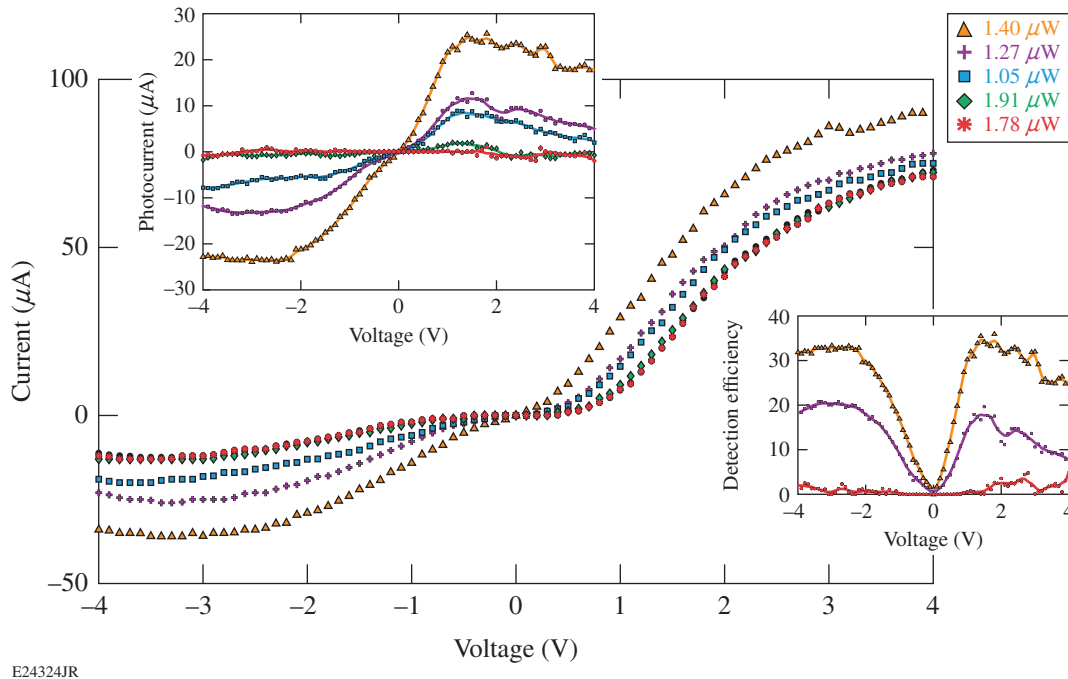


Figure 143.43

Direct-current I–V characteristics for a normally OFF device (channel width of $\sim 200\text{ nm}$) in darkness (black dots) and under 800-nm -wavelength cw laser illumination. The top left inset shows the photocurrent's dependence on the bias voltage, collected as the current difference between the I–V curve under a given illumination and the one measured in the dark. The bottom right inset presents the detection efficiency's (DE's) dependence on the bias voltage, calculated for a given curve as the ratio of the photocurrent to incident laser power and expressed in units of electron/photon. The legend for all presented traces is as follows: orange triangles $1.4\text{ }\mu\text{W}$; purple crosses $1.27\text{ }\mu\text{W}$; blue squares $1.05\text{ }\mu\text{W}$; green diamonds $0.91\text{ }\mu\text{W}$; and red stars $0.78\text{ }\mu\text{W}$.

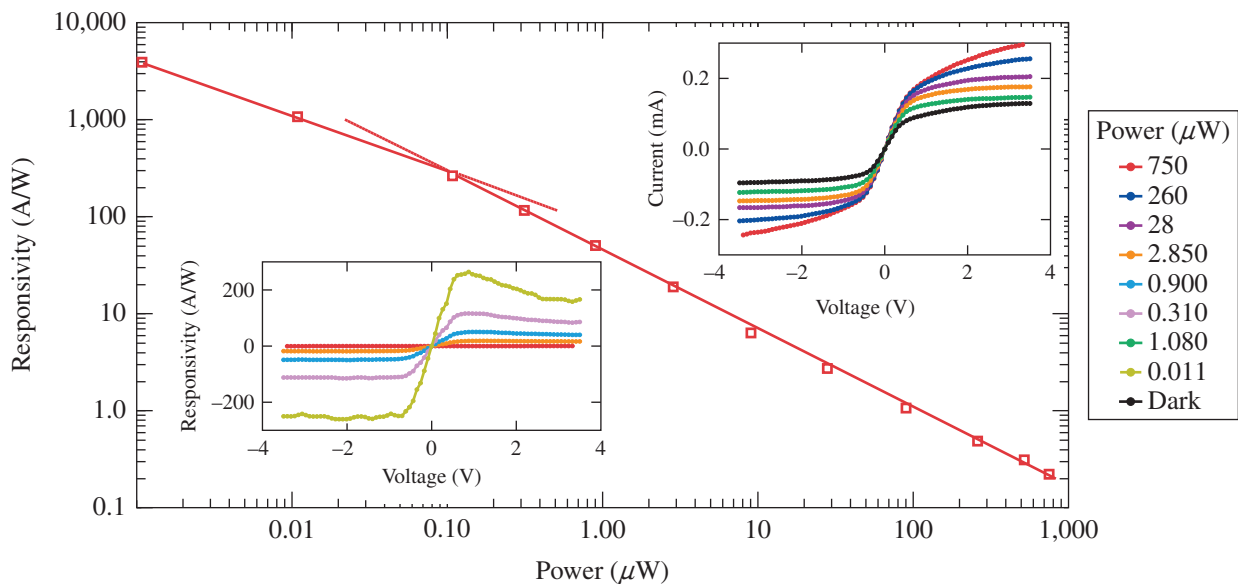
Optical gating in FET's has been recently studied;⁵ however, here we have a much simpler structure—an asymmetric nano-channel—and the effect is very strong, even as the incident light power changes in a very narrow range from 1 to 1.4 μW .

The optical gating is caused by photogenerated holes that move to locations below and/or beside the channel and are likely to partly compensate negative surface charges at the walls of the trenches. This effect reduces the channel depletion in an analogous way to a gate voltage in the FET, further opening the 2DEG channel and, consequently, leading to a large optical responsivity. The latter conclusion is in full agreement with the detection efficiency (DE) data presented in the bottom right inset in Fig. 143.43. The DE value increases with the incident light power and the ANCD structure exhibits an intrinsic gain; i.e., a $\text{DE} \gg 1$, resulting from the optical gating of the channel of the SSD.

A family of I–V characteristics, this time collected for a normally ON device, is shown in the top right inset in Fig. 143.44 and was measured under light illumination conditions similar to those in Fig. 143.43. We note that now the I–V curve measured in the dark (black dots) has an S-like shape and resembles the one presented in Fig. 143.42(b). The unbiased diode is clearly in the ON state, and when biased, the current is in the mA rather

than the μA range. The observed nonlinearity (transition toward saturation) comes, as indicated earlier, from the Γ – L electron scattering. Figure 143.44 (main panel) shows that the maximum optical responsivity (red squares), expressed in A/W (see also the left bottom panel), increases linearly (red solid line) with decreasing optical power over many orders of magnitude with only very slight tapering at the lowest light power levels, reaching a value of almost 10,000 A/W , comparable to the gain of avalanche-type, single-photon detectors.

The existence of optical gain in normally ON ANCD's is consistent with a model proposed for photoconductive gain in high-electron-mobility transistors (HEMT's).⁶ In this model, the band bending present in the 2DEG of the HEMT captures photoexcited electrons, which transit the channel of the device, while photoexcited holes are pushed away from the 2DEG and become trapped in the substrate or in surface states on the sidewalls of the channel. The value of the photoconductive gain is the ratio of the hole trapping time to the electron transit time. The gain is dependent on the optical power because the density of photogenerated charges affects the potential (as in the case of the normally OFF device) that separates the photo-generated holes from the 2DEG, thereby affecting the hole trapping time. The subpicosecond electron transit time of our ANCD's translates into a very large optical gain.



E24325JR

Figure 143.44 Maximum optical responsivity's (red squares; solid line is a linear fit) dependence on the incident optical power for a normally ON ANCD (channel width ~ 300 nm). The top right inset shows the I–V characteristics collected in the dark (black dots) and under 800-nm cw light illumination for power levels in the range of 750 to 0.11 μW . The bottom left inset presents examples of the responsivity versus the bias voltage.

We have also measured an impulse photoresponse of our normally ON sample using 100-fs-wide pulses from our mode-locked Ti:Al₂O₃ laser and a 50-GHz-bandwidth oscilloscope readout. The observed strong pulse (not shown) was ~120 ps wide and was followed by damped oscillations. Our measured signals were severely restricted by the limited bandwidth of the sample housing; i.e., inductance of wire bonds and pad capacitance, designed for strictly dc characterization.

Conclusions

We have shown that ANCD's, originally intended for THz applications, also have very interesting photoresponse properties. In normally OFF devices, where the nanochannel width is defined by the depletion layers and electric-field-controlled, optical illumination plays a role of optical gating, analogous to the gate in FET structures. On the other hand, the physics of the photoresponse gain mechanism in normally ON ANCD's arises from a dramatic difference between a subpicosecond transient time of electrons traveling in the 2DEG nanochannel layer and the microsecond lifetime of holes, optically excited and subsequently pushed toward the substrate. When cooled (to

minimize the dark current), our ANCD's should be practical photon counters. The ANCD's implemented in the InAs or InSb material systems should be especially attractive since they will cover the infrared radiation region, including the most-important telecommunication and thermal-imaging wavelengths.

ACKNOWLEDGMENT

The work in Rochester was supported in part by a University of Rochester Research Grant and by ARO Grant #W911NF-15-1-0356.

REFERENCES

1. A. M. Song *et al.*, Appl. Phys. Lett. **83**, 1881 (2003).
2. K. Y. Xu, G. Wang, and A. M. Song, Appl. Phys. Lett. **93**, 233506 (2008).
3. C. Balocco *et al.*, Appl. Phys. Lett. **98**, 223501 (2011).
4. J. Mateos *et al.*, Appl. Phys. Lett. **86**, 212103 (2005).
5. S. Tripathi and S. Jit, J. Appl. Phys. **109**, 053102 (2011).
6. M. A. Romero, M. A. G. Martinez, and P. R. Herczfeld, IEEE Trans. Microw. Theory Tech. **44**, 2279 (1996).

Publications and Conference Presentations

Publications

- R. Betti, A. R. Christopherson, B. K. Spears, R. Nora, A. Bose, J. Howard, K. M. Woo, M. J. Edwards, and J. Sanz, "Alpha Heating and Burning Plasmas in Inertial Confinement Fusion," *Phys. Rev. Lett.* **114**, 255003 (2015).
- A. Bose, K. M. Woo, R. Nora, and R. Betti, "Hydrodynamic Scaling of the Deceleration-Phase Rayleigh–Taylor Instability," *Phys. Plasmas* **22**, 072702 (2015).
- L. Gao, P. M. Nilson, I. V. Igumenshchev, M. G. Haines, D. H. Froula, R. Betti, and D. D. Meyerhofer, "Precision Mapping of Laser-Driven Magnetic Fields and Their Evolution in High-Energy-Density Plasmas," *Phys. Rev. Lett.* **114**, 215003 (2015).
- H. Habara, S. Ivancic, K. Anderson, D. Haberberger, T. Iwawaki, C. Stoeckl, K. A. Tanaka, Y. Uematsu, and W. Theobald, "Efficient Propagation of Ultra-Intense Laser Beam in Dense Plasma," *Plasma Phys. Control. Fusion* **57**, 064005 (2015).
- M. Hohenberger, P. B. Radha, J. F. Myatt, S. LePape, J. A. Marozas, F. J. Marshall, D. T. Michel, S. P. Regan, W. Seka, A. Shvydky, T. C. Sangster, J. W. Bates, R. Betti, T. R. Boehly, M. J. Bonino, D. T. Casey, T. J. B. Collins, R. S. Craxton, J. A. Delettrez, D. H. Edgell, R. Epstein, G. Fiksel, P. Fitzsimmons, J. A. Frenje, D. H. Froula, V. N. Goncharov, D. R. Harding, D. H. Kalantar, M. Karasik, T. J. Kessler, J. D. Kilkenny, J. P. Knauer, C. Kurz, M. Lafon, K. N. LaFortune, B. J. MacGowan, A. J. Mackinnon, A. G. MacPhee, R. L. McCrory, P. W. McKenty, J. F. Meeker, D. D. Meyerhofer, S. R. Nagel, A. Nikroo, S. Obenschain, R. D. Petrasso, J. E. Ralph, H. G. Rinderknecht, M. J. Rosenberg, A. J. Schmitt, R. J. Wallace, J. Weaver, C. Widmayer, S. Skupsky, A. A. Solodov, C. Stoeckl, B. Yaakobi, and J. D. Zuegel, "Polar-Direct-Drive Experiments on the National Ignition Facility," *Phys. Plasmas* **22**, 056308 (2015) (invited).
- S. X. Hu, V. N. Goncharov, T. R. Boehly, R. L. McCrory, S. Skupsky, L. A. Collins, J. D. Kress, and B. Militzer, "Impact of First-Principles Properties of Deuterium–Tritium on Inertial Confinement Fusion Target Designs," *Phys. Plasmas* **22**, 056304 (2015) (invited).
- S. Ivancic, D. Haberberger, H. Habara, T. Iwawaki, K. S. Anderson, R. S. Craxton, D. H. Froula, D. D. Meyerhofer, C. Stoeckl, K. A. Tanaka, and W. Theobald, "Channeling of Multikilojoule High-Intensity Laser Beams in an Inhomogeneous Plasma," *Phys. Rev. E* **91**, 051101(R) (2015).
- A. Klimov, R. Puźniak, B. Aichner, W. Lang, E. Joon, R. Stern, W. Słysz, M. Guzewicz, M. Juchniewicz, M. A. Borysiewicz, R. Kruszka, M. Węgrzecki, A. Łaszcz, A. Czerwinski, and R. Sobolewski, "Superconducting and Ferromagnetic Properties of NbN/NiCu and NbTiN/NiCu Bilayer Nanostructures for Photon Detection," in *Photon Counting Applications 2015*, edited by I. Prochazka, R. Sobolewski, and R. B. James (SPIE, Bellingham, WA, 2015), Vol. 9504, Paper 950405.
- T. Z. Kosc, J. H. Kelly, E. M. Hill, C. Dorrer, L. J. Waxer, and W. R. Donaldson, "The Multiple-Pulse Driver Line on the OMEGA Laser," in *High Power Lasers for Fusion Research III*, edited by A. A. S. Awwal and M. A. Lane (SPIE, Bellingham, WA, 2015), Vol. 9345, Paper 93450H.
- D. T. Michel, A. K. Davis, W. J. Armstrong, R. E. Bahr, R. Epstein, V. N. Goncharov, M. Hohenberger, I. V. Igumenshchev, R. K. Jungquist, D. D. Meyerhofer, P. B. Radha, T. C. Sangster, C. Sorce, and D. H. Froula, "Measurements of the Ablation-Front Trajectory and Low-Mode Nonuniformity in Direct-Drive Implosions Using X-Ray Self-Emission Shadowgraphy," *High Power Laser Science and Engineering* **3**, e19 (2015).
- U. Nasti, L. Parlato, M. Ejrnaes, R. Cristiano, T. Taino, H. Myoren, R. Sobolewski, and G. Pepe, "Thermal Fluctuations in Superconductor/Ferromagnet Nanostripes," *Phys. Rev. B* **92**, 014501 (2015).
- P. M. Nilson, L. Gao, I. V. Igumenshchev, G. Fiksel, R. Yan, J. R. Davies, D. Martinez, V. A. Smalyuk, M. G.

Haines, E. G. Blackman, D. H. Froula, R. Betti, and D. D. Meyerhofer, “Magnetic-Field Generation by the Ablative Nonlinear Rayleigh–Taylor Instability,” *J. Plasma Phys.* **81**, 365810201 (2015).

H.-S. Park, C. M. Huntington, F. Fiuza, R. P. Drake, D. H. Froula, G. Gregori, M. Koenig, N. L. Kugland, C. C. Kuranz, D. Q. Lamb, M. C. Levy, C. K. Li, J. Meinecke, T. Morita, R. D. Petrasso, B. B. Pollock, B. A. Remington, H. G. Rinderknecht, M. Rosenberg, J. S. Ross, D. D. Ryutov, Y. Sakawa, A. Spitkovsky, H. Takabe, D. P. Turnbull, P. Tzeferacos, S. V. Weber, and A. B. Zylstra, “Collisionless Shock Experiments with Lasers and Observation of Weibel Instabilities,” *Phys. Plasmas* **22**, 056311 (2015).

L. Parlato, U. Nasti, M. Ejrnaes, R. Cristiano, H. Myoren, R. Sobolewski, and G. Pepe, “Dark Counts in Superconducting Single-Photon NbN/NiCu Detectors,” in *Photon Counting Applications 2015*, edited by I. Prochazka, R. Sobolewski, and R. B. James (SPIE, Bellingham, WA, 2015), Vol. 9504, Paper 950404.

G. P. Pepe, L. Parlato, M. Ejrnaes, R. Cristiano, R. Arpaia, F. Tafuri, D. Golubev, T. Bauch, F. Lombardi, and R. Sobolewski, “Y-Ba-Cu-O Nanostripes for Optical Photon Detection,” in

Photon Counting Applications 2015, edited by I. Prochazka, R. Sobolewski, and R. B. James (SPIE, Bellingham, WA, 2015), Vol. 9504, Paper 950406 (invited).

B. W. Plansinis, W. R. Donaldson, and G. P. Agrawal, “Spectral Changes Induced by a Phase Modulator Acting as a Time Lens,” *J. Opt. Soc. Am. B* **32**, 1550 (2015).

W. Theobald, R. Nora, W. Seka, M. Lafon, K. S. Anderson, M. Hohenberger, F. J. Marshall, D. T. Michel, A. A. Solodov, C. Stoeckl, D. H. Edgell, B. Yaakobi, A. Casner, C. Reverdin, X. Ribeyre, A. Shvydky, A. Vallet, J. Peebles, F. N. Beg, M. S. Wei, and R. Betti, “Spherical Strong-Shock Generation for Shock-Ignition Inertial Fusion,” *Phys. Plasmas* **22**, 056310 (2015) (invited).

A. N. Tsympkin, S. E. Putilin, A. V. Okishev, and S. A. Kozlov, “Ultrafast Information Transfer Through Optical Fiber by Means of Quasidiscrete Spectral Supercontinua,” *Opt. Eng.* **54**, 056111 (2015).

H. Wen, R. Yan, A. V. Maximov, and C. Ren, “Linear Regime of Two-Plasmon Decay and Stimulated Raman Scattering Instability Near the Quarter-Critical Density in Plasmas,” *Phys. Plasmas* **22**, 052704 (2015).

Forthcoming Publications

J. Bromage, C. Dorrer, and J. D. Zuegel, “Temporal-Contrast Measurements of a White-Light–Seeded Noncollinear Optical Parametric Amplifier,” to be published in the *Journal of Optics*.

R. S. Craxton, K. S. Anderson, T. R. Boehly, V. N. Goncharov, D. R. Harding, J. P. Knauer, R. L. McCrory, P. W. McKenty, D. D. Meyerhofer, J. F. Myatt, A. J. Schmitt, J. D. Sethian, R. W. Short, S. Skupsky, W. Theobald, W. L. Kruer, K. Tanaka, R. Betti, T. J. B. Collins, J. A. Delettrez, S. X. Hu, J. A. Marozas, A. V. Maximov, D. T. Michel, P. B. Radha, S. P. Regan, T. C. Sangster, W. Seka, A. A. Solodov, J. M. Soures, C. Stoeckl, and J. D. Zuegel, “Direct-Drive Inertial Confinement Fusion: A Review,” to be published in *Physics of Plasmas*.

C. Dorrer, A. Consentino, D. Irwin, J. Qiao, and J. D. Zuegel, “OPCPA Front End and Contrast Optimization for the OMEGA EP Kilojoule, Picosecond Laser,” to be published in the *Journal of Optics*.

R. Epstein, S. P. Regan, B. A. Hammel, L. J. Suter, H. A. Scott, M. A. Barrios, D. K. Bradley, D. A. Callahan, C. Cerjan, G. W. Collins, S. N. Dixit, T. Döppner, M. J. Edwards, D. R. Farley, K. B. Fournier, S. Glenn, S. H. Glenzer, I. E. Golovkin, A. Hamza, D. G. Hicks, N. Izumi, O. S. Jones, M. H. Key, J. D. Kilkenny, J. L. Kline, G. A. Kyrala, O. L. Landen, T. Ma, J. J. MacFarlane, A. J. Mackinnon, R. C. Mancini, R. L. McCrory, D. D. Meyerhofer, N. B. Meezan, A. Nikroo, H.-S. Park, P. K. Patel, J. E. Ralph, B. A. Remington, T. C. Sangster, V. A. Smalyuk, P. T. Springer, R. P. J. Town, and J. L. Tucker, “Applications and Results of X-Ray Spectroscopy in Implosion Experiments on the National Ignition Facility,” to be published in *Proceedings of Atomic Processes in Plasmas* (invited).

P. M. Nilson, A. A. Solodov, J. R. Davies, W. Theobald, C. Mileham, C. Stoeckl, I. A. Begishev, J. D. Zuegel, D. H. Froula, R. Betti, and D. D. Meyerhofer, “Time-Resolved K_{α} Spectroscopy Measurements of Hot-Electron Equilibration Dynamics in Thin-Foil Solid Targets: Collisional and Col-

lective Effects,” to be published in the Journal of Physics B: Atomic, Molecular and Optical Physics.

P. B. Radha, V. N. Goncharov, M. Hohenberger, T. C. Sangster, R. Betti, R. S. Craxton, D. H. Edgell, R. Epstein, D. H. Froula, J. A. Marozas, F. J. Marshall, R. L. McCrory, P. W. McKenty,

D. D. Meyerhofer, D. T. Michel, S. X. Hu, W. Seka, A. Shvydky, S. Skupsky, J. A. Frenje, M. Gatu Johnson, R. D. Petrasso, T. Ma, S. Le Pape, and A. J. Mackinnon, “Direct-Drive–Implosion Physics: Results from OMEGA and the National Ignition Facility,” to be published in the Journal of Physics: Conference Series.

Conference Presentations

The following presentations were made at ILOW 2015, Bordeaux, France, 7–9 April 2015:

D. Canning, B. E. Kruschwitz, M. Barczys, J. Kwiatkowski, K. Gibney, and D. Weiner, “UV Stray-Light Management on OMEGA EP.”

E. M. Hill, J. H. Kelly, T. Z. Kosc, C. Dorrer, C. Stoeckl, and W. R. Donaldson, “Operational Challenges and Advances in the Generation and Co-Timing of High-Precision, Low-Jitter Pulse Shapes.”

T. Z. Kosc, J. H. Kelly, E. M. Hill, and L. J. Waxer, “Design and Operation of the Multiple-Pulse Driver Line on the OMEGA Laser.”

S. F. B. Morse, R. L. McCrory, S. J. Loucks, T. C. Sangster, S. Skupsky, D. D. Meyerhofer, J. D. Zuegel, J. H. Kelly, B. E. Kruschwitz, T. Z. Kosc, M. Barczys, L. J. Waxer, M. J. Guardalben, W. T. Shmayda, R. T. Janezic, J. C. Puth, S. Stagnitto, D. Canning, E. M. Hill, C. Sorce, C. Stoeckl, M. J. Shoup III, W. R. Donaldson, C. Dorrer, M. D. Wittman, R. Earley, J. Bromage, S. P. Regan, B. S. Rice, J. Ulrich, D. R. Harding, and D. H. Froula, “Omega: Capability Improvements and National Ignition Facility Enhancements for Polar Direct Drive.”

C. Sorce, R. E. Bahr, R. Boni, J. Katz, D. Mastrosimone, M. McCluskey, C. Mileham, A. Sorce, and N. Whiting, “The Experimental Support Group’s Role at the Omega Laser Facility.”

The following presentations were made at the Undergraduate Research Exposition, Rochester, NY, 10 April 2015:

P. Angland, D. Haberberger, S. Ivancic, and D. H. Froula, “An Iterative Program to Find Plasma Density Profiles from Angular-Filter-Refractometry Images.”

J. Hassett, R. Boni, and D. H. Froula, “Diffracted Efficiencies for Optical Wavelength Gratings with Arbitrary Groove Shapes are Predicted and Compared to Measurements.”

J. D. Zuegel, S.-W. Bahk, J. Bromage, M. J. Guardalben, B. E. Kruschwitz, J. B. Oliver, C. Robillard, M. J. Shoup III, C. Stoeckl, and L. J. Waxer, “Technology Development and Prospects for Multi-10-PW OPCPA Pumped by OMEGA EP,” Research Using Extreme Light, Prague, Czech Republic, 13–16 April 2015.

The following presentations were made at the 2015 University Technology Showcase, Rochester, NY, 16 April 2015:

W. R. Donaldson, “High-Dynamic-Range, Single-Shot, 10-GHz Signal Processing.”

K. Tinkham, T. Jacobs, M. Mayton, Z. Hobbs, and K. L. Marshall, “Cerium Oxide Polishing Slurry Reclamation Project: Characterization Techniques and Results.”

The following presentations were made at the Seventh Omega Laser Facility Users Group Workshop, Rochester, NY, 22–24 April 2015:

P. Angland, D. Haberberger, S. Ivancic, and D. H. Froula, “An Iterative Program to Find Plasma Density Profiles from Angular-Filter-Refractometry Images.”

E. M. Garcia and R. S. Craxton, “Optimization of Uniformity for Current Polar-Direct-Drive Implosion Experiments at the National Ignition Facility.”

J. Hassett, R. Boni, and D. H. Froula, “Diffracted Efficiencies for Optical Wavelength Gratings with Arbitrary Groove Shapes are Predicted and Compared to Measurements.”

J. Katz, C. Stoeckl, J. Magoon, R. Taylor, D. Guy, M. Couch, F. Ehrne, D. J. Lonobile, D. Weiner, E. C. Cost, C. Rees, M. H. Romanofsky, J. Szczepanski, C. Abbott, T. Lewis, and M. Maslyn, “Commissioning the P11 Neutron Temporal Diagnostic for High-Neutron-Yield Implosions.”

R. W. Kidder, A. Zeller, T. Meyer, P. Stoeckl, R. Pasols, and R. Hoderried, “External User Access Through the LLE PI Portal.”

J. Kwiatkowski, M. Barczys, M. Bedzyk, A. Kalb, B. E. Kruschwitz, C. McMahan, T. Nguyen, A. L. Rigatti, and M. Sacchitella, “OMEGA EP Short-Pulse-Transmission Study Status Report.”

D. Mastrosimone, A. Agliata, T. Buczek, D. J. Lonobile, M. J. Shoup III, and C. Sorce, “Enhanced Gas-Filled Capabilities for Ten-Inch–Manipulator–Based Target Positioners.”

S. F. B. Morse, “Omega Facility OLUG 2015 Update: Progress on Recommendations and Items of General Interest.”

S. P. Regan, T. C. Sangster, V. N. Goncharov, R. Epstein, P. B. Radha, R. Betti, T. R. Boehly, R. Earley, C. J. Forrest, D. H. Froula, V. Yu. Glebov, E. M. Hill, S. X. Hu, I. V. Igumenshchev, R. T. Janezic, J. H. Kelly, T. J. Kessler, T. Z. Kosc, J. Kwiatkowski, J. A. Marozas, F. J. Marshall, R. L. McCrory, P. W. McKenty, D. D. Meyerhofer, D. T. Michel, J. F. Myatt, J. C. Puth, N. P. Redden, J. Reid, W. Seka, W. T. Shmayda, A. Shvydky, C. Stoeckl, M. D. Wittman, J. A. Frenje, M. Gatu Johnson, and R. D. Petrasso, “OMEGA Layered DT Cryogenic Implosions” (invited).

R. Zhang, C. Kingsley, and R. T. Janezic, “Statistical Investigation of Cryogenic Target Defects.”

N. D. Viza and D. R. Harding, “Using Lab-on-Chip Technology to Mass Produce Inertial Fusion Energy Targets,” 5th Energy for the 21st Century Symposium, Rochester, NY, 1 May 2015.

The following presentations were made at CLEO 2015, San Jose, CA, 10–15 May 2015:

S.-W. Bahk, C. Dorrer, R. G. Roides, and J. Bromage, “A Spectrally Resolved Lateral-Shearing Interferometer to Measure Relative Group Delay Using a Periodic Entrance Slit in a Spectrometer.”

C. Dorrer, W. A. Bittle, R. Cuffney, M. Spilatro, E. M. Hill, J. H. Kelly, T. Z. Kosc, and J. D. Zuegel, “A Time-Multiplexed Pulse-Shaping System for Generating Multiple High-Bandwidth, Low-Jitter Optical Waveforms.”

C. Dorrer, L. Waxer, A. Kalb, E. M. Hill, and J. Bromage, “Single-Shot Characterization of Optical Pulses Below the Resolution Limit by Phase-Diversified Photodetection.”

P. Fiala, C. Dorrer, and K. L. Marshall, “Twisted-Nematic Liquid Crystal Polarization Rotators for Broadband Laser Applications.”

L. E. McIntire, M. Divoky, W. H. Knox, S.-W. Bahk, and J. D. Zuegel, “High-Contrast, Closed-Loop Control of Laser-Beam Profiles.”

M. Sharpe, W. T. Shmayda, and W. U. Schröder, “Modeling Tritium Migration into the Adsorbed Water Layers on Metal Surfaces,” Symposium on Fusion Engineering, Austin, TX, 31 May–4 June 2015.

S.-W. Bahk, R. G. Roides, J. Bromage, and J. D. Zuegel, “Laser-Beam Shaping and Imaging Using Adaptive Quasi-Phase Conjugation,” Computational Optical Sensing and Imaging, Arlington, VA, 7–11 June 2015.

The following presentations were made at the 19th Biennial APS Conference on Shock Compression of Condensed Matter, Tampa, FL, 14–19 June 2015:

T. R. Boehly, M. C. Gregor, C. A. McCoy, D. N. Polsin, and D. E. Fratanduono, “High-Energy-Density Studies at the Omega Laser Facility.”

D. N. Polsin, C. A. McCoy, M. C. Gregor, T. R. Boehly, T. C. Sangster, D. E. Fratanduono, and P. M. Celliers, “Probing the Release of Shocked Material.”

The following presentations were made at the 45th Anomalous Absorption Conference, Ventura, CA, 14–19 June 2015:

R. Betti, K. S. Anderson, A. Bose, M. Lafon, R. Nora, and W. Theobald, “Electron Shock Ignition of Thermonuclear Fuel.”

A. Bose, R. Betti, K. M. Woo, A. R. Christopherson, and D. Shvarts, “Effects of Long- and Intermediate-Wavelength Asymmetries on Hot-Spot Energetics.”

A. K. Davis, D. Cao, D. T. Michel, R. Epstein, V. N. Goncharov, S. X. Hu, I. V. Igumenshchev, M. Lafon, J. Marozas, D. D. Meyerhofer, P. B. Radha, T. C. Sangster, and D. H. Froula, “Quantifying the Growth of Cross-Beam Energy Transfer in Polar-Direct-Drive Implosions.”

D. H. Edgell, R. K. Follett, V. N. Goncharov, I. V. Igumenshchev, J. Katz, J. F. Myatt, W. Seka, and D. H. Froula, “Diagnosing Cross-Beam Energy Transfer Using Beamlets of Unabsorbed Light from Direct-Drive Implosions.”

R. K. Follett, J. G. Shaw, D. H. Edgell, R. J. Henchen, S. X. Hu, J. Katz, D. T. Michel, J. F. Myatt, A. A. Solodov, C. Stoeckl, B. Yaakobi, and D. H. Froula, “Zakharov Modeling of Thomson-Scattering Measurements of Multibeam Two-Plasmon Decay.”

D. H. Froula, J. A. Delettrez, G. Fiksel, V. N. Goncharov, S. X. Hu, H. Huang, I. V. Igumenshchev, T. J. Kessler, D. D. Meyerhofer, D. T. Michel, S. P. Regan, T. C. Sangster, A. Shvydky, and J. D. Zuegel, “A Pathway to Ignition-Hydrodynamic-Equivalent Implosions in OMEGA Direct Drive Through the Reduction of Cross-Beam Energy Transfer.”

M. C. Gregor, T. R. Boehly, C. A. McCoy, D. N. Polsin, D. D. Meyerhofer, D. E. Fratanduono, P. M. Celliers, and G. W. Collins, “The Release Behavior of Diamond Shocked to 15 Mbar.”

R. J. Henchen, S. X. Hu, R. K. Follett, J. Katz, D. H. Froula, and W. Rozmus, “Heat-Flux Measurements from Thomson-Scattering Spectra.”

S. X. Hu, L. A. Collins, V. N. Goncharov, and S. Skupsky, “Extended Equation of State of Polystyrene (CH) Based on First-Principles Calculations.”

S. Ivancic, D. Haberberger, C. Stoeckl, K. S. Anderson, C. Ren, W. Theobald, J. Fienup, D. H. Froula, D. D. Meyerhofer, T. Iwawaki, H. Habara, and K. A. Tanaka, “Optical Probing of Laser-Produced Plasma Experiments on the OMEGA EP Laser System” (invited).

J. Li, C. Ren, and R. Yan, “Two-Plasmon–Decay Instabilities in a Plasma with Ion-Density Fluctuations.”

A. V. Maximov, J. F. Myatt, R. W. Short, I. V. Igumenshchev, and W. Seka, “The Effects of Beam Incoherence and Colors on Cross-Beam Energy Transfer.”

D. T. Michel, T. C. Sangster, V. N. Goncharov, A. K. Davis, R. Epstein, V. Yu. Glebov, S. X. Hu, I. V. Igumenshchev, D. D. Meyerhofer, S. P. Regan, W. Seka, A. Shvydky, C. Stoeckl, and D. H. Froula, “Measurements of the Conduction-Zone Length and Mass Ablation Rate in Cryogenic Direct-Drive Implosions on OMEGA.”

J. F. Myatt, J. G. Shaw, V. N. Goncharov, J. Zhang, A. V. Maximov, R. W. Short, W. Seka, D. H. Edgell, D. H. Froula, D. F. DuBois, D. A. Russell, and H. Vu, “A Numerical Model for Hot-Electron Generation in Direct-Drive Implosions.”

M. J. Rosenberg, A. A. Solodov, W. Seka, R. Epstein, J. F. Myatt, S. P. Regan, M. Hohenberger, T. J. B. Collins, J. E. Ralph, D. P. Turnbull, J. D. Moody, and M. A. Barrios, “Planar Two-Plasmon–Decay Experiments at Polar-Direct-Drive Ignition-Relevant Scale Lengths at the National Ignition Facility.”

W. Seka, S. P. Regan, P. B. Radha, J. A. Marozas, M. J. Rosenberg, M. Hohenberger, V. N. Goncharov, J. F. Myatt, D. H. Edgell, D. T. Michel, D. H. Froula, J. E. Ralph, J. D. Moody, and D. P. Turnbull, “The Current *LILAC* Model for Cross-Beam Energy Transfer (CBET) has been Extended to *DRACO* and Non-Symmetrical Illumination.”

R. W. Short, A. V. Maximov, J. F. Myatt, W. Seka, and J. Zhang, “Absolute Two-Plasmon Decay and Stimulated Raman Scattering in Direct-Drive Irradiation Geometries.”

A. A. Solodov, B. Yaakobi, J. F. Myatt, C. Stoeckl, and D. H. Froula, "Hot-Electron Temperature Measurements with Laser Irradiation at 10^{14} to 10^{15} W/cm²."

R. Yan, R. Betti, J. Sanz, B. Liu, and A. Frank, "Three-Dimensional Single-Mode Nonlinear Ablative Rayleigh–Taylor Instability."

The following presentations were made at the 21st Target Fabrication Meeting, Las Vegas, NV, 21–25 June 2015:

M. J. Bonino, D. R. Harding, D. W. Turner, H. Goodrich, A. Caveglia, M. Dorward, and M. Anthamatten, "The Mechanical Properties of the Adhesives Used for Cryogenic Targets."

B. Chock, T. B. Jones, and D. R. Harding, "Effect of a Surfactant on the Electric-Field Assembly of Oil/Water Emulsions for Making Foam Targets."

D. R. Harding, R. Q. Gram, K. Arian-Raines, J. Du, T. P. Bernat, and N. Petta, "Calorimetry Measurement of Supercooling in Liquid D₂, Suppression of Supercooling, and the Controlled Growth of a D₂ Crystal."

D. R. Harding, M. D. Wittman, N. P. Redden, C. Fella, and D. C. Whitaker, "How Interfacial Surface Energy Affects the Growth of the DT Ice Layer and the Fuel Content in Fill-Tube Targets."

N. P. Redden, D. R. Harding, and M. D. Wittman, "Controlling the D₂ and H₂/D₂ Fuel Content in Cryogenic Direct-Drive National Ignition Facility Targets."

T. C. Sangster, V. N. Goncharov, P. B. Radha, M. Hohenberger, S. P. Regan, T. J. B. Collins, R. S. Craxton, J. A. Delettrez, D. H. Edgell, R. Epstein, P. Fitzimmons, C. J. Forrest, J. A. Frenje, D. H. Froula, M. Gatu Johnson, V. Yu. Glebov, D. R. Harding, S. X. Hu, I. V. Igumenshchev, R. T. Janezic, M. Karasik, J. H. Kelly, T. J. Kessler, J. P. Knauer, T. Z. Kosc,

C. Kurz, S. LePape, A. J. Mackinnon, J. A. Marozas, F. J. Marshall, R. L. McCrory, P. W. McKenty, D. T. Michel, J. F. Myatt, A. Nikroo, S. P. Obenshain, R. D. Petrasso, H. G. Rinderknecht, M. J. Rosenberg, A. J. Schmitt, W. Seka, W. T. Shmayda, A. Shvydky, C. Stoeckl, S. Skupsky, J. Weaver, and A. Zylstra, "Progress with Direct-Drive Inertial Confinement Fusion."

D. W. Turner, M. J. Bonino, S. G. Noyes, and D. R. Harding, "Assembly of Direct-Drive Fill-Tube Targets."

N. D. Viza, M. J. Moynihan, and D. R. Harding, "The Effect of a Surfactant on the Operation of T-Junctions for Mass-Producing Foam Targets."

J. B. Oliver, T. J. Kessler, C. Smith, B. Taylor, V. Gruschow, J. Hettrick, B. Charles, J. Spaulding, T. Noll, A. L. Rigatti, S. Papernov, K. A. Sharma, G. Mitchell, and J. Foster, "Development of a Glancing-Angle–Deposited Distributed Polarization Rotator," Novel Optical Materials and Applications, Boston, MA, 26 June–1 July 2015.

The following presentations were made at the 19th International Conference on Electron Dynamics, Optoelectronics, and Nanostructures, Salamanca, Spain, 29 June–2 July 2015:

Y. Akbas, A. Stern, L. Q. Zhang, Y. Alimi, A. M. Song, I. Iñiguez-de-la-Torre, J. Mateos, T. González, G. W. Wicks, and R. Sobolewski, "Ultrahigh Responsivity of Optically Active Semiconducting Asymmetric Nanochannel Diodes."

J. Serafini, Y. Akbas, L. Crandall, R. Bellman, C. K. Williams, and R. Sobolewski, "Time-Resolved, Nonequilibrium Carrier Dynamics in Si-on-Glass Thin-Film Absorbers for Photovoltaic Cells."

